Study of the variability of active galactic nuclei at very high energy with H.E.S.S.

Gabriel Emery

LPNHE
PARIS

PhD THESIS
OF SORBONNE UNIVERSITÉ

presented by

Gabriel EMERY

Submitted in fulfilment of the requirements for the degree of

DOCTEUR DE SORBONNE UNIVERSITÉ

Speciality :

Physics of the Universe (STEP'UP - ED 560)

Study of the variability of active galactic nuclei at very high energy with H.E.S.S.

Defended on September 16th 2020 in front of the committee:

Mr	Jean-Philippe	Lenain	Supervisor
Mrs	Marianne	Lemoine-Goumard	Referee
Mr	Frédéric	Piron	Referee
Mr	Christophe	Balland	Examiner
Mrs	Piera	Ghia	Examiner
Mr	Mosè	Mariotti	Examiner

cnrs IN2P3 Les deux infinis

SORBONNE UNIVERSITÉ CRÉATEURS DE FUTURS DEPUIS 1257

Université de Paris

Acknowledgements

Compilation of more than three years of work, and the consecration of even more years of learning, this manuscript wouldn't have existed or at least been as enjoyable to produce without the presence of a lot of people. I will try here to highlight specific individuals and groups.

The one group that accompanied me the longest is my family, always there and supportive in my choice of career and passion. In order for all of them to be able to read it, a bit of french.

Une première mention concerne bien sûr ma famille, qui a toujours supporté mes choix de carrière et ma passion pour la science. Des dizaines de noms me viennent à l'esprit, et bien que j'ai une pensée pour chaqu'un d'entre eux je ne tenterais pas ici de tous les citer. Le temps passé avec les membres de ma famille forme un ensemble de très bons moments qui ont été une source de joie depuis toujours. Mention spéciale pour mon père et ma mère, qui ont été une aide précieuse et sont venu assister à ma soutenance pour écouter un exposé de codes étranges et incompréhensibles. Un de mes cousin était aussi présent à ma soutenance, et tant que premier docteur de la famille était sûrement le plus à même de comprendre ce qui se disait malgré un domaine d'expertise différent.

The LPNHE where my work was performed gathers an awesome community with which I was able to interact on multiple occasions. I got very close to some of the people there, while others are remembered as short but enjoyable interactions. My longest standing office mates : Julianna and Christelle, were very fun to hang with in and outside the office and allowed for very interesting and regular conversations. They are part of the many friends that I made in the lab over the years, mostly but not only from the other doctorants, and that I hope I will be able to keep good contacts with. Sophie, my thesis god mother in the lab, was always available to talk and help me if needed. While it ended up being mostly convenience queries about teaching, her presence was very appreciated. The H.E.S.S. group was very enjoyable to be a part of. Be it for work, lunch or other activities. Speaking about H.E.S.S., the collaboration was also very inclusive with regular meetings allowing to meet everyone for work during the days, and socialisation in the evening. Once again this was a source of fun and new friends.

For taking the time to read this document, and to make it better through comments and questions in the process, I want to thank every members of my jury. My rapporteurs Marianne and Frédéric, gave me a lot to think about with their comments. The president of the jury Christophe also expressed his interest for my work and is also someone with whom I interacted regularly in the lab. And finally Piera and Mosè, who also had insightful and interesting questions during my defence.

Finally, I kept the person which was the most important for these three years of work. Jean-Philippe have been an amazing supervisor with whom it was always easy to interact in all settings. Always there to help me, he also pushed me when needed to improve my work. I often think that I can't even imagine a better supervisor and fell blessed for having been able to work with him on this project.

September 2020

Contents

Liste des figures

Liste des tables

Introduction

Since the dawn of humanity, observations of the optical light reaching Earth were used to develop an understanding of the Universe we live in. In the 19th century, the revolution of electromagnetism extended the range of potential observations to invisible light. It was later observed in the early 20th century with, e.g., the observation of astrophysical radio waves by Karl Jansky. During this period, first observations of highly energetic charged radiations coming from space were also performed, with the most famous being balloon observations by Victor Hess. The parallel development of particle physics and observation techniques then allowed to identify these radiations and to better characterise their energy distribution.

With the rapid technological and theoretical development since then, it is now known that Earth constantly receives particles from everywhere in the Universe over a very large range of energies. The sources of these particles remain an open question, in particular when considering the highest energies of both the component considered to be of galactic origin, and the component associated to an extragalactic origin. One of the most limiting factor when studying cosmic rays is the deflection of charged particles by the magnetic field in the Universe. Photons are not affected by this effect, and are thus the main messenger used for astronomy as they point back in a straight line – or more precisely, following a gravitational geodesic –back to their source. Other, more recently observed messengers are now also used to perform astronomy : neutrinos and gravitational waves.

The electromagnetic spectrum extends from very low energies with radio wavelength, to very high energies with gamma-rays. Each observed band requires specific instruments developed to efficiently detect photons in their wavelength band of interest. The H.E.S.S. experiment observes the very high energy band corresponding to individual photons with energies of around 1 TeV. It uses the atmosphere as a screen to detect the very rare photons reaching Earth at this energy. Sources energetic enough to produce such photons are relatively rare. In the extragalactic sky, a category of sources sometimes able to do so are active galactic nuclei. In particular, active galactic nuclei ejecting a jet of relativistically moving particles emit detectable flux of very high energy photons. The processes occurring in the jet are still vastly unknown and the emissions are variable. In order to improve our knowledge of such objects, detailed observations are required. Optimally, temporally detailed observations with a multi-wavelength, and even multi-messenger, coverage would be very useful.

In this document I will present my work on active galactic nuclei variability as observed with the H.E.S.S. experiment. In chapter 1, I first explain what are active galactic nuclei and their classification. Then I focus on the sub-category of active galactic nuclei of interest for this work – Blazars – with an overview of the emission processes occurring in the relativistic jet and of the jet properties. The chapter 2 starts with an introduction to astronomical messengers of interest. It is followed by a description of the phenomena occurring in the atmosphere when a very high energy particle interacts in it. Finally, it goes over the properties of the H.E.S.S. experiments from its physical implementation to the details of the data analysis. The chapter 3

concerns the new software developments introduced to optimise the exploitation of observations of variable sources. Then chapter 4 mostly covers specific analyses of observations of active galactic nuclei flares obtained with the associated target of opportunity program in H.E.S.S. The chapter 5 presents a young project of systematic characterisation of the temporal properties of flaring events observed by H.E.S.S., and evaluates the usability of general estimators on light curves with variable binnings. Finally, chapter 6 is about a study I took part in, modelling the emission of both photons and neutrinos of TXS 0506+056 in a lepto-hadronic model. Using multi-wavelength data obtained contemporaneously with a neutrino detection correlated with TXS 0506+056, the emission of neutrino is predicted. It is then compared to the detection and IceCube sensitivity.

Chapter 1

Blazars

Sommaire

Active galactic nuclei are intense sources of electromagnetic radiations located in the extra-galactic Universe. While AGN are not the brightest sources in the Universe at every given times, they are very long lived and generally very bright. They also display important variability over long and short time scales. In this chapter we will first see the main properties of active galactic nuclei. Then we will do an overview of the main processes responsible for blazar emissions. Blazars are an important category of active galactic nuclei emitting photons up to the highest energies and will be the object of study in this document.

1.1 Active Galactic Nuclei

Active galactic nuclei, or AGN, are located at the center of some galaxies. They are responsible for an additional, non star-like, component in the spatial luminosity distribution of these galaxies. This can for example be seen in Figure 1.1 displaying the radial luminosity profile of an AGN in its host galaxy. A spatially extended component is produced by the stars of the host galaxy and a central, point-like component comes from the active nuclei. AGN electromagnetic emissions extend over a large variety of energies which can include radio, optical, X-rays, high and very high-energy (HE and VHE), ... Active galactic nuclei differ by the energy bands in which they emit and can be observed, and by the intensity of emissions. They can be classified based on their observational and inferred intrinsic properties.

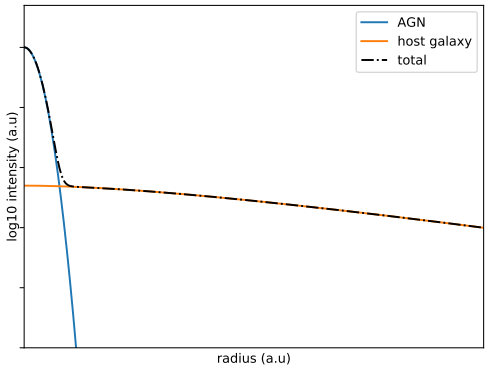

Figure 1.1: Schematic optical luminosity profiles of an AGN and its host galaxy. The host galaxy luminosity follows the star density, decreasing exponentially. The active galactic nucleus appears as a very localised luminosity peak. Luminosity profile obtained with the Wide Field and Planetary Camera 2 on the Hubble Space Telescope from real AGN can be found in [1].

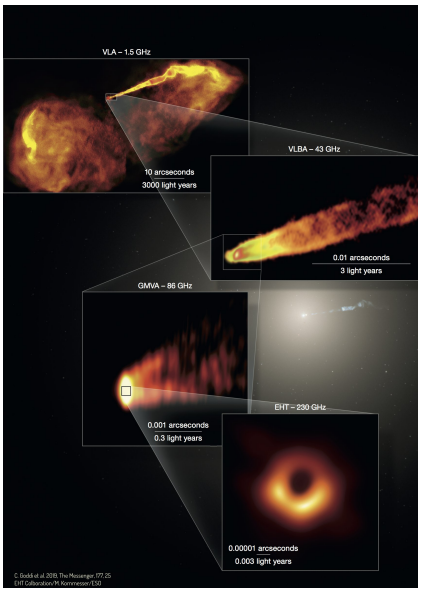

Figure 1.2: Radio observations of M87 at scales ranging from the full radio lobes to the acceleration region of the relativistic jet and EHT image of the central black hole. From [2]. Details on the EHT measurement can be found in [3].

1.1.1 General properties and classification

1.1.1.1 Current general AGN representation

The first observations of active galactic nuclei last century varied strongly in both observed properties and observation techniques used. Hence, at the time, those objects were categorized and studied independently. It is only in the 90s that a unified scheme was proposed in which all AGN are composed of the same main sub-parts with varying internal properties and orientation compared to the line of sight [4] [5]. It is now commonly accepted that AGN can be divided into two main morphologies differing by the presence of a relativistic jet.

An AGN is divided into :

- **A Super Massive Black Hole** (**SMBH**) located at the center of the nuclei. This SMBH mass is of the order of 10^6 to 10^9 solar masses ($M_\odot$). Measured masses obtained using spectroscopic reverberation-mapping[1] studies [6] can be found in the AGN Black Hole Mass Database[2]. Its mass and spin will be responsible for the geometry of the space around it and hence, control the accretion of matter into the black hole and subsequent ejections. The first direct observation of the SMBH of an AGN was performed recently by the Event Horizon Telescope. The deflected emission around the SMBH in the AGN at the center of the galaxy M87 allowed to see the shadow of the black hole as displayed in Figure 1.2 with the EHT 230 GHz image from [3].

- **An accretion disk** of in falling matter extended to one parsec away from the black hole. Accretion processes will increase the temperature of the in falling matter as it gets closer to the black hole. Light from the accretion disk comes from black body processes integrated over the full disk, i.e. from the innermost stable orbit to the external edge. The associated spectral energy distribution (SED) extends from optical to the highest energy of ultra violet light. Line emission from the disk components are also visible above the black body continuum [7][8]. Accretion efficiency varies between AGN and reflects differences in the structure of the flow and emission strength. The ratio of the disk luminosity L to the Eddington luminosity L_{Edd} [3] of the system seems to be directly linked to those differences.

- **A "torus"** of gas and dust surrounding the accretion disk. It is responsible for obscuration of the AGN nuclei and for infra-red photon emissions. The morphology of this gas and dust structure is still widely studied and vary between sources. For example a geometrically-thin disk in the accretion disk plane and a cone of dust out-going towards the polar region (see Figure 1.3) are favored by resolved observations of some AGN [9]. Observations of low luminosity sources such as the AGN located at the center of M87 show none of the infra-red radiations expected from the torus [10] implying that it can be absent from such sources.

[1] Uses the delay between a change in the accretion disk luminosity and the feedback in the BLR luminosity to estimate the distance between the black hole and the BLR. Then this information is combined with the knowledge of the projected speed of the BLR gas obtained with the width of the emission lines to deduce the black hole mass.

[2] http://www.astro.gsu.edu/AGNmass/

[3] See the Eddington luminosity boxed text

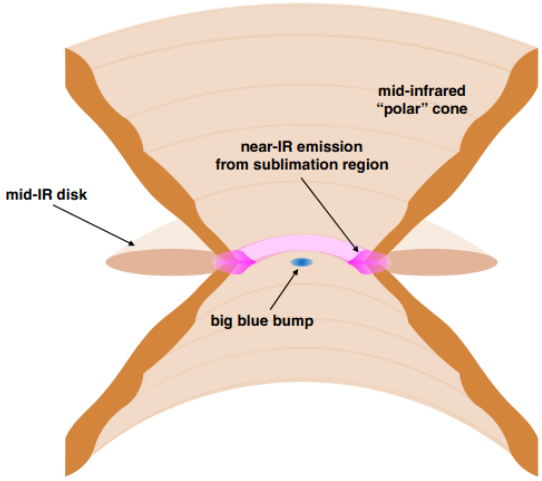

Figure 1.3: AGN infrared emission in a model with : a geometrically-thin disk in the accretion disk plane (light brown) and an outflow of dust in the form of a hollow cone towards the polar region (dark brown). The "big blue bump" is a signature of the optical light emitted by the accretion disk. From [9].

- **A Broad Line Region** (**BLR**), **a Narrow Line Region** (**NLR**) and **a gas corona**. The latter is located around the accretion disk. It reprocesses the emissions from the disk to emit X-rays through inverse Compton scaterring (see Section 1.2.1.1) by hot electrons. The BLR and the NLR are regions containing ionised gas which will be responsible for emissions lines. The NLR extends quite far from the black hole and contains gas with velocities of hundreds to a thousand kilometres per second [11]. The BLR is located closer to the black hole and is characterised by velocities a factor ten above the ones of the NLR [12] leading to broader emission lines.

Finally, around 10% of AGN possess an additional feature :

- **A relativistic jet** leaving the black hole vicinity in the direction perpendicular to the accretion disk plane. The jet is composed of matter launched by the SMBH from the accretion disk, and collimated over very long distances up to the Megaparsec (Mpc) scale. The properties of the jet evolve strongly when going away from the black hole as seen on radio images Figure 1.2. Intense radio emission is a signature of jetted AGN visible in all direction. It comes both from the well collimated jet close from the black hole, and from farther regions such as the extended radio lobes. The relativistic jet is also the origin of beamed photon emissions covering a large fraction of the electro-magnetic spectrum and visible in a limited cone in the jet direction. This beamed emission will be covered in more details in the sections 1.1.2 and 1.2.

In this simplified model, the AGN displays two symmetries. First a reflection symmetry around the plane containing the accretion disk and the black hole. Second, a rotational symmetry around the axis perpendicular to the previous symmetry plane and passing through the central black hole. It took a long time for such a model to appear leading to a complex classification linked to observed differences and a late unification of AGN.

Eddington luminosity

The Eddington luminosity is the maximum luminosity of an accreting body in hydrostatic equilibrium. It is obtained by compensating the gravitational pressure with the radiation pressure in the object. To derive it we can use F_{rad} the local radiation flux, i.e. the local flux of energy carried by photons.

Noting κ the opacity of the medium, i.e. the fraction of energy flux absorbed by the medium per unit density and unit length, and knowing that the momentum of a photon is its energy divided by the celerity of light c we can deduce the momentum locally transferred from the radiation field to particles per unit time $\frac{dp_+}{dt}$:

$$\frac{dp_+}{dt} = \frac{\kappa F_{rad}}{c} \tag{1.1}$$

The momentum locally transferred from the gravitational interaction is

$$\frac{dp_-}{dt} = -\frac{GM}{r^2} \tag{1.2}$$

with G the gravitational constant, M the local effective mass of the object and r the distance from the center of mass. In hydrostatic equilibrium the total momentum evolution is null, so :

$$F_{rad} = \frac{cGM}{\kappa r^2} \tag{1.3}$$

To obtain the Eddington luminosity of the object, one then needs to integrate over the object surface. In the spherical and homogeneous case, M, κ and r are constant and the surface is $4\pi r^2$ giving :

$$L_{Edd} = \frac{4\pi cGM}{\kappa} \tag{1.4}$$

Considering that the gravitational potential is fully converted into radiation in an accretion system, the Eddington luminosity becomes equivalent to an upper limit to the accretion rate. The classical Eddington limit L_{Edd} derived previously is an oversimplification when applied to non-spherical and inhomogeneous systems such as accretion disks [13].

1.1.1.2 Observational classification and limits

In 1963, M. Schmidt reports the observation of "a star-like object" in coincidence with a radio source and a jet [15]. Based on the observed emission lines the favoured hypothesis is an extragalactic source at a redshift of 0.158. Later that year, this kind of objects becomes known as quasi-stellar radio sources, abbreviated quasars nowadays.

The names associated to AGN multiplied depending on the observation technique and wavelength. As a first cause, observation techniques are not sensitive to the same range and strength of sources. For instance, very high energy photons are absorbed by the extragalactic background light (See Section 2.1.3.2) which limits the range of detection up to redshifts of 1 even today. Conversely, radio survey observed sources up to redshift 6. Another issue arises with the complexity of the sources. Each wavelength is affected by a different sub part of the AGN leading to two sources looking the same for one observer but different for a second. For example, optical is sensitive to obscuration of the accretion disk by the torus while mid infra-red is mostly unaffected. A final point concerns the orientation of the observed AGN. The lack of spherical symmetry means that two intrinsically equivalent AGN observed from different directions may

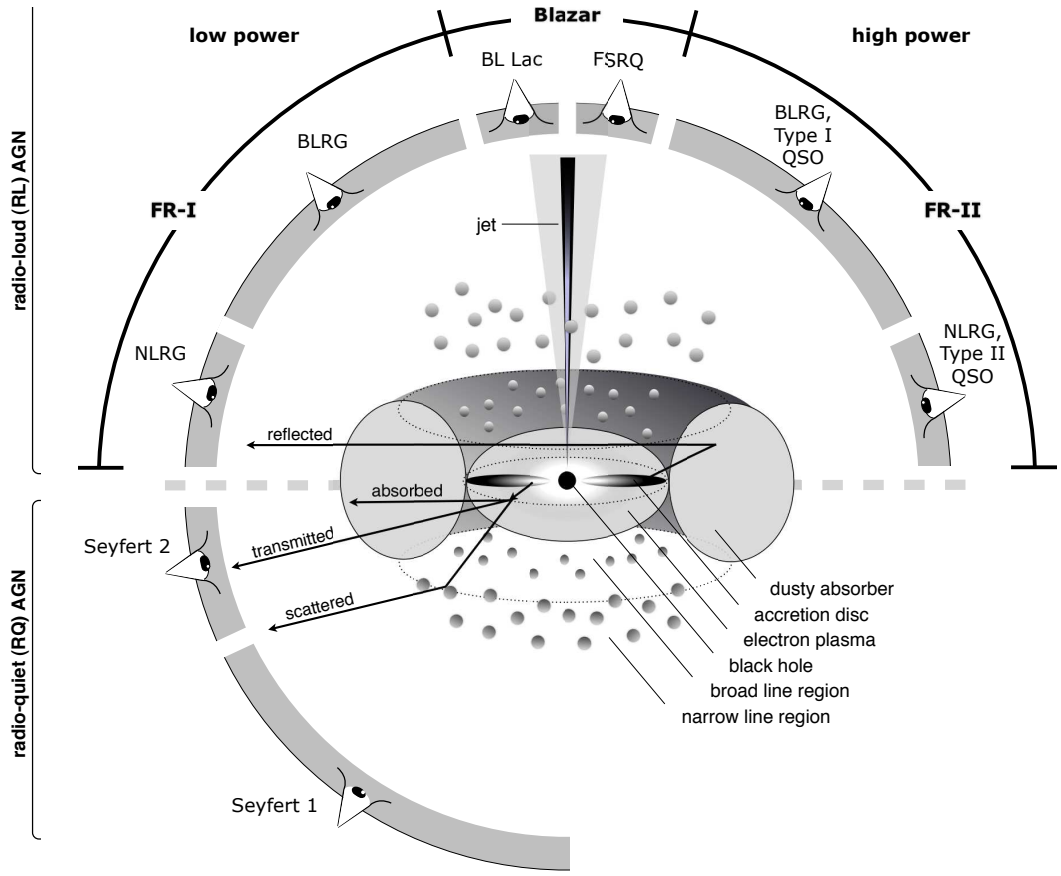

Figure 1.4: Commonly used AGN classification and associated properties. Separations depend on the presence of a jet, the visibility of the broad line region, the visibility of the jet beamed radiations and the power of the AGN. Abbreviation used : NLRG - Narrow Line Radio Galaxy; BLRG - Broad Line Radio Galaxy; QSO - Quasi Stellar object; FSRQ - Flat Spectrum Radio Quasar. From [14]

not be seen as the same. This concerns in particular the beamed emissions from the jet and absorption by the torus.

In the end, more than 53 categories of AGN were created as seen in the table 1 from [16], which is a full review on the selection effects and AGN properties. With the unification of AGN, the number of categories used decreased and is now closely linked to :

- The presence of a jet
- The bolometric luminosity of the AGN
- The orientation of the system with respect to the line of sight

The Figure 1.4 shows this classification taking all 3 criteria into account.

The sources of interest for this document will be blazars. A blazar is an AGN containing a jet and observed in the direction of the jet. The bolometric luminosity is not included in the blazar definition and corresponds to a sub-division of this category between FSRQ (high power) and BL Lac objects (low power).

1.1.2 Blazar observational properties

Since the observer is in the direction of the relativistic jet, the beamed light radiated inside the jet will be visible. In the case of BL Lac objects it will even be the dominating contribution to the majority of the electromagnetic spectrum. For FSRQ, a stronger emission from other components of the AGN will be visible along with the jet. Hence FSRQ also display emission lines [17].

Due to important selection effects, the properties of the detected blazars depend strongly on the observed energy band. At very high energy, the compilation of sources TeVCat[4] contains a total of 74 blazars. Out of those, 8 are FSRQ, 63 are BL Lac objects and 3 are of undefined category. Even among the BL Lac objects, the majority (52) is composed of HBL (defined in the next section), a sub-category emitting at higher energies than the others. While BL Lac objects are more numerous in the VHE sky, they are detected at shorter distances compared to FSRQ. The former are observed up to a redshift of 0.5 while FRSQ are detected up to redshift close to 1. At high energy, the 4FGL-DR2 [18] catalogue[5] compiles all the sources detected by the *Fermi*-LAT instrument over 10 years of mission. It compiles information on 3437 blazars including 730 FSRQ, 1190 BL Lac objects and 1517 undefined blazars. An AGN specific catalogue, the 4LAC [19], contains additional information on the blazars in the 4FGL (but is limited to a smaller dataset, corresponding to the 4FGL-DR1 covering only 8 years of mission). The FSRQ are located up to redshift above 3, with a distribution peaking at a redshift of 1. In the case of BL Lac objects, the distribution peaks at a redshift of 0.5 but some are still detected between a redshift of 2 and 3. About half of the tested blazars are found to be variable in the 4LAC, with the fraction being significantly higher for FSRQ compared to BL Lac objects. All the TeVCat AGN are included in the 4LAC.

[4] http://tevcat.uchicago.edu/
[5] https://heasarc.gsfc.nasa.gov/W3Browse/fermi/fermilpsc.html

1.2 Relativistic jet emission

The spectral energy distribution (SED) of the jet is characterised by two bumps. The low energy component extends roughly from the radio to the X-rays while the high energy component extends from the hard X-rays to very high energy. An example of such a SED is visible in Figure 1.5. The lower energy component is generally accepted to originate from synchrotron emission from electrons in the jet. The high energy bump origin is still unsure and possibilities will be addressed in the following sections. The energy at which each bump reaches its maximum is source-dependent. The energy of the maximum, or more often the peak frequency ν_{peak}, of the synchrotron emission is used to differentiate FRSQ and sub-categories of BL lac objects as follows [20] [21] :

- FSRQ : ν_{peak} ranging from 10^{12} Hz to 10^{14} Hz
- BL lac : ν_{peak} ranging from 10^{12} Hz to 10^{18} Hz
  - LBL (Low frequency peaked BL lac) : $\nu_{peak} \sim 10^{12} - 10^{14}$ Hz
  - IBL (Intermediate frequency peaked BL lac) : $\nu_{peak} \sim 10^{15} - 10^{16}$ Hz
  - HBL (High frequency peaked BL lac) : $\nu_{peak} \sim 10^{17} - 10^{18}$ Hz

It was found that the synchrotron peak frequency of blazars decreases when the luminosity increases but that the dependence is stronger for BL lacs objects [21].

Another important piece of information about blazars is that they are strongly variable. As seen in Figure 1.5, PKS 2155-304 displayed variations of flux of more than an order of magnitude with for example the flux at 1 TeV measured at both $\sim 3.10^{-15}$ W/m^2 and $\sim 2.10^{-13}$ W/m^2. This high flux state of PKS 2155-304 was observed in 2006 during an historically strong flare at very high energies. Observations by H.E.S.S. at this time led to detailed enough light curves to resolve minute scale variability [22]. Variability is also seen at day [23][24] to year [25][26] time scales.

Understanding the origin of those observations is particularly challenging as coverage of the full energy band is impossible, as is the coverage of the full time evolution of the sources especially when considering the need for simultaneity of the multi-wavelength datasets. Therefore, a wide variety of models of the emission from the jets still exist with varying geometry, composition and environment.

1.2.1 Particle composition issue

A key question is what particles are present in the jet and relevant to the observational signature of AGN. Since the jet needs to be neutral it must contain nuclei and electrons but the photons can originate from a sub-ensemble of the available particles. One popular family of models, the leptonic models, considers a population of relativistic electrons to be at the origin of both the low and high energy bumps. Alternatively, lepto-hadronic models still explain the low energy bump with electrons while also including relativistic protons dominating the high energy bump emission. The hadronic scenario can also theoretically be extended to include nuclei heavier than protons.

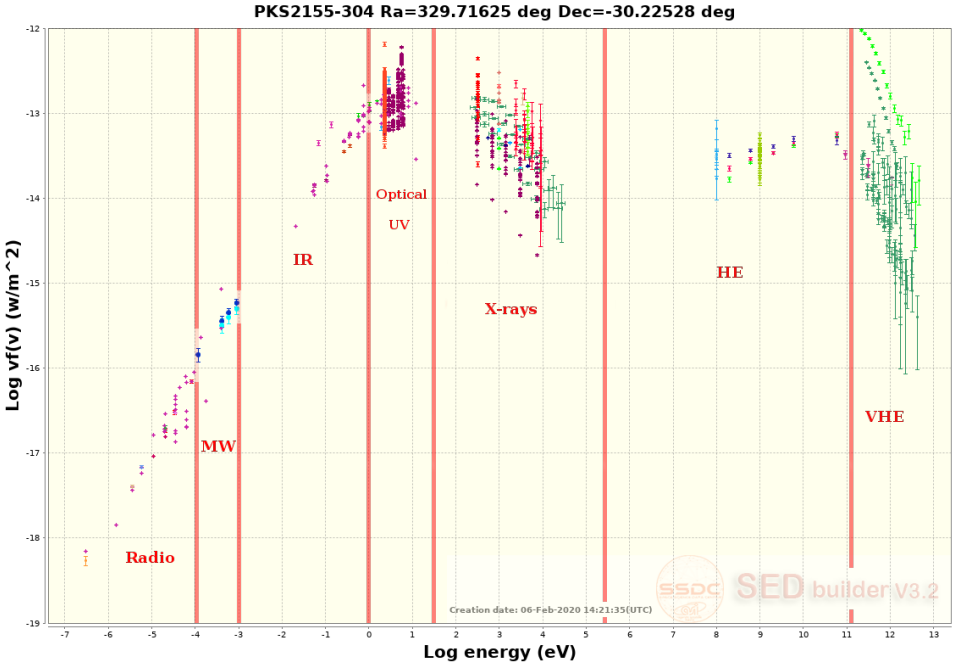

Figure 1.5: SED of PKS 2155-304 extracted from SED Builder (https://tools.ssdc.asi.it/SED/)

1.2.1.1 Leptonic emission processes

Leptonic models are an elegant way to represent the general blazar SED as they use only one population of particles, the electrons, which are light hence easy to accelerate and interact only in two relevant ways. Furthermore, each of these interactions is fully responsible for one of the bumps. The global neutral charge of the jet is guaranteed by a population of low energy ("cold") nuclei. It should be noted that positrons are also expected to be produced near the black hole through photon-photon annihilation into electron-positron pairs [27]. Positrons will act in the same way as electrons as they share the same mass and absolute electric charge.

Electron synchrotron

Charged particles accelerated in a magnetic field will radiate photons. This process, called synchrotron radiation, is a well known phenomenon that appears naturally when considering the interaction vertex of the electron in the magnetic field and applying laws of conservation. Indeed the interaction is the following :

$$\gamma_v + e^- \rightarrow \gamma_r + e^- \tag{1.5}$$

where γ_v is a virtual photon and γ_r is the real photon created to conserve energy and momentum. If the electron is moving at non-relativistic speed it is likely to "see" the medium at the origin of the magnetic field and hence to transfer the needed energy momentum into the medium instead of emitting a real photon. This is why synchrotron emission is efficient only for particles moving at relativistic speed. A more common way to see it is by considering the perturbation of the electromagnetic fields by the moving charge. When the relativistic charged particle is deflected, the field perturbation in the direction away from the deflection cannot adjust to the new particle direction as it would require supra-luminal information transfer. Consequently the

electromagnetic field perturbation separates from the particle itself in the form of a photon. See Figure 1.6.

Considering a single electron, some of the main properties needed to represent its synchrotron radiations can be derived. See, e.g., "High Energy astrophysics" by Malcom S. Longair [29]. The properties which will interest us here are the rate at which energy is radiated by the particle, the spacial distribution of the emission and the energy of the individual photons. To start, the radiation energy loss rate is the energy radiated by the particle as synchrotron per unit time. It can be given using the Thomson cross-section σ_T, the energy density of the magnetic field u_B and β as follow :

$$\frac{dE}{dt} = -2\sigma_T c u_B \beta^2 \gamma^2 sin^2\theta \tag{1.6}$$

with :

$$\sigma_T = \frac{e^4}{6\pi\epsilon_0^2 c^4 m_e^2} \quad (1.7a) \qquad u_B = \frac{B^2}{2\mu_0} = \frac{B^2 c^2 \epsilon_0}{2} \quad (1.7b) \qquad \beta = \frac{v}{c} \quad (1.7c)$$

with e the electron charge, B the magnetic field strength, c the speed of light, m_e the electron mass, v the electron velocity, $\gamma = (1-(\frac{v}{c})^2)^{-1/2} = (1-\beta^2)^{-1/2}$ the electron Lorentz factor and θ the pitch angle between the electron velocity and the magnetic field line.

For a relativistic electron with lorentz factor γ, the synchrotron radiation is beamed in a cone of radius $1/\gamma$ containing most of the radiated power.

The information on the frequency at which the energy is radiated can be obtained with two approaches. A simplified view is to consider the frequency at which most of the radiation occurs :

$$\nu = \gamma^2 \frac{eB}{2\pi m_e} sin\theta \tag{1.8}$$

obtained by the Fourier transform of the pulse observed when the cone of emission with opening $1/\gamma$ crosses the line of sight. Approximating the whole synchrotron by this value is often enough to obtain good order of magnitude estimates. A full, and complex, computation leads to a SED plotted in Figure 1.7 where the critical frequency ν_c was used as the natural scale for the frequencies.

$$\nu_c = \frac{3}{2}\gamma^2 \frac{eB}{2\pi m_e} sin\theta \tag{1.9}$$

In astrophysics we are mostly interested in the global emission from a population of relativistic electrons. Considering that the density of electrons at energy E follows a power law as $N(E) \propto E^{-p}$, the resulting synchrotron SED will be a power law with index $(1-p)/2$.

One last important effect to be considered is synchrotron self absorption. At any frequency, the emitting electrons can re-absorb the synchrotron radiation if the brightness temperature becomes high compared to the particles temperature. The brightness temperature associated to a flux of photons is the temperature of a black body that would emit radiation with the same intensity. A full computation of the frequency dependent absorption coefficient goes outside of the scope of this part. Overall, this effect makes the lower energy part of the SED into a power law of index independent of the initial electron population and reduces the flux at this energy as shown in Figure 1.8.

Inverse Compton

The inverse Compton effect is a scattering interaction between a high energy electron and a low energy photon. The probability of interaction of the photon and the electron are given by

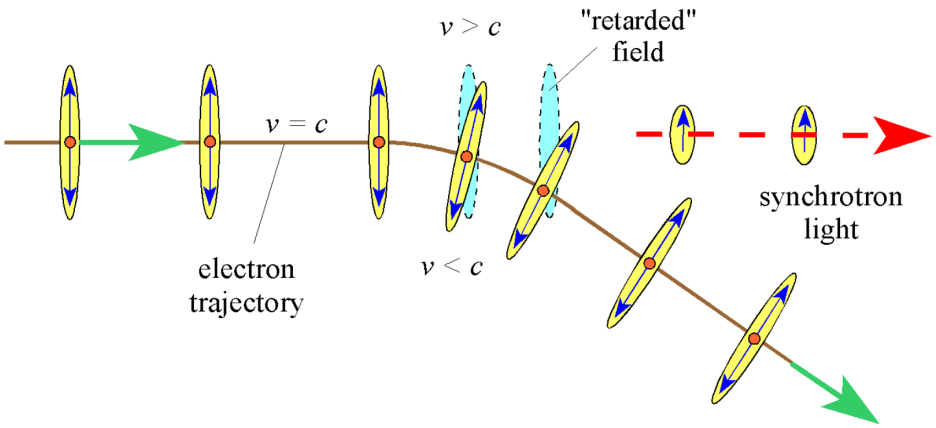

Figure 1.6: Synchrotron emission from a charged particle deflected by a magnetic field. The electron is represented by a red dot. The electromagnetic field perturbation contracted by special relativity is shown as a yellow area. From [28].

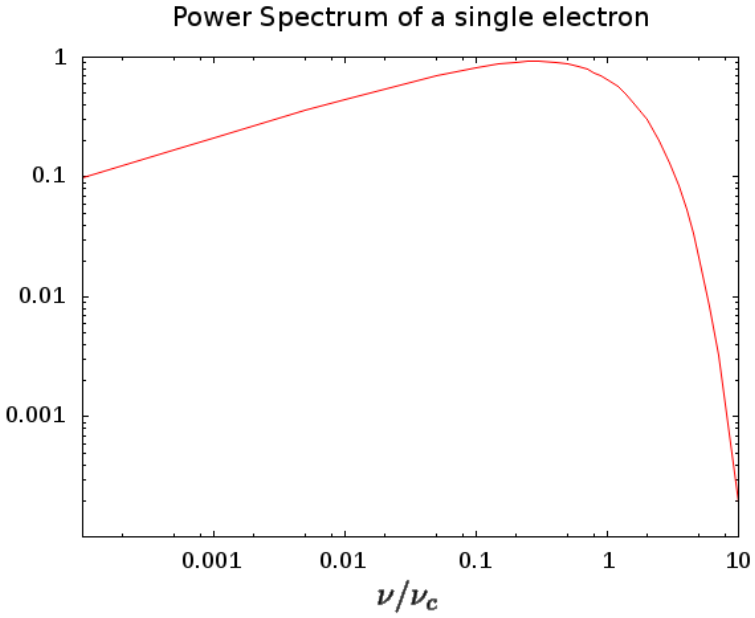

Figure 1.7: Synchrotron spectrum for a single electron. The frequency is scaled by the critical frequency ν_c.

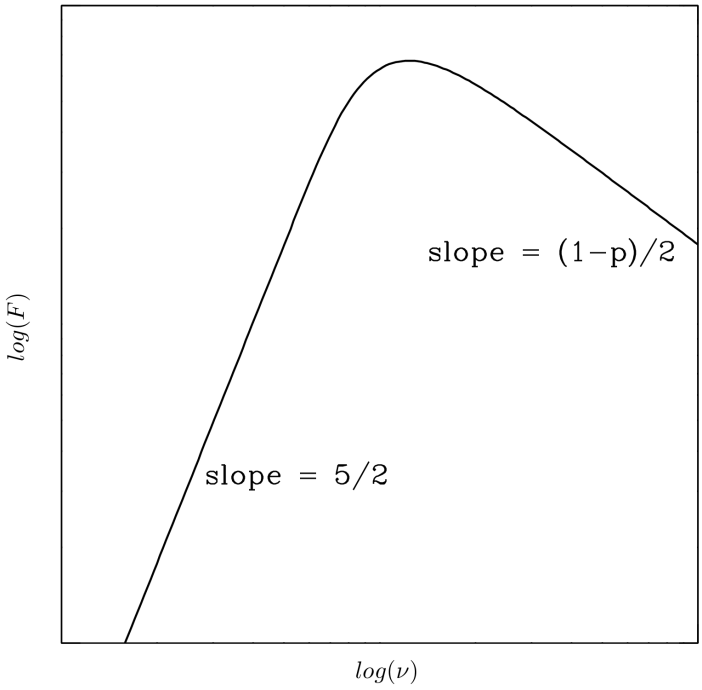

Figure 1.8: Self-absorbed synchrotron spectra produced by a population of electrons distributed with a power law of index $-p$.

the Klein-Nishina cross section [30], here integrated over the solid angles :

$$\sigma_{KN} = \frac{3}{4}\sigma_T\left(\frac{1+\epsilon_\gamma^*}{\epsilon_\gamma^{*3}}\left[\frac{2\epsilon_\gamma^*(1+\epsilon_\gamma^*)}{1+2\epsilon_\gamma^*} - ln(1+2\epsilon_\gamma^*)\right] + \frac{ln(1+2\epsilon_\gamma^*)}{2\epsilon_\gamma^*} - \frac{1+3\epsilon_\gamma^*}{(1+2\epsilon_\gamma^*)^2}\right) \tag{1.10}$$

with σ_T the Thomson cross section previously defined and ϵ_γ^* the energy of the photon in units of $m_e c^2$ in the electron rest frame.

The inverse Compton interaction can be approximated into two regime depending on the value of ϵ_γ^* :

- Thomson regime : The energy of the photon is small compared to the mass energy of the electron in the electron rest frame, namely $\epsilon_\gamma^* \ll 1$. Then, $\sigma_{KN} \to \sigma_T$ and the photon will be scattered without energy modification. Hence, the final photon energy $E_{\gamma f}$ is simply the initial photon energy $E_{\gamma i}$ Lorentz transformed twice. Once to the electron rest frame before interaction and once back to the original frame after interaction. Consequently $E_{\gamma f} = \gamma_e^2 E_{\gamma i}(1+\beta cos\theta_f^*)(1-\beta cos\theta_i)$ with γ_e the Lorentz factor of the electron, θ_i the initial angle between the electron and photon trajectory and θ_f^* the angle after interaction in the electron rest frame.

- Klein-Nishina regime : In this case, $\epsilon_\gamma^* \gg 1$. σ_{KN} decreases with the photon energy. Additionally, the energy of the photon after scattering is independent of the initial energy and incident angle and becomes $E_{\gamma i}^* = m_e c^2$. The final photon energy is hence $E_{\gamma f} = m_e c^2 \gamma_e (1+\beta cos\theta_f^*)$.

The dependency on the angles will disappear when considering the average effect on a population of relativistic electrons and isotropic photons. The important distinction will then be that in the Thomson regime the photon energy is boosted as γ_e^2 and is proportional to the initial energy while in the Klein-Nishina regime the energy increases as γ_e and is proportional to $m_e c^2$.

1.2.1.2 Hadronic emission processes

Lepto-hadronic models complexity increases exponentially with the number of additional particles and interactions considered. In a simple approach, a population of relativistic protons are considered in the jet while dense targets for hadron-hadron interactions are absent. Adding heavy nuclei and dense hadronic regions would induce processes such as fissions, Z/W productions, ... The following will assume a simple model with only proton-photon interactions. As protons are heavier than electrons they are harder to accelerate but also to cool down and can hence reach higher energies.

Meson production

The dominant output of the interaction between a high energy proton and a low energy photon is pion production if the energy available is above the threshold. Pions (π) are the lightest mesons, composed of a pair of u or d quark/anti-quark. The neutral pion (π^0) mass is $m_{\pi^0} = 134$ MeV.c^{-2} and the charged pions ($\pi^\pm$) mass are $m_{\pi^\pm} = 139$ MeV.c^{-2}. From kinematic arguments, one can see that the proton threshold energy for this interaction is :

$$E_{p,th} = \frac{m_p m_\pi (1 + m_\pi/2m_p)}{2E_\gamma} \approx 10^{17} \left[\frac{E_\gamma}{1 \text{ eV}}\right]^{-1} \text{ eV} \tag{1.11}$$

The inverse dependency on the target photon energy is quite important, especially when taking into account the shape of the $p\gamma$ cross-section shown in Figure 1.9. The cross-section [31] is peaked at the threshold then lower but non-vanishing at higher energies. As a result, the shape of the SED of the target photon field will directly influence the energy of the interacting proton and therefore the energy distribution of the produced pions. Generally, each interaction can produce multiple pions. Noting n_0 the number of neutral pions produced and $n_\pm$ the number of pairs of charged pion :

$$p + \gamma \rightarrow p + n_0\pi^0 + n_\pm(\pi^+ + \pi^-) \tag{1.12}$$

or

$$p + \gamma \rightarrow n + n_0\pi^0 + n_\pm(\pi^+ + \pi^-) + \pi^+ \tag{1.13}$$

The neutral pions will then decay into two photons while the charged pions will decay into muons and then electrons:

$$\pi^0 \rightarrow \gamma + \gamma \rightarrow EMshowers \tag{1.14}$$

$$\pi^+ \rightarrow \mu^+ + \nu_\mu \rightarrow e^+ + \nu_e + \bar{\nu_\mu} + \nu_\mu \tag{1.15}$$

$$\pi^- \rightarrow \mu^- + \bar{\nu_\mu} \rightarrow e^- + \bar{\nu_e} + \nu_\mu + \bar{\nu_\mu} \tag{1.16}$$

Electromagnetic showers, noted $EMshowers$ above, are cascades of photons, electrons and positrons generated in this case by the high energy photons from the pion decay. More details can be found in subsection 2.2.1.

To summarise, the meson production through proton-photon interaction will temporarily pro-

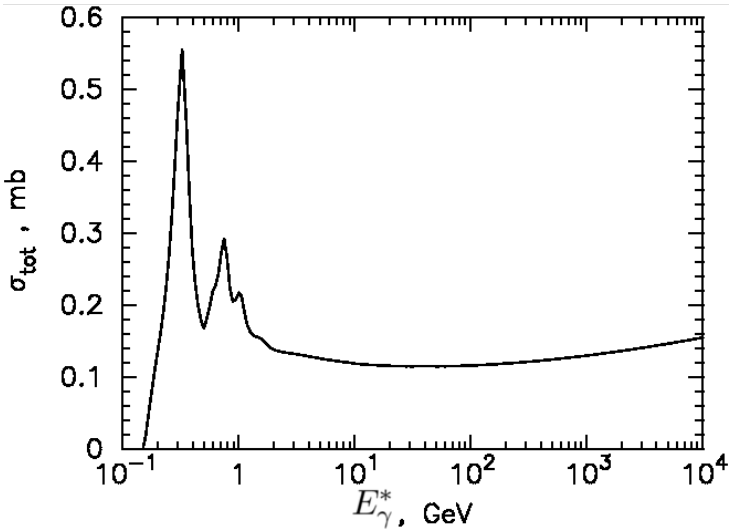

Figure 1.9: Photon-proton cross-section for pion production. Obtained using the routine of the code SOPHIA [32]. The abscissa is the energy of the photon in the proton rest frame. From [31].

duce π^{0+-} and $\mu^{\pm}$ and a final output comprised of neutrons, high energy photons, $e^{\pm}$ and neutrinos.

Bethe-Heitler

Under the threshold of the meson production the dominant proton-photon interaction is called Bethe-Heitler. It consists in the production of pair of electrons and positrons :

$$p + \gamma \rightarrow p + e^+ + e^- \tag{1.17}$$

Charged particles synchrotron

All the new charged particles introduced previously in this section will, as the electrons in the leptonic case, emit synchrotron photons. The process is similar to the electron case but the electron mass needs to be replaced by the mass of the considered particle. Additionally the particles will generally reach significantly higher energies than the primary electrons. Indeed, lepto-hadronic models have shown that the electrons required to produce the low energy bump reach gamma factor of the order of 10^{4-5} while the protons responsible for the high energy bump have gamma factor going as high as 10^{8-9} (see, e.g. [33]) to which one needs to add the factor 2.10^3 between their masses. Secondaries will also carry large energies. For example in the case of a single pion production from a $p+\gamma$ interaction, the pion will carry a fraction close to $\frac{m_\pi}{m_p} \approx 0.14$ of the initial proton energy. From equations 1.6 and 1.7a we can see that $dE/dt \propto \gamma^2/m^2$. This implies that heavy particles from hadronic models, such as the protons, will only emit significant synchrotron at high energies. Even at the same γ/m ratio, the heavier particles will loose a smaller fraction of their energy. The frequency of the emission will also be increased since $\nu_c \propto \gamma^2/m$ (equation 1.9).

1.2.1.3 Dopler boosting

Up to this point, every process was discussed in the relativistic jet rest frame. Noting Γ the Lorentz factor associated to the jet and ϕ the angle between the jet and the observer in the observer rest frame, the Doppler factor is in the small angle approximation :

$$\delta_D = \frac{1}{\Gamma(1-\beta cos\phi)} \tag{1.18}$$

Time dilation and spatial compression effects will occur when evaluating the emission in the jet rest frame (subscript j) compared to the observer rest frame (subscript o). Due to the time dilation, durations observed in the jet frame will be reduced when going to the observer frame with two important effects :

- Increase of the frequency ν, and associated energy $E = h\nu$, of the particles and photons : $\nu_o = \delta_D \nu_j$
- The frequency of arrival of particles will be multiplied by δ_D for each individual trajectories

The spatial compression will affect the direction of the particles to be oriented along the jet axis as seen in Figure 1.10. Since the angular dispersion is a two dimensional spatial quantity, it will be divided δ_D^2.

From this we can see that the energy distributions will be shifted by a factor δ_D and the fluxes by a factor δ_D^3.

These ideas can be pushed a bit further when considering the intensity in the jet. It has been shown that $\frac{I(\nu)}{\nu^3}$ is a Lorentz invariant [34] with $I(\nu)$ the intensity at frequency ν. We get:

$$\frac{I_o(\nu_o)}{\nu_o^3} = \frac{I_j(\nu_j)}{\nu_j^3} = \frac{I_j(\nu_j)}{(\nu_o/\delta_D)^3} \Rightarrow I_o(\nu_o) = I_j(\nu_j){\delta_D}^3 \tag{1.19}$$

The full intensity is then obtained by integrating over the frequencies :

$$I_o = \int_0^{+\infty} I_o(\nu_o) d\nu_o = \int_0^{+\infty} {\delta_D}^3 I_j(\nu_j) \delta_D d\nu_j \tag{1.20}$$

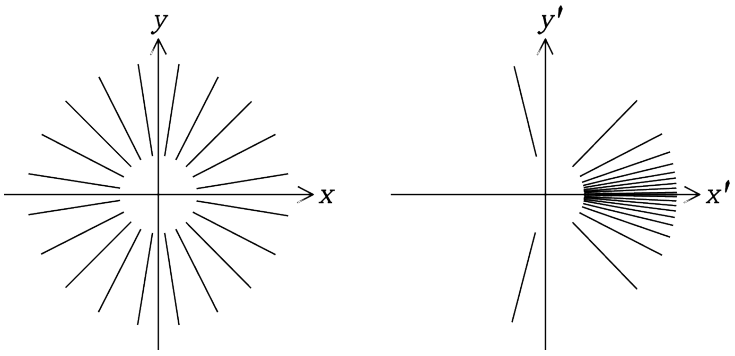

Figure 1.10: Relativistic beaming. Left : isotropic emission in the particle rest frame. Right : same emission seen in the frame where the particle moves at relativistic speed toward the positive values of x'.

$$I_o = \delta_D{}^4 I_j \tag{1.21}$$

Implying that the full jet power will be boosted as the power 4 of the relativistic Doppler factor.

1.2.1.4 Observables

To identify between a leptonic or lepto-hadronic origin for AGN observations, one needs to look at specific spectral feature or potential unique messengers.

In fully leptonic models, the only expected observables are the synchrotron and inverse Compton photons. The electrons will be deflected by the intergalactic magnetic field so they cannot be associated with the source and are never directly observed in the extragalactic sky[6]. Difference in the SED of blazars between leptonic and lepto-hadronic models are expected at the high energy bump. For example, if we consider that the high energy bump is fully dominated by proton synchrotron, one expects a simple power law followed by a cut-off. The cut-off could originate either from a limit to the energies reached by the protons or from absorption of the highest energy gamma-rays. Additional synchrotron from, e.g., muons can also contribute at very high energy inducing an up turn in the SED compared to a simple proton synchrotron solution [35].

Neutrinos from meson decay are a promising indicator of hadronic interactions. They are not deflected by magnetic fields and interact weakly in matter implying that they can be traced back to the source and are visible even if they cross, e.g., gas and dust clouds. The first association of a single neutrino with an AGN occurred in 2017. At that time the detector IceCube observed a neutrino event IceCube-170922A in a direction consistent with the blazar TXS 0506+056 which was experiencing a long period of increased gamma-ray emissions that year. The spatial and timing agreement between the two led to an association at a 3 sigma confidence level [36]. Later studies searched for the possibility of associating clusters of neutrinos from IceCube archival data with the catalogued position of blazars. A 3 sigma association was found between the neutrinos arrival direction and IBL/HBL positions [37].

1.2.2 Geometry and environment effects

It was quite evident when developing the possible interactions possible in the jet that the output would be dependent on the properties of the emission region, of the jet and of its environment. Some examples of the possibilities will be highlighted.

1.2.2.1 Number of emission regions

Not all the jet participates to the observed emission at a given time but it is possible to have multiple regions of the jet active simultaneously. In such a case, the full jet SED will be the superposition of the individual SED. This could lead to wider bumps due to the superposition of shifted SED; uncorrelated low and high energy bumps if one region dominates at low energy and another at high energy; uncorrelated variability depending on the wavelength; ...

[6]The deflected electrons will produce gamma-rays around their source. Halos created this way are searched for and would constrain the intergalactic magnetic field.

1.2.2.2 Jet geometry

In cases when emissions from the jet cannot be approximated as coming from a single uniform region, the question of the spatial disposition of the emitting medium becomes important. The multiple region models grants two potential ameliorations compared to one-zone models : they can fit a wider variety of observations and they are often motivated by questions on acceleration processes, energy budget, opacity[7],... Two examples of models using specific geometries are described in the following paragraphs.

The homogeneous two zone model [38] was introduced to be coherent with the short time variability of blazars. Here, one zone is located at a shock front in the jet and houses acceleration of electrons. Particles from the acceleration zone will then escape downstream into an extended region called the radiation region where most of the synchrotron radiation will occur. This is schematised in Figure 1.11. Variability is hence controlled by a relatively small region but the total emission remains consistent with the usually observed synchrotron SED.

The two-flow model [39] considers a highly energetic electron/positron beam surrounded by a lower energy proton/electron beam (see Figure 1.12). This model is interesting as it reduces the total energy budget of the jet while still including particles energetic enough to produce high energy photons. Reducing the energy budget of the jet means reducing the needed accretion rate efficiency in the AGN accretion disk which can be necessary for the disk stability. Each flow interacts with the other one leading to an evolution of the jet properties along its axis including self acceleration effects. This model was studied numerically while also including photon fields from other regions of the AGN leading to information on the spatial origin of the different components of the jet SED [40].

1.2.2.3 Environment

The local environment of the jet will affect both emission from the jet and absorption of said emission with interactions such as :

- Inverse Compton on an external photon field : The inverse Compton effect detailed in section 1.2.1.1 can occur either on the synchrotron photon from the jet itself, in this case we speak of synchrotron self-Compton (SSC), or from photons coming from outside the jet. External photon fields can for example originate from the accretion disk, the dusty torus or the BLR. It is important to consider the Lorentz transformation from the AGN rest frame to the jet emission region rest frame. Indeed, the photon energy and direction distribution relevant to the inverse Compton is the one in the jet rest frame. From this it can be concluded that the external photon field contribution to the inverse Compton will be strongly dependent on the emission region distance from the SMBH. Indeed, in order

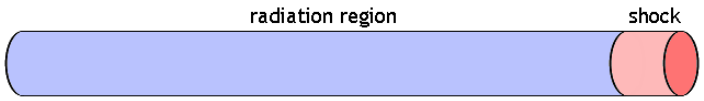

Figure 1.11: Mono dimensional two zone homogeneous jet model. Electrons are accelerated in the shock area (red) before escaping downstream to the radiation area (blue). Electrons in the radiation area will stay long enough to cool down fully.

[7] In order to be observed, the photons produced in the jet need to escape the emission region and the source. Opacity affecting the radiation thus needs to be limited.

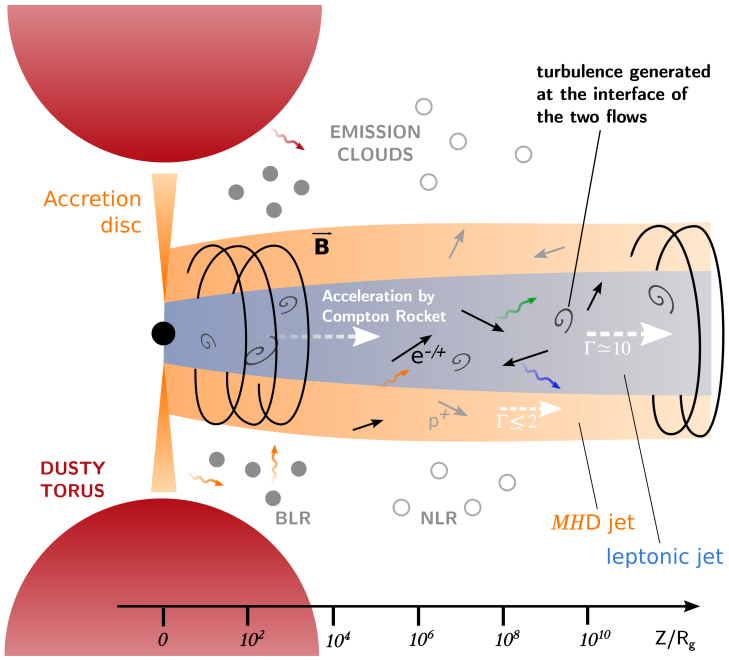

Figure 1.12: Blazar in the two-flow model. The MHD (Magneto-Hydro Dynamic) jet surrounds a highly relativistic electron/positron jet. Feedback between the two flows is particularly important to particle acceleration and structure stability. The "Compton rocket" is a self acceleration effect due to the interaction between the inner and outer flows. From [40].

for the target photon field to be dense enough the emission region needs to be close to their source [41].

- Pair production on BLR photons : If the emission region of very high energy gamma-rays is located closer to the central black hole than the BLR, this gamma-rays will encounter a dense low energy photon field from the BLR. When this happens, pairs of e^+/e^- will be produced by interaction of gamma-rays with BLR photons. This process can significantly reduce the flux at the highest energies.

- Jet cloud collisions [42]: A gas cloud can occasionally cross the jet. When this happens, the jet may be temporarily deflected or slowed. Alternatively, if the jet is powerful enough, the cloud can be disrupted and feed the jet [43].

Chapter 2

Very high energy astronomy with imaging atmospheric Cherenkov telescopes

Sommaire

Astronomy is a domain of physics whose goal is to observe the variety of signals coming from the Universe. This is a complex task as there is a variety of messengers to observe at various energies. To do so a large number of observation techniques were developed. In the following, I will first introduce the important properties of the messengers relevant to VHE astronomy. Then I will cover the topic of atmospheric showers as they are key to the VHE gamma-ray observation techniques. Finally I will introduce the H.E.S.S. experiment in which my work was performed.

2.1 Very high energy messengers

Earth is constantly exposed to a stream of particles and perturbations coming from the Universe. These messengers come from any distance from the Sun to the limits of the visible Universe. They can do so either directly, in a straight line, or after coherent or random deflections. Cosmic rays, neutrinos and photons form the majority of observed signals in modern Astronomy. Out of those, only photons were always observed as we are biologically equipped to detect them while other particles required the development of specific detectors and started being observed in the early 20th century. Gravitational waves differ greatly from these as they are deformation of space and not particles. Predicted in the developments of the general relativity theory, definitive evidence of their existence was only obtained in 2015. At that time, an advanced interferometer experiment LIGO detected the gravitational wave signal produced by the merging of two black holes. After the addition of an additional interferometer Virgo that year, the LIGO/Virgo collaboration observed numerous additional mergers of black holes and neutron stars. In particular a binary neutron star merger, GW170817, was associated with an electromagnetic signal corresponding to a gamma-ray burst [44], a previously mysterious category of sources. While gravitational waves are a promising field of study in the future, they will not be addressed further in this document.

2.1.1 Cosmic rays

The term of cosmic rays is generally used to define the totality of ambient particles in space. This includes electrons and heavier leptons, protons, neutrons and nuclei. While neutrinos and photons are technically included in this definition, they behave very differently compared to the previously cited particles and represent a way smaller number. Indeed, below individual particle energies of 3.10^{15} eV charged particles are five thousand times more numerous than photons and neutrinos. Here, the term of cosmic rays will in consequence be used to describe charged particles and will in particular exclude photons and neutrinos.

The shape of the cosmic ray spectrum is impressively simple considering that it covers twelve order of magnitude in energies. The lowest observed energies start at hundreds of MeV while the highest energies observed are close to the ZeV. The all-particle cosmic ray spectrum is shown on Figure 2.1 left, it can be divided as follows [45]:

- Up to a few tens of GeV, cosmic rays are influenced by the sun activity. In particular, these cosmic rays are pushed away by the solar wind when they are diffusing in the heliosphere, thus reducing their energy and increasing the chance of escape from the heliosphere. The flux of cosmic rays at these energies is hence reduced compared to the power law behaviour found at higher energy. Furthermore, the flux in this energy band will vary following the solar activity cycle [46].

- Below the "Knee" at 3.10^{15} eV the cosmic rays energy distribution $\frac{dN}{dE}$ follows a single power law of the energy with index -2.7.
- Between the "Knee" and a "second knee" at 4.10^{17} eV the power law index changes to -3.0.
- Above the "second knee" and up the the "Ankle" at 4.10^{18} eV the index value becomes -3.3.
- After the "Ankle", the spectrum hardens to an index of -2.6.
- Finally the cosmic ray flux is suppressed above 3.10^{19} eV where a cut-off is seen.

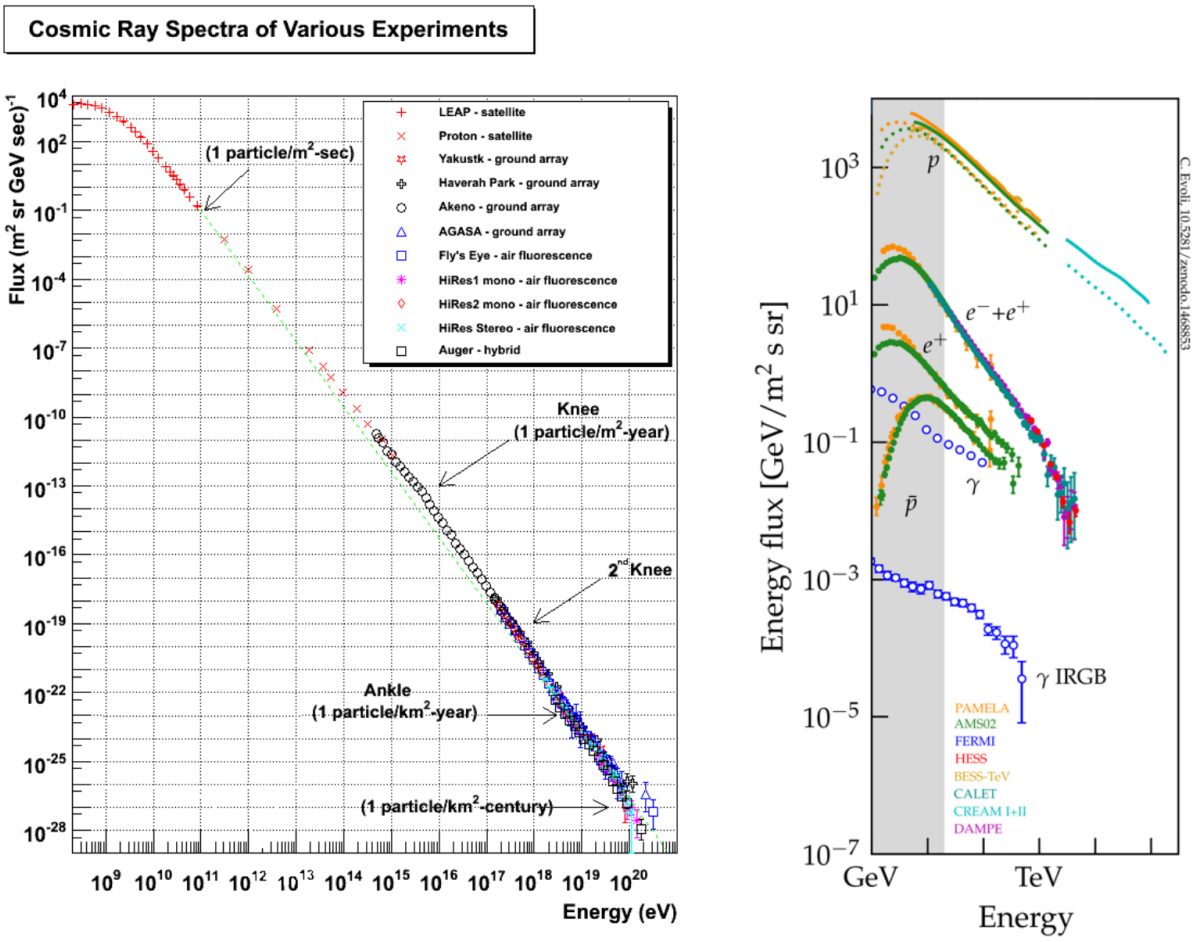

Figure 2.1: *left* - All particles cosmic ray spectrum using data from multiple experiments. Up to 10^{15} eV the flux of particles is high enough to allow for direct detection. Above this energy, indirect detection through, e.g., air showers (see section 2.2) is needed, forbidding particle identification. Adapted from [47]. *right* - Individual particle cosmic ray (and HE and VHE gamma-ray) spectrum using data from multiple direct detection experiments in the GeV to TeV range. Adapted from [48].

The composition of cosmic rays is very important in understanding their origin. Up to energies of the order of 10^{15} eV direct detection of cosmic rays is possible using satellites and balloons to avoid the atmosphere in which they would otherwise interact. This allows for identification of the detected particles as shown on Figure 2.1 right. A detailed knowledge of the cosmic ray composition is useful to identify the properties of the accelerators and to learn about the diffusion of particles in our galaxy [49]. Standard models produce the majority of the galactic cosmic rays through diffusive shock acceleration (random reflections by magnetic fields in a shock leading to a positive average acceleration of charged particles) in supernova remnants. It is hence expected that the population of protons and helium reaching us should have the same power law index for their energy distribution. Results by PAMELA [50] are incompatible with these expectations implying that either the source physics or the diffusion coefficient is misunderstood. At higher energy the flux drops below a particle per square meter per year and detectors with large effective areas are needed. Since building, e.g., a kilometre square space detector is impossible we need to use indirect detection techniques. An effective way to achieve large effective areas is to use the atmosphere as a screen for the detector. Indeed, at the energies where direct detection is not effective anymore the individual particle energy is high enough to produce extensive air showers that can be detected on the ground up to hundreds of meter from the initial particle impact point.

Ultra high energy cosmic rays (UHECR) are the highest energy cosmic rays with individual particle energy of more than 10^{18} eV. Reaching such energies is challenging and both the sources capable of emitting UHECR and the processes responsible for their acceleration are questioned to this day [51]. UHECR are characterised by two very interesting observational properties. The first one concerns the possibility to probe the particle composition of UHECR even with indirect detection. Indeed, it was shown through simulations that the energy and the depth of maximum shower development X_{max} of a cosmic ray are correlated with a dependence to its mass. Using this property it was shown that the cosmic ray composition transitions from nearly pure proton below 10^{18} eV to a majority of heavier nuclei above 10^{19} eV as seen in Figure 2.2.

The second interesting property of UHECR is their rigidity. The rigidity of a particle is $R = p/q$ with p the momentum and q the charge. The lower the rigidity of a particle the more it will be deflected by a magnetic field. Hence, while most cosmic rays are isotropised over relatively small distances, UHECR rigidities are high enough to allow the search for anisotropies. For example, for $R > 20.10^{18}$ V, deflections of less than 10 degrees over 100 Mpc are expected [51].

UHECR physics is still a young and active field of research yielding new, regularly improved observations. The UHECR spectrum was measured by Auger and telescope array but tensions are found above $10^{19.5}$ eV even accounting for systematics implying that either the detectors are misunderstood or an intrinsic physical effect is at work. The previously discussed results on the mass composition are also predicted to be refined in the future with the improvement of hadronic shower models and studies including various masses of nuclei. Another promising study is the search for anisotropies which currently only yields the observation of a global dipole anisotropy in the UHECR distribution [52] but no clear evidence of localised excesses. Not detected yet, a faint flux of neutral secondaries is predicted due to the interactions of propagating UHECR. Often called cosmogenic neutrinos and photons, these particle distributions vary strongly with the Universe content and evolution.

2.1.2 Neutrinos

Neutrinos are light neutral leptons and as a result they interact only by the weak interaction and with a very limited gravitational pull. The mass of neutrinos could not be measured yet and

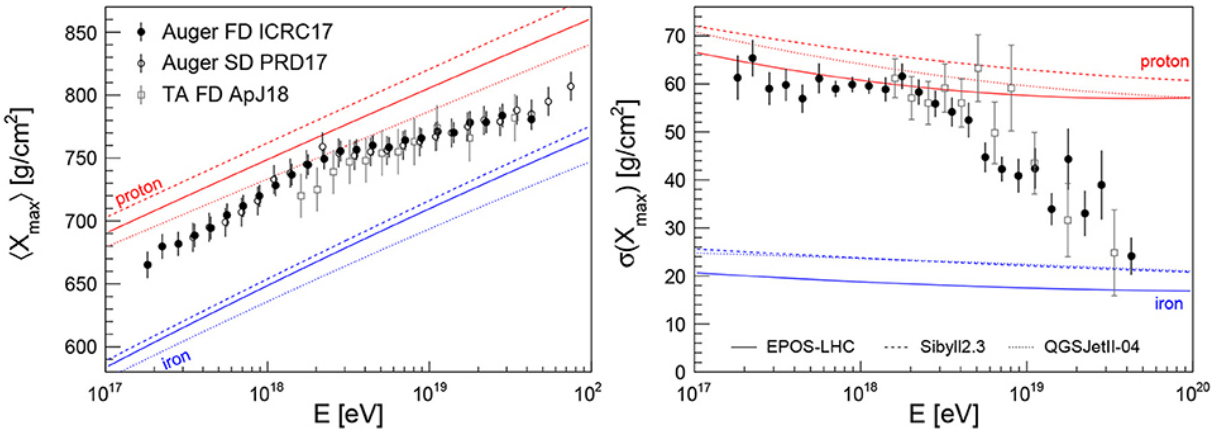

Figure 2.2: Measured mean depth of the shower maximum (left) and standard deviation of the depth of the shower maximum distribution (right) as functions of the cosmic ray measured energy. The expected values obtained from simulations are also displayed for the pure proton case (red) and the pure iron case (blue). From [51].

is so small that it was long considered to be null. Recent modelling and observations allowed to derive an upper limit on the sum of the masses of the three mass neutrinos [53] and to measure the difference between the squared masses of the mass neutrinos [54]. This gives the following constraint:

$$1.0.10^{-37}\ \text{kg} < \sum_{i=1,2,3} m_{\nu_i} < 4.6.10^{-37}\ \text{kg} \tag{2.1}$$

Here I introduced the term of mass neutrino (with subscript 1, 2 or 3) which is different from the weak interaction states related to the electron, muon and tau leptons (with subscript e, μ or τ) and called flavors. In the following I will write "neutrino" to describe the weak interaction states - ν_e, ν_μ *and* ν_τ - and "mass neutrino" if specifically speaking about the mass states. A mass state of a particle is stable when propagating in space time while an interaction state is the state concerned by the interaction. Usually the interaction and mass states of a particle are the same, e.g., an electron remains the same whether speaking about how it propagates, its weak interaction or its electro-magnetic interaction. Neutrinos are different and each one is a combination of the mass neutrinos with different weights (the reverse is naturally also true). A crucial consequence of these hybrid mass states is neutrino oscillations. Using quantum field theory it can be shown that, while pure mass states are stable, combinations of multiple mass states will evolve periodically when propagating [55][56]. Hence a neutrino produced with a given flavor (e.g. electronic ν_e) could be later detected as any of the 3 flavors with probabilities depending on the time elapsed in the neutrino rest frame.

Due to the weak nature of neutrino interaction, they are very difficult to detect. Massive detectors are needed such as IceCube, a 1 km^3 volume of ice with more than 5000 Cherenkov detectors [57]. And even with such massive detectors, only individual events can be observed as the detection rate is too low for instantaneous flux measurement. Indeed, IceCube detected only 102 high energy through-going track neutrino events (category of events with good direction reconstruction and low atmospheric contamination) over 7.5 years in the northern sky [58].

The state of the art for astrophysical neutrino measurement, currently carried by IceCube, can be divided into two main categories : study of the full sky neutrino properties and search for excesses from individual sources. A significant excess in the integrated flux of observed neutrinos allowed to extract the diffuse neutrino spectral energy distribution which could be

characterised by a spectral index varying with energy [58]. When searching for individual sources of neutrinos in IceCube data two approaches are possible. The first is the search for a significant deviation from the average in the neutrino data. One such study [59] performed a search for a spatial accumulation of muon-neutrino events with and without an a-priori catalogue of source candidates from gamma-ray observations, both with negative outcomes. The other possibility is to search for spatial and temporal coincidence between a neutrino observation and activity seen with photon observations. Such an association was possible at the 3 σ confidence level between an IceCube neutrino and an AGN called TXS 0506+056 in 2017 (more about this observation, along with an associated source modelling in chapter 6).

2.1.3 Gamma-rays

2.1.3.1 Observation

Photon based astronomy probes a wide variety of physics covering most if not all of the energy scales available in the Universe. When speaking about gamma-rays, we are interested in the most energetic photons at high and very high energy (HE and VHE). Due to the opacity of the atmosphere (Figure 2.3) it is impossible to directly observe gamma-rays on the ground. Two methods are used to circumvent this issue : direct detection from space and indirect detection on the ground.

Direct detection from space requires sending a satellite equipped to absorb the totality of the photon energy and reconstruct its direction of arrival. Satellites are strongly limited in weight and size by the rocket used to launch them. Consequently, the detection area of direct space detector is limited to the m^2 scale which is enough for HE gamma-rays but too small for VHE gamma-ray detection due to the weak fluxes at these energies. The current generation of space based HE gamma-ray detectors, such as the LAT on the *Fermi* satellite, is characterized by a wide field of view and constant activity allowing for regular, whole sky observations. The full sky map cumulating 9 years of HE observations by *Fermi*-LAT is shown in Figure 2.4 where a multitude of long lived sources are visible. The LAT is also sensitive enough to detect transient activity including purely transient sources such as GRB with 186 detections of the later over 10 years of observation [60].

Indirect detection from the ground takes advantage of the extensive air showers (EAS, see section 2.2) developing in the atmosphere when an energetic particle interacts with it. Detectors on the ground sample the Cherenkov photons and/or secondary particles from the EAS. The air shower from HE photons are too small and weak to be detected so this method is only useful for VHE astronomy. The use of the Cherenkov light produced in the atmosphere is limited in terms of field of view and activity time (more in section 2.3) whereas particle detectors have a large field of view and perfect time coverage but suffer from large direction errors and are only sensitive to the high end of the photon energy distribution.

2.1.3.2 Propagation

Photons are the neutral and massless bosons carrying the electromagnetic interaction. As a consequence, they are not deflected by magnetic fields, travel at the speed of light and interact through electromagnetic interaction only. Photons can interact quite efficiently with charged matter and between themselves. They can hence be absorbed in the source where both the matter and photon density can be important, in clouds along their propagation trajectory and by the diffuse photon fields in the Universe. Interactions in non relativistic matter are :

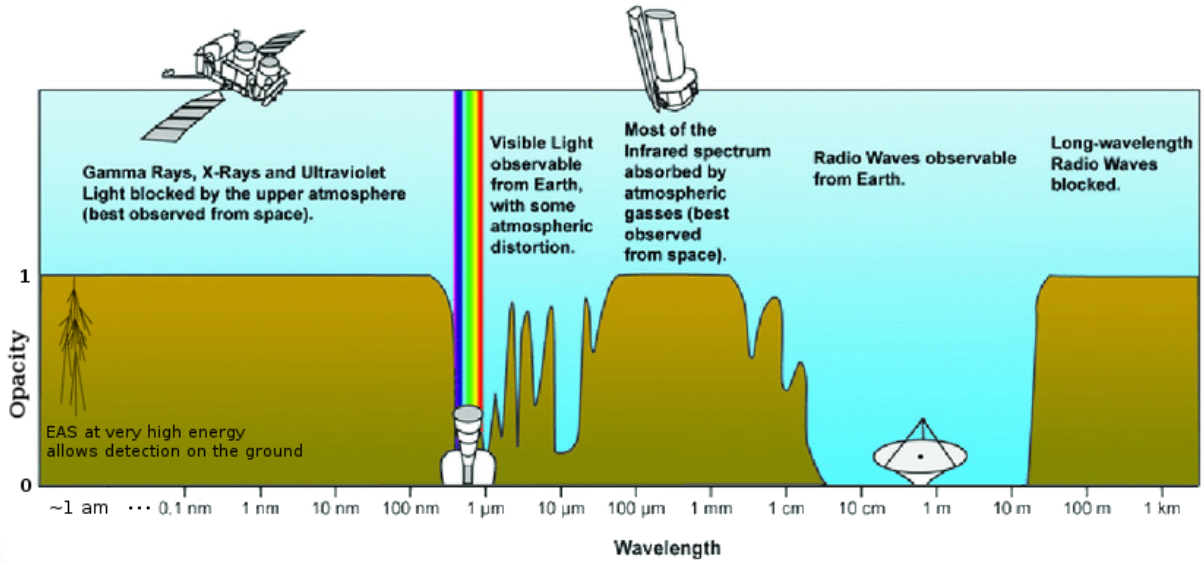

Figure 2.3: Atmosphere opacity dependence to photon wavelength. Only wavelengths for which opacity is smaller than 1 can be observed directly from the ground. The alternative for absorbed wavelength is usually space based telescopes. Very high energy photons are an exception here as they are fully absorbed but the effect on the atmosphere is still visible from the ground thanks to the produced extensive air showers.

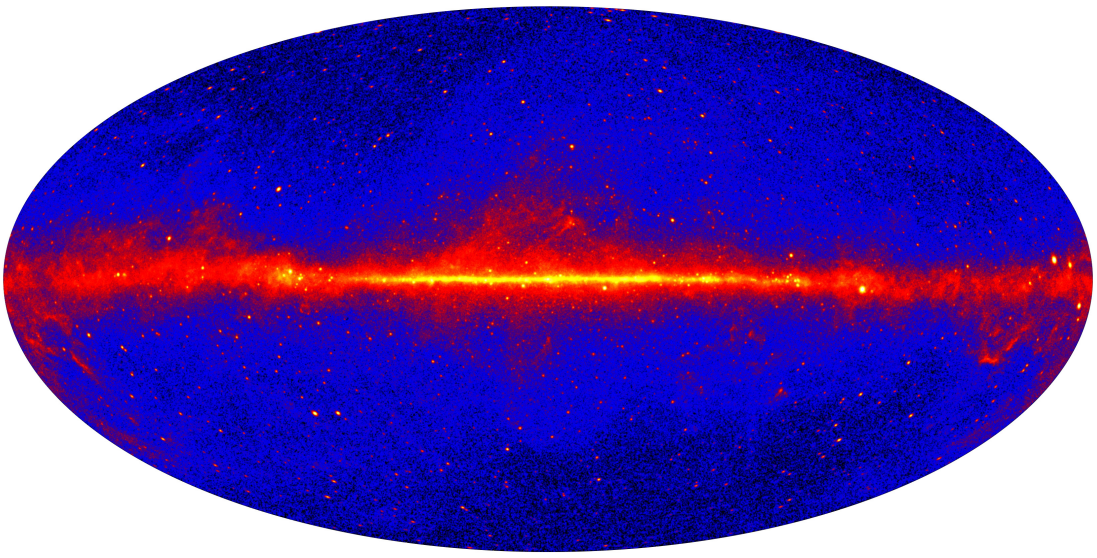

Figure 2.4: Map of the signal accumulated by the *Fermi*-LAT over 9 years of observation at high energy. Intense diffuse emission is seen from the galactic plane along with multiple point-like sources both galactic and extragalactic. Credit: NASA/DOE/Fermi LAT Collaboration

- photoelectric effect : absorption of the photon by an electron in an atom, the electron is then freed from the atom and carries the majority of the photon energy

- Compton scattering : an elastic collision of the photon with a charge particle leading to a deflection and change of energy

- pair production : A photon with energy of at least $2m_ec^2$ can convert to an electron/positron pair when travelling close to a nucleus

Each interaction in this list is dominant at higher energy than the previous one with a dependency on the absorbing medium as shown in Figure 2.5.

The extragalactic background light (EBL) is the cumulated emission of stars and dusts emitted during the Universe evolution [62]. The EBL radiation is composed of photons with wavelength ranging from 0.1μm to 1000μm. Since the Universe is mostly homogeneous the EBL is also quite uniform in space. Conversely, EBL evolves with time as the already present part is redshifted by the expansion of the Universe and additional light is emitted by the existing galaxies at any time. The energies of the EBL photons are exactly in the range at which pair production with VHE gamma-rays is efficient. This will lead to an energy dependent attenuation of the flux observed in the form of en exponential cut-off between high and very high energy. Since the EBL is present everywhere the total opacity affecting the photons coming from a given source will also depend on the distance they need to travel to reach the observer.

2.2 Extensive air showers

Highly energetic particles tend to interact inelastically. A high energy particle entering a medium is consequently likely to split into secondary particles each carrying a fraction of the initial particle energy while potentially converting part of this energy into mass. If the medium is dense enough and the energies of the secondary particles are still important they are likely to repeat this process creating once again new particles. The repetition of this process in the Earth atmosphere started by gamma-rays and other high energy particles creates millions of particles. Due to the conservation of momentum, each interaction has its product moving away from one another. As a consequence the particles will cover a transverse area increasing with each interaction. This expending blob of millions[1] of particles falling from the sky is what is called an extensive air shower. EAS can be separated into two categories : electromagnetic and hadronic.

2.2.1 Electromagnetic showers

Electromagnetic air showers are started either by a charged lepton or a photon. The likelihood of the interaction producing something else than new photons, electrons and positrons is so low in the energy range we are interested in, that it can be considered to be zero in application. Hence, the shower will only develop through electromagnetic interactions. The shower will evolve using two mechanisms :

[1] Taking as an example a 1 TeV photon, the number of electrons at rest needed to have the same mass energy is $\sim 10^{12}/5.10^5 = 2.10^6$

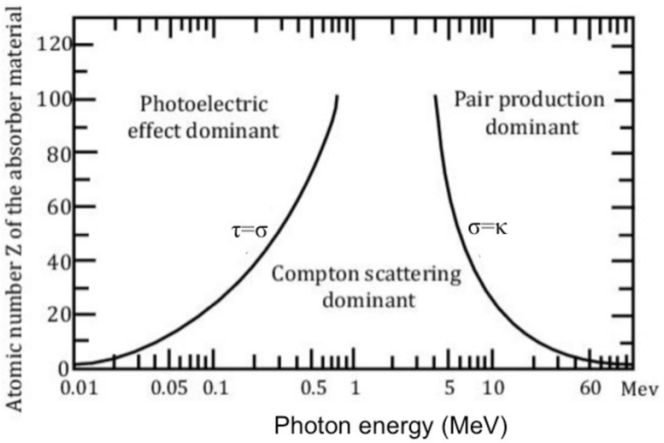

Figure 2.5: Domain of dominance of the photoelectric effect, Compton scattering and pair production process for a photon in matter. The dominance is a function of the energy of the photon and of the atomic number of the matter component. The equality lines are given between the cross sections of the photoelectric effect τ, the Compton effect σ and the pair production κ. From [61].

- pair production : A gamma-ray photon γ converts to a pair of electron e^- and positron e^+ when interacting with a virtual photon γ_v from the medium charged particles.

$$\gamma + \gamma_v \rightarrow e^- + e^+ \tag{2.2}$$

- bremsstrahlung : an electron or positron is deflected in the medium and emit a photon.

$$e^\pm + \gamma_v \rightarrow e^\pm + \gamma \tag{2.3}$$

The shower development will end when the photons energy drops below 83 MeV at which point energy loss by ionisation of the atoms in the atmosphere is the dominant channel of energy dissipation. The development of electromagnetic showers is symmetric around the initial particle momentum axis taking a conical shape.

2.2.2 Hadronic showers

Hadronic showers are started by protons or heavier nuclei. The early stages of the shower development will hence be mostly hadronic with the splitting of the nucleus and an important production of pions [63]. The hadronic expansion continues as long as the energy of the charged pions is high enough so that they interact by collision before decaying. In parallel, the neutral pions decays into two photons starting electromagnetic showers. Finally, once the individual charged pion energy is low enough they decay into muons.

Since the early particles in the shower are heavier and more energetic than in the electromagnetic showers, and since the particle production itself is complex, it is likely that some of the particles will separate significantly from the main shower. This means that the morphology of the shower is more complex than in the electromagnetic case with multiple sub-showers (Figure 2.6).

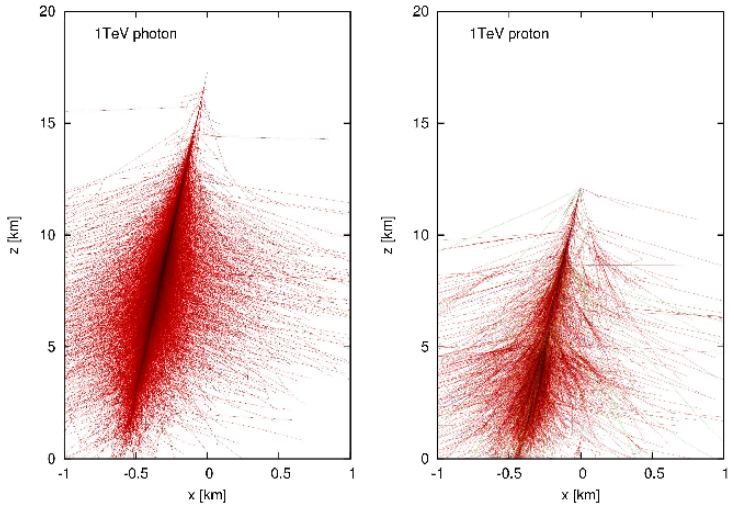

Figure 2.6: Simulated EAS from a 1 TeV photon (left) and a 1 TeV proton (right) produced with CORSIKA [64] [65]. Each line represents the path of an elementary particle created during the shower evolution. The proton first interaction occurs deeper in the atmosphere and leads to a less symetric distribution. From [66].

2.2.3 Cherenkov light

In the early stages of the EAS development particles carry enough energy to move at velocities near the speed of light in a vacuum. In particular, a large subset of particles will move with velocities $v > \frac{c}{n}$ where n is the atmosphere refraction index ≈ 1.0003[2]. Since they move faster than the speed of light in the atmosphere, a phenomenon emitting visible light called the Cherenkov effect will be initiated.

From a full theoritical development [68] it is shown that the emission fully occurs within a cone at an angle θ around the particle trajectory verifying :

$$cos\theta = \frac{1}{\beta n} \tag{2.4}$$

The emitted light spectrum, assuming a constant value of n, follows a photon density decreasing as $\frac{1}{\lambda^2}$ as shown in Figure 2.7. In a real case the refraction index is a function of λ and in particular reaches values below unity around X-rays wavelength, forbidding Cherenkov emission as the particle velocity needed would be above c. At long wavelengths self-absorption limits the Cherenkov light. With these two limits taken into account, the observed Cherenkov light is finite and peaked at the highest energies of the visible spectrum. Cherenkov astronomy is hence based on the detection of blue flashes in the sky.

2.3 H.E.S.S.: The High Energy Stereoscopic System

H.E.S.S. is an array of 5 imaging atmospheric Cherenkov telescopes (or IACTs) located in Namibia. It collects the Cherenkov light from air showers in order to observe the VHE sky. The location was chosen to optimise the quality of observations and the visibility of the Galactic plane and Galactic Center. The choice of a location in the south hemisphere was also motivated

[2] for air, at a wavelength of 589 nm, with a presure of 1 atm and a temperature of 0 Celsius [67].

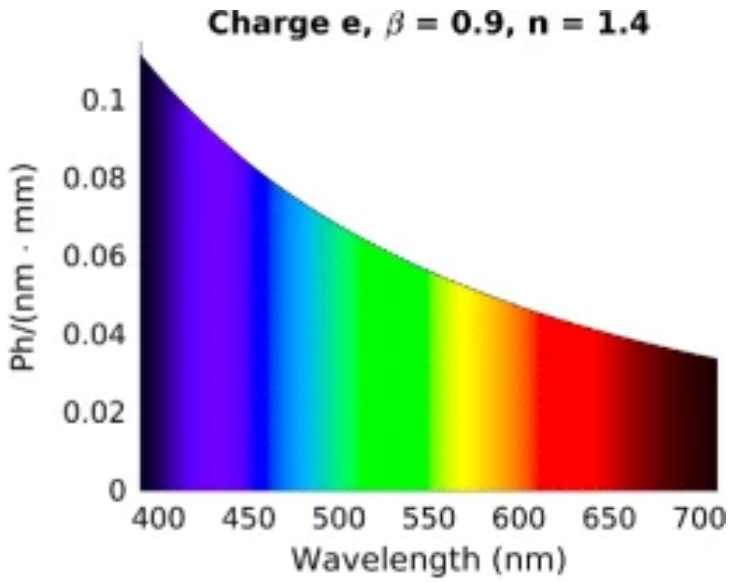

Figure 2.7: Example Cherenkov light optical spectrum assuming a constant refraction index. From [69].

by the access to an exclusive field of view in the South compared to other IACTs located in the north hemisphere such as MAGIC and VERITAS. At an altitude of ~ 1800 m above sea level, the telescopes are low enough to have the full shower development above the telescope altitude and high enough to limit the subsequent absorption of the emitted Cherenkov light. Due to the signal to observe being faint blue light, limited light pollution and atmospheric optical opacity are required. Hence, the selected site was in a desert climate for limited cloud coverage, and far away from cities to limit both light and atmospheric pollutions.

2.3.1 Technical properties

Four of the HESS telescopes, called CT1-2-3-4, were installed during the HESS1 phase of the experiment, starting in 2003. The HESS1 telescopes are positioned at the corners of a square with 120 meter sides. This configuration was chosen accounting for the requirement for the stereoscopic reconstruction of events. The stereoscopic technique requires multiple telescopes observing the Cherenkov light from the shower from as different angles as possible to obtain a precise determination of the primary initial direction and properties. Since the typical area covered by the Cherenkov light pool is a disk of radius 250 meters, a separation of 120 meters is a good compromise as larger distances would reduce significantly the fraction of detected events while a reduced viewing angle would negate the interest of using multiple telescopes.

The HESS2 phase, started in 2012, added the telescope CT5 in the middle of the array (Figure 2.8). The goal was to improve the collection area and to extend the energy range of the experiment thanks to a larger mirror. The camera from the HESS1 telescopes were also upgraded in 2016 [70] improving in particular the timing properties of the electronics in two ways. First a huge reduction of the camera dead time by a factor 60. Second a possibility to sample the full evolution of the charge in a pixel instead of the integrated charge when saving an event. On one hand the first improvement led to a direct improvement in the ability of the CT1-4 telescopes to trigger stereoscopically with CT5. On the other hand the sampling

possibility may lead to improvement at the highest energy in the future at the cost of increased data size.

All 5 telescopes are composed of a mount controlling the pointing direction, a mirror collecting the atmospheric Cherenkov light and a camera receiving the signal. The mount is an alt-azimuthal steel mount (Figure 2.9-a) allowing a pointing of the telescope at any point in the sky. The mirrors of the HESS1 telescopes are segmented into 382 round, 60 cm diameter, mirrors forming a combined mirror with a diameter of 12 m and a surface of 108 m^2 (Figure 2.9-b). In the case of CT5, the 614 m^2 total area of the mirror is divided into 875 hexagonal mirrors and is equivalent to a 28 meter diameter mirror (Figure 2.9-c). The hexagonal shape was chosen to optimise light collection by limiting gaps between the mirrors.

Each pixel in the H.E.S.S. cameras (Figure 2.9-d) is a photo-multiplier tube (PMT) tasked with converting the blue photons into electronic signal. The entrance of the pixels are equipped with Winston cones : mirrors with hexagonal entrances redirecting the light that would fall between pixels into the PMTs. The hexagonal shape allows for nearly 100% of the light sent to the camera to be processed by the PMTs. Behind the PMTs, the electronics for image digitization, readout and triggering is integrated. The HESS1 cameras are composed of 960 pixels while the HESS2 camera contains 2048. For both cameras the pixels are gathered into movable sections called drawers (Figure 2.9-e). Each drawer carries 16 pixels[3] and part of the electronics, and is used in the triggering process. Most of the HESS1 cameras was replaced during the upgrade of the electronics and some of the surrounding hardware in 2016. The goal was to replace the ageing hardware while improving the readout electronics, reducing the dead time and also testing technology for future CTA telescopes.

In a drawer, the signal coming out of each PMT is split into 3 channels. The trigger channel is connected to the trigger control system which will be responsible to control the data recording. The other two channels are a low and a high gain channel which are both connected to an analogue card tasked with temporarily saving the signal. When a trigger decision is received, the memories are read and the signal is converted and sent to the camera CPU through a box bus. The drawer contains 2 analogue cards each responsible for 8 pixels. An additional slow control card takes care of various tasks including voltage and temperature control and communication with the box bus.

	H.E.S.S. experiment		
duty cycle	10 %		
coordinates	Khomas Highland,Namibia 23.3S 16.5E		
altitude	1800 m		
	HESS1	**HESS1U**	**HESS2**
pixels	960		2048
field of view	5°		3.2°
dead time	450 μs	7.2 μs	< 25 μs
energy threshold	∼100 GeV	∼100 GeV	∼30 GeV

Table 2.1: Summary of some H.E.S.S. properties

2.3.2 Data acquisition

A typical observation night by H.E.S.S. is divided in observation runs. When a run starts all 5 telescopes point toward the selected source position, or more often at a small "wobble"

[3]HESS1 camera : 60 drawers; HESS2 camera : 128 drawers

Figure 2.8: The five H.E.S.S. telescopes in Namibia. CT5, the bigger telescope added in 2012, is visible at the center of the photograph, and is surrounded by the CT1 to 4 telescopes. Credit: H.E.S.S. Collaboration, Arnim Balzer

angle ($< 1°$) from it (see subsubsection 2.3.3.3). The signal received is then recorded following a trigger strategy (defined below) during 28 minutes before ending the run. The next pointing is then acquired from the scheduler and a new run started.

In order to record an event, a multi level trigger is applied. In the camera at least 3 pixels from 4 adjacent drawers need to receive at least X[4] photo-electrons each in a time window of $\sim 1.3ns$. This duration is necessary to account for the difference of distance travelled and emission time of associated photons. When the criteria is meet the information is sent to a central trigger system with three possible outcomes :

- At least two telescopes reached their individual trigger in a time window of 80 ns : the event is recorded in stereo mode
- CT5 only was triggered : the event is recorded in mono mode
- Only one HESS1 telescope was triggered : the event is discarded

A duration of 80 ns is equivalent to a distance travelled by light of 400 meters which is needed due to the telescope separation and potential electronic delays. With a trigger rate of ~ 500 Hz the average duration between two event is 2 ms $= 25000 \times 80$ ns so the probability of recording coincident noise events with multiple telescopes is low.

The stereo mode is preferred when possible as it increases the statistics received from the shower and allows to observe the shower from multiple angles leading to a more precise estimation of the initial particle properties. It also has the advantage of reducing the quantity of data to be saved by rejecting the night sky background (NSB) which is expected to yield random signals in each telescopes independently. The mono mode is thus used to exploit specific advantages of CT5. Namely the lower energy threshold and, in case of prompt transient triggers, the shorter slewing time.

[4]Camera dependent. For example X=4 in the case of the original HESS1 cameras

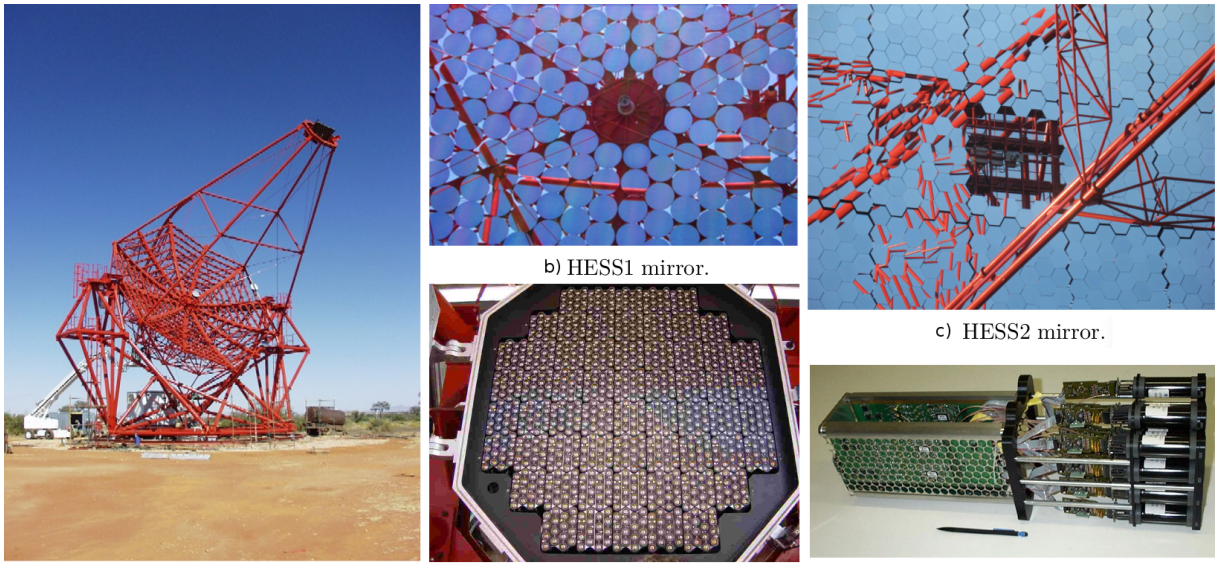

a) HESS1 steel mount. b) HESS1 mirror. c) HESS2 mirror. d) HESS1 camera. e) HESS drawer.

Figure 2.9: Various components of the H.E.S.S. telescopes. Credit: H.E.S.S. Collaboration

Before analysing the obtained data, a calibration is required to take into account the status of the atmosphere and the instrument. At the level of the cameras, specific runs are performed to evaluate the level of each pixel pedestal, the average response of the each pixel to a single photo electron as well as the inhomogeneities in the response of the camera exposed to a uniform signal. The structural deformation of the telescopes are corrected using data obtained during pointing runs : observations of stars with known positions using a CCD located on the cameras. It is assumed that deformations of the mount and positioning errors are only dependent on the pointing direction. Consequently a model of pointing correction for all observations is derived from the pointing run and updated monthly. Finally, the optical transmittance of the Cherenkov light in the atmosphere and the telescope optics needs to be evaluated. This is done by comparing the muon rings in the data with the expected light as the muon Cherenkov emission is very simple[5].

2.3.3 Analysis

In the H.E.S.S. experiment the calibration, reconstruction and analysis are performed by two independent software chains in order to provide a cross-check of every published analysis. Thanks to this procedure bugs can be identified and corrected. Most of the techniques described in this part are used in both analysis chains, called Paris Analysis and HAP, with the notable exception of the gamma reconstruction techniques.

2.3.3.1 Gamma/hadron discrimination

As seen previously, the information acquired by IACTs is a sampling of indirect Cherenkov light from VHE photons and hadrons. From camera images the discrimination between photons and hadrons is performed taking advantage of the difference in morphology of electromagnetic

[5]supraluminal muons will quickly lose energy through Cherenkov emissions. Thus the conic Cherenkov emission occurs in a very short time leading to a thin ellipse on the ground

and hadronic EAS, and the photon origin and energy are extracted. One of the simplest way to do so is by using the Hillas technique [71]. An ellipse is fitted on the shower image after cleaning of the pixel containing only night sky background and the result of the fit is compared to simulations to determine both the nature of the particle and, if it is a photon, the primary energy and direction. Nowadays new and more effective reconstructions exist and the Hillas reconstruction is rarely used.

Model

Used for the Paris Analysis analysis software, the Model reconstruction [72] compares the raw camera image with simulated showers from a semi-analytical model. The model simulates images of the shower in the camera through the following steps :

- Monte Carlo production of the particles in the shower
- Integration of all the Cherenkov light produced in the shower and seen in the camera, taking into account the telescope response (reflectivity, quantum efficiency,...) and atmospheric absorption
- Modelling of the NSB

Images are produced over the useful range of 4 parameters : energy, impact distance, primary interaction depth and zenith angle. Effects of the shower direction and azimuthal angle do not need to be saved as they can be obtained by rotation and translation of the image in the camera and are the last 2 parameters describing the shower.

For any set of values for the 6 parameters the associated predicted image in the camera can be obtained by interpolation between the saved images and applying the required spatial transformations. Comparing with real camera images, the telescope log-likelihood is obtained as the sum of the individual pixel log-likelihood : the probabilities of observing the signal seen in the pixel if it follows a Poisson law convoluted by the PMT resolution, with the modelled signal as mean value. In order to estimate the real shower parameters a Levenberg-Marquardt fit algorithm [73] is applied to minimise the telescope log-likelihood. The best estimation of the shower parameters and associated errors are obtained this way.

At this point it was assumed that the particle at the origin of the image in the camera is a photon. To reject a reasonable amount of protons while keeping the majority of photons, cuts on discriminant variables are applied. One such variable is the mean scaled shower goodness (MSSG) which measures the difference between the best guess model image and the actual image accounting only for the shower and ignoring the remaining part of the camera. After selection of the shower pixels, the shower goodness is computed as :

$$SG = \frac{\sum_{pixel\ i}[logL(signal\ in\ pixel) - average\ logL\ at\ the\ modeled\ mean]}{2\sqrt{number\ of\ degrees\ of\ freedom}} \tag{2.5}$$

This value is then corrected for the effect of the finite size of the cameras which can bias the goodness of high energy, large impact showers. The MSSG is hence obtained by scaling the SG using tabulated values of its mean for a given energy and impact. MSSG distributions of photons and protons are shown in Figure 2.10 assuming that all OFF events are protons. More details on applied cuts are given in subsubsection 2.3.3.2.

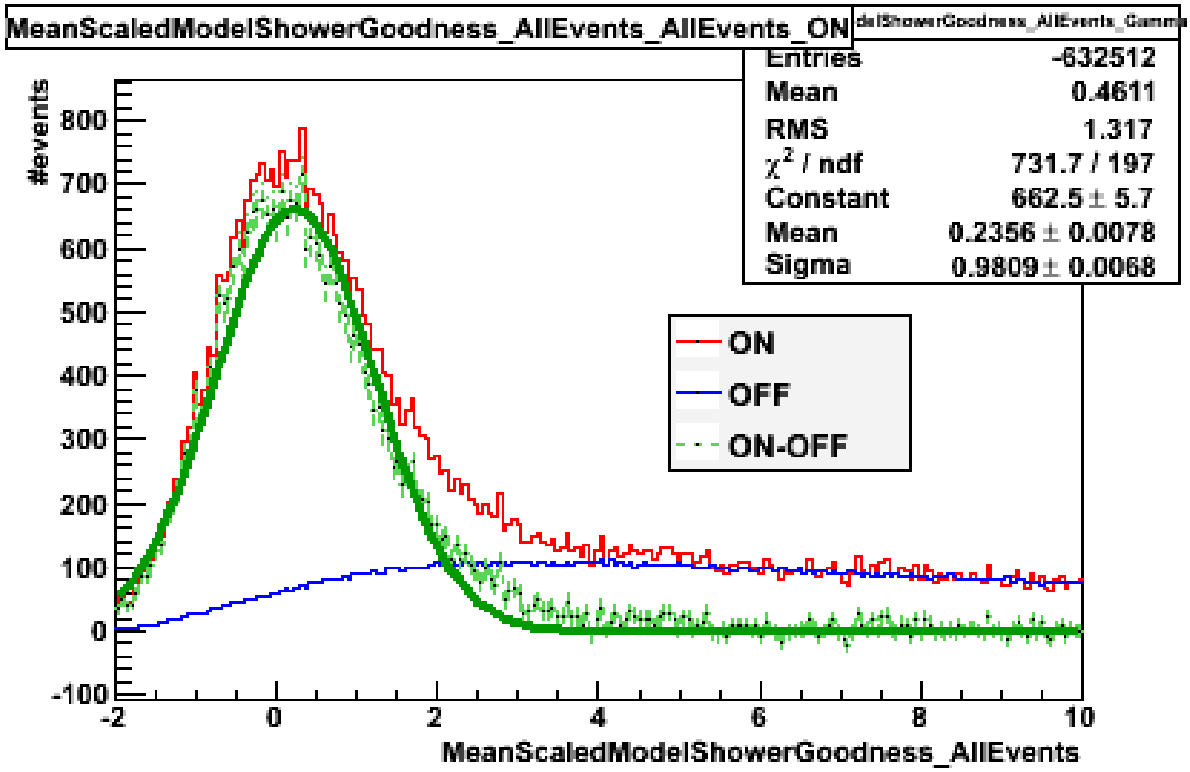

Figure 2.10: MSSG distributions of events for real data taken on the Crab Nebula. The MSSG distribution for protons is estimated using the OFF dataset. The ON-OFF distribution shows the photons MSSG.

ImPACT

The ImPACT (Image Pixel-wise fit for Atmospheric Cherenkov Telescopes) framework [74] used in the HAP analysis chain uses a method similar to Model in order to recover the photon parameters but with a few key differences. First, ImPACT doesn't use a semi-analytical model for the shower simulation but a full Monte-Carlo production of the air showers followed by ray tracing and simulation of the telescope electronics. The use of full simulation allows to directly include fine effects such as the Earth magnetic field or biases in the electronics. This comes at the cost of heavy computational power requirement. The second point of divergence with the Model method is on the fitted part of the images when evaluating real data. Contrary to the Model approach, only the pixels containing the shower signal are used in the log-likelihood minimisation. The final difference concerns the gamma-hadron separation. Since ImPACT mostly discards the background in its template the effect of the NSB is less precisely estimated compared to Model which can particularly affect analysis where the field of view is inhomogeneous. This is also important on variable such as the MSSG, thus another method is used for gamma-hadron discrimination. After the derivation of the shower parameters in the photon hypothesis, a boosted decision tree is used. It takes a series of discriminant parameters to determine the nature of the reconstructed event. The boosted decision tree training was performed using

gamma simulations to obtain the distribution of the discriminant parameters for gamma-rays, and observations of empty field of view for the hadronic distributions.

2.3.3.2 Analysis profiles

The Paris Analysis software allows for a wide variety of analysis profiles characterised by a reconstruction technique : Model or Hillas; the telescopes used for the reconstruction : CT1-4 stereo, CT1-5 stereo or CT5 mono; and cuts applied to select events. Below, I will describe the different profiles for the Model reconstruction. Profiles for the Hillas reconstruction are similar but exclude combined profile and some cut configurations.

Telescope configuration

Since the addition of CT5 during the HESS2 phase of the experiment, the inhomogeneity of the array multiplied the possible telescope configurations usable to reconstruct events. Three telescope configurations as well as three combinations are available :

- **HESS1 Stereo** : Events are reconstructed in stereoscopic mode using only the information from the CT1-4 telescopes. This configuration is used when CT5 is not available or usable. It is characterised by a higher energy threshold compared to profiles including CT5.

- **HESS2 Stereo** : Events are reconstructed in stereoscopic mode using the information from all CT1-5 telescopes. The reconstruction needs to account for the array inhomogeneity. Due to the difference in sensitivity between CT5 and the smaller telescopes, lower energy events are more likely to not be detected by some of the small telescopes while higher energy events tend to lack informations from CT5.

- **HESS2 Mono** : Events are reconstructed in monoscopic mode using only the information from the CT5 telescope. The large mirror of CT5 allows the lowest energy threshold for this configuration. This configuration is used when we are particularly interested in low energy emissions.

- **HESS2 Combined** : These profiles use events which can be reconstructed by both HESS2 Stereo and HESS2 Mono configurations. The more precise stereoscopic reconstruction is thus used over a large energy range, and the lower energy threshold available with CT5 is exploited.

- **HESS Combined** : These profiles use events which can be reconstructed by both HESS1 Stereo and HESS2 Stereo configurations. It is thus fully stereoscopic and allows to combined data with and without CT5.

- **HESS Combined3** : These profiles use events which can be reconstructed by all three telescope configurations : HESS1 Stereo, HESS2 Stereo and HESS2 Mono. For each event, all available reconstructions are compared and the one with the smallest errors is selected. It allows to combine dataset with different telescopes available and to optimise the quality of reconstructed events.

Selection cuts

In order to select events for the analysis a set of cuts are applied. First, the raw properties of the image in the camera are used. This includes a cut on the minimum charge received in the camera in number of photo-electrons, a minimum number of pixels above a threshold charge and a maximum distance between the shower and the camera center. This allows to exclude too faint, too small, and too badly contained showers which would be wrongly reconstructed or not originate from astrophysical photons. Then, a variety of cuts are applied on discriminating variables produced during the Model reconstruction. Cuts are applied on the primary depth of interaction, the error on the direction of the reconstructed event, the quality of the NSB reconstruction (through an estimator called NSB goodness), and the MSSG. Finally, a cut is applied to selected gamma-ray candidates on the distance between the source position and the direction of arrival of the event.

When applying a cut, a choice needs to be made between purity and efficiency of the selection. Taking as an example the MSSG as shown in Figure 2.10, we see that photons are found with MSSG as high as 4. In order to keep all the signal, this would thus be the cut value. The drawback would be that a large contribution from hadrons would also be accepted as they dominate in the MSSG range from 2 to 4. In order to keep a majority of photon events while optimising the signal over noise ratio, a maximum value of $\sim$1 for the MSSG could be used. A selection of background events can also be performed by applying a lower limit cut of, e.g., $\sim$2. Events with MSSG between these two cuts are too difficult to identify and are thus generally not used.

There is a total of 5 sets of cuts for each telescope configuration optimised for different science cases :

- Std or Standard : These cuts, optimised using observations of the Crab Nebula, are thus particularly adapted to analyse observations for sources with a relatively hard spectrum and high flux.

- Loose and Very Loose : These two sets of cuts are less constraining than the Standard cuts and increase the number of events accepted at low energy. They are best used for sources with softer spectrum but are more sensitive to region of the sky with high NSB such as the galactic plane.

- Safe : More restricting than the standard cuts, the Safe cuts are useful to limit contamination in region of the sky with high NSB.

- Faint : The most restricting cut configuration, it rejects most of the background at the cost of a higher energy threshold. It is thus optimised for observations of faint sources with a hard spectrum.

Additional cuts can also be added if required for a given analysis. The cut uniformity was recently improved so that the cuts applied in Combined profiles are the same as the cuts applied

for single telescope configuration profiles. Meaning that an event reconstructed using HESS2 Mono in the HESS Combined3 profile is subjected to the same cut as in the HESS2 Mono profile.

2.3.3.3 Signal extraction

Despite the advanced hadron rejection method used, a significant flux of hadrons passes the event selection cuts during an analysis. This is mostly unavoidable as the large number of hadrons will statistically always produce air showers with electromagnetic morphologies. This leads to a uniform background of events in the maps produced with H.E.S.S. along with a potential excess from a VHE photon source. The most used method to analyse IACTs data uses control regions to evaluate the background. Defining an ON region believed to contain the signal originating from a source along with a background contribution, the later is estimated using an OFF region (the control region) containing only background.

The excess at the source position is then defined as :

$$Excess = N_{ON} - \alpha N_{OFF} \tag{2.6}$$

Where N_{ON} and N_{OFF} are respectively the number of events from the ON and OFF regions, and alpha is the acceptance corrected ratio of size (or livetime) between the ON and OFF regions.

The significance of the excess can be determined in units of equivalent normal law standard deviation (σ) using the Li&Ma formula , equation 17 in [75] :

$$S = \sqrt{2}\left\{ N_{ON}\ ln\left[\frac{1+\alpha}{\alpha}\left(\frac{N_{ON}}{N_{ON}+N_{OFF}}\right)\right] + N_{OFF}\ ln\left[(1+\alpha)\left(\frac{N_{OFF}}{N_{ON}+N_{OFF}}\right)\right]\right\}^{0.5} \tag{2.7}$$

In H.E.S.S., the sign of the excess is also added to this significance to identify negative fluctuations and obtain a smooth behaviour.

The ON region will always be taken at the source position and its size will be at least as large as the instrument PSF (point spread function)[6], and larger for visibly extended sources. The OFF region selection is more complex. On one hand, the higher the fraction of the field of view used the more statistics will be available to precisely estimate the background. On the other hand any difference in acceptance between the ON and OFF region need to be corrected which is likely to induce errors and potential sources need to be rejected from the OFF regions.

One of the generally most effective way to select the OFF region is the reflected background technique. OFF regions are produced by rotating the ON region around the pointing position as shown in Figure 2.11. It requires the observation to be taken with on offset between the source direction and the telescope pointing which is the reason why observation runs are taken with an offset angle. Additionally, in order to obtain a symmetric coverage around the source and limit systematic errors, the direction of the offset around the source position will alternate between observation run. Thus this observation mode is called wobble observations. The OFF regions are also required to be independent and separated from the ON region and any pre-defined exclusion regions containing additional sources. The major benefice of the reflected background technique is that the telescope acceptance is radially symmetric in first approximation implying that it does not need to be known in order to determine α.

Other background estimations include the template technique [77] : fitting of a background model over the field of view; the ring background technique [76] : uses a ring around the source position as OFF region; and a variety of techniques specifically developed to, e.g., study very

[6]This will be the case for extragalactic sources which are so far that they appear point-like for H.E.S.S., meaning that their angular extension is smaller than the resolution of the telescopes.

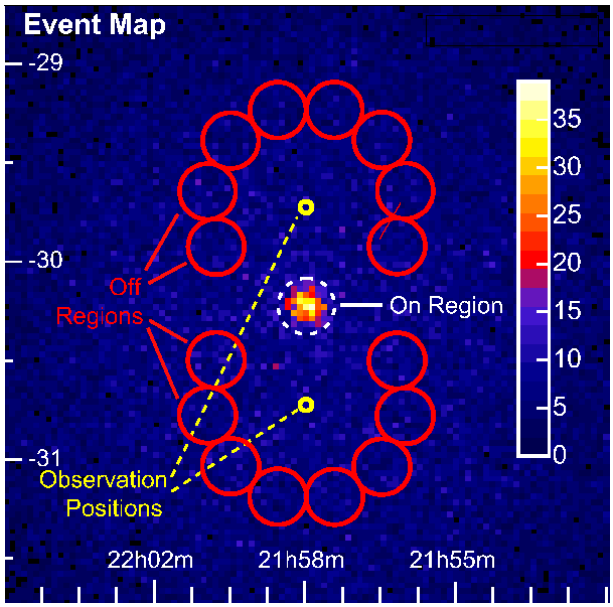

Figure 2.11: Reflected background technique applied to an observation with 2 runs. The ON region is chosen on the source which is separated from the observation position by a small intentional offset angle. For each pointing a set of independent OFF regions (8 in this case) is produced by rotation of the ON region around the pointing direction. No OFF regions are created next to the ON region to avoid gamma-ray contamination during the background estimation. From [76].

extended emissions. Since the reflected background method is not suited for use on all of the field of view, significance maps are produced using some of these alternative techniques as in Figure 2.12.

2.3.3.4 Spectral and temporal analysis

When a source is detected it is possible to extract information on the energy distribution of the photons it produces - the energy spectrum - and the time distribution of the emission - the light curve. The spectral and temporal analyses are usually performed using the reflected background extraction to reduce systematics.

Spectrum determination using the forward folding technique

In H.E.S.S. the spectral analysis is performed using the forward folding technique [78]. The basic idea is to evaluate a spectral hypothesis by comparing the photon detections it predicts with the observed signal in the ON and OFF regions using a Poisson statistics.

The log-likelihood for a given spectral shape assumption $\phi = \frac{dN}{dE_{true}}$ is obtained by summing over the bins of a 4 dimensional space in zenith angle, off-axis angle, optical efficiency and reconstructed energy. For a given bin we estimate the predicted number n_γ of photons detected by the telescopes. It requires the knowledge of the acceptance of the telescope as a function of the gamma-ray true energy $A(E_{true})$ and the resolution of the energy reconstruction $R(E_{true}, E_{rec})$.

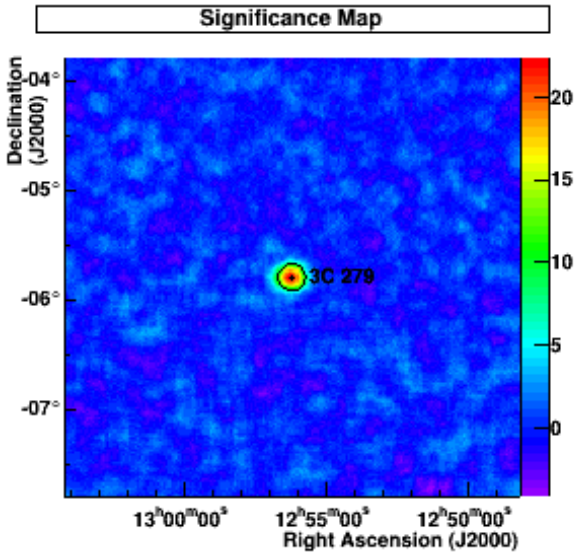

Figure 2.12: Significance map produced using the ring background method. For each location on the map, the signal is compared to the average signal estimated on a circular region around the position excluding any known source. The random nature of the fluctuations in the region without sources, and the correlations between the significance estimates induce a gaussian distribution of the significances centred on 0 when using the Li&Ma formula. Here, the source 3C 279 is clearly visible at the center of the map as a point like area with high significance, incompatible with a background fluctuation.

In Poisson statistics the probability of observing N_{ON} events from the ON data and N_{OFF} events from the OFF data while expecting n_γ photons and αn_h hadrons in the ON region is :

$$P(N_{ON}, N_{OFF}|n_\gamma, n_h) = \frac{(n_\gamma + \alpha n_h)^{N_{ON}}}{N_{ON}!} e^{-(n_\gamma + \alpha n_h))} \times \frac{n_h^{N_{OFF}}}{N_{OFF}!} e^{-n_h} \tag{2.8}$$

with α the ratio of livetime between the ON and OFF region and n_h is estimated by maximising $logP$ over n_h.

A Levenberg-Marquardt algorithm is used to maximise the full log-likelihood against the free parameters of the assumed spectral shape. For example in case of a power law spectrum :

$$\phi = \frac{dN}{dE_{true}} = N\left(\frac{E}{E_0}\right)^{\Gamma} \tag{2.9}$$

E_0 is a reference energy without physical meaning and there are two parameters : N the flux normalisation and Γ the photon index.

Light curves

Light curves in H.E.S.S. are generally produced using the average spectral shape fitted over the full dataset. In each time bin the local normalisation of the flux is re-evaluated with respect to the local values of N_{ON} and N_{OFF} using either a full Poisson treatment or simply the excess. Once this is done the light curve point is produced by integrating the renormalised spectrum over the selected energy interval. An example light curve is shown Figure 2.13. Before this

work, the binning available were bins of a lunar period, a night, an observation run or a fixed duration shorter than a run. A new time binning method is described in chapter 3 section 3.1.

2.4 CTA : The Cherenkov Telescope Array

The Cherenkov Telescope Array (CTA)[7] will be an observatory composed of two arrays of IACTs meant to succeed the current experiments H.E.S.S., MAGIC and VERITAS. CTA will be composed of two arrays located at La Palma in the northern hemisphere and in the Atacama Desert in Chile in the southern hemisphere. The choice of implementing two arrays, one in each hemisphere, is motivated by the possibility of achieving a near complete coverage on the night sky. Each site was selected after careful scientific [79] and politico-economic studies.

CTA aims at reaching sensitivities over an order of magnitude better than current instruments, with an extended energy range (see Figure 2.14), an improved angular resolution and a wide field of view [80]. To do so, the choice of implementing multiple sizes of telescopes, as done in H.E.S.S., was made. The Large Sized Telescopes (LST), with a primary mirror of 23 meter in diameter, will be the telescopes most sensitive at low energy between 20 and 150 GeV. This will allow to observe energies unavailable to current instruments using this observation technique. Since this energy range is of particular interest for transient study, an important focus was made in reducing the repositioning time of the LST down to ∼30 seconds. The Medium Sized Telescopes (MST) , with a primary mirror of 12 meter in diameter, will be the telescopes most sensitive in the core energy range of CTA between 150 GeV and 5 TeV. Thanks to a large field of view of ∼ 7.5 degrees and a high sensitivity, this will be capable of performing rapid surveys of the VHE gamma-ray sky. Finally the Small Sized Telescopes (SST) will be responsible for the coverage of the highest energies between 5 and 300 TeV. To do so, a large number of telescopes sampling a large area with small primary mirror of 4.3 meter in diameter are needed. They will also achieve a large field of view of ∼ 10.5 degrees.

The northern array will be composed of 4 LST and 15 MST while the southern array will be composed of 4 LST, 25 MST and 70 SST. SST will only be located in the south hemisphere since this site will have an easier access to galactic sources. Indeed, only galactic sources are expected to be detectable in the SST high energy range due to the absorption by the EBL. Given the

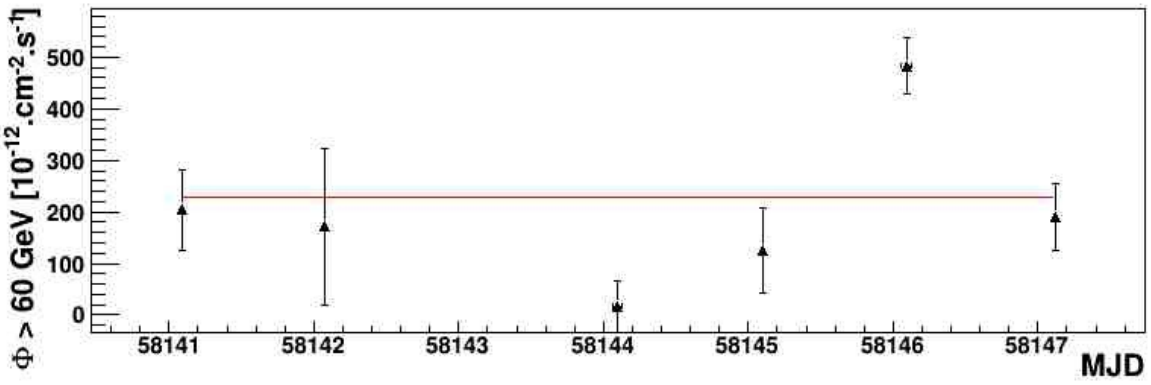

Figure 2.13: Nightly binned light curve obtained using observations of the FSRQ 3C 279 in January 2018 analysed in mono mode. Details of this analysis are given in chapter 4 section 4.3.

[7] Detailled informations about CTA can be found in the dedicated website https://www.cta-observatory.org/

high cost of an array of SST, only the site benefiting the most from a sensitivity at the highest energies will be equipped.

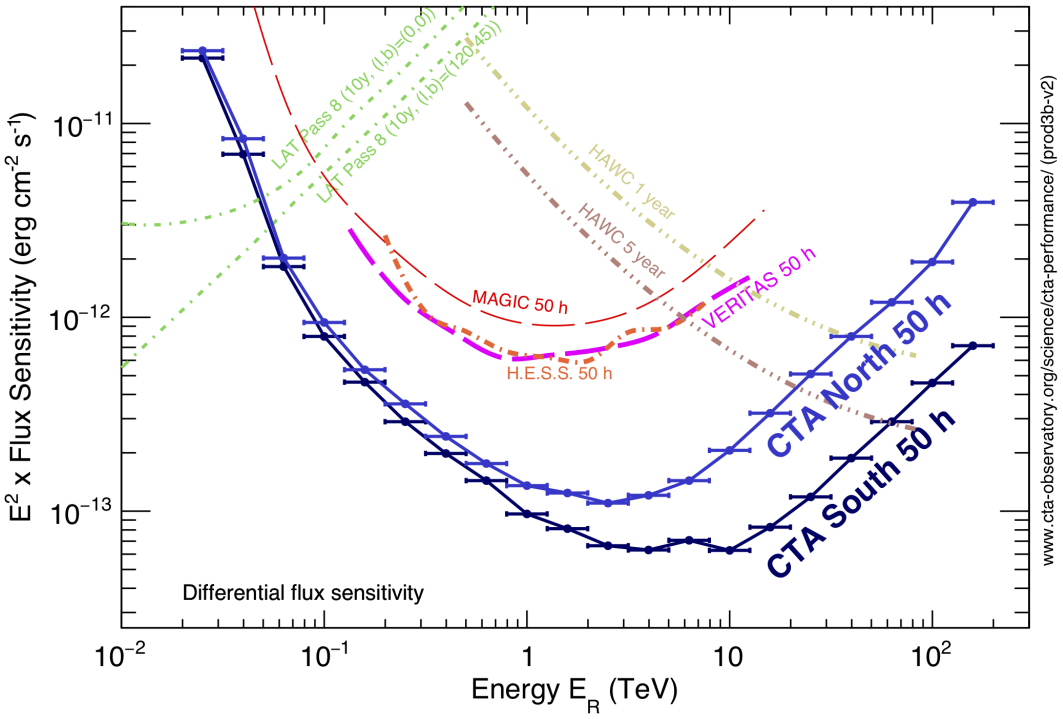

Figure 2.14: Comparison of the expected sensitivity of CTA with the sensitivity of current instruments. From https://www.cta-observatory.org/science/cta-performance/

The science to be performed using CTA has been divided into two main categories : a core program already defined by the collaboration [81] and a variety of smaller projects to be performed using open time awarded during the activity period of the observatory. The core program will use around 40% of CTA observation time over the first ten years of operations [81] and is composed of campaigns with high interest and requiring long observations and complex organisation. It is divided in "key science projects" including an AGN program; surveys of, e.g., the Galactic Center and an area of the extragalactic sky; a dark matter program; a transient program; ...

CTA builds on the knowledge acquired in the field of VHE photon observation with the current and previous generations of experiments. It is an ambitious project which will improve significantly the scientific possibilities in this domain. CTA is now in construction phase. It also performs commissioning observations with the first LST prototype in the northern site. In January 2020, it managed to detect the pulsed emission from the Crab pulsar[8]. Construction is now actively started and CTA will be of major importance in the decades to come and for at least thirty years.

[8]https://www.cta-observatory.org/lst1-detects-vhe-emission-from-crab-pulsar/

Chapter 3

Improvement to the analysis software for time dependent signal analysis

Sommaire

The dataset we are interested in are obtained from the observation of variable emissions from AGN with H.E.S.S., consequently it has some critical properties :

- irregular sampling : observations are impossible during run transitions ($\sim$ minute), observations of other sources, bad weather, bright moonlight periods, daytime and other potentially random constraints.

- non-linear statistics : the duration needed to accumulate a significant excess from the source is dependent on the instantaneous flux of the source.

- time criticality : the interesting dataset is limited in duration and a-priori unique, so any discarded data cannot be recovered with later observations.

The first point is linked to the duty cycle and field of view limitation of the experiment while the two following points are intrinsic to the science case. In order to improve the quantity of information extracted from dataset obtained on variable sources two additions to the H.E.S.S. analysis software were developed. The first is a method to dynamically adapt the duration of light curves binning to the available statistic. The second aims at recovering observation runs that would be discarded otherwise due to an identified, temporary issue.

3.1 Paris Analysis software : an overview

Paris Analysis is a C++ code built with ROOT[1] divided into modules and classes dedicated to a multitude of tasks from simulation to the various steps of an analysis. It makes use of ROOT to perform most operations and to store and display the analysis results. It is also provided with a graphical user interface (GUI) created using python. The GUI can receive inputs on the kind of analysis to be performed, with which data and with which parameters. Then, it writes a bash file containing the instructions to create and launch the desired C++ code. Finally the bash file is either run or submitted to a computing center.

The implementation of a new optional functionality requiring input hence implies the following steps :

- addition in the python GUI of buttons or input fields to activate and control the task to perform

- transfer of the information to the C++ code through the bash file

- saving of the needed values into class variables able to reach the relevant part of the analysis

- implementation of the functionality

- modification of the ROOT result file to contain the new results and information needed for a future analysis step

[1] https://root.cern.ch/

3.2 Adaptive light curve binning algorithm

3.2.1 Concept

One of the most important property to understand the variability of a source is its light curve. The light curve represents the evolution of the flux of photons emitted by the observed object as a function of time. One of the main issue when creating a light curve is determining the duration of the bins to be used as a long integration averages out any shorter variability while a very short binning can lead to light curve points produced without any discernible signal. The goal is thus to choose the shortest binning that still creates only meaningful flux estimates.

The adaptive light curve binning algorithm was developed in order to provide a binning adapted to strongly varying observation, for which the low state requires multiple minutes of integration to be evaluated whereas the high state is significant enough to be resolved potentially down to the second scale. To do so, an iterative process is applied for each points in order to find the optimal integration duration. The starting time is fixed and the number of ON and OFF events between the starting and ending time of the point is used to evaluate the significance of the source based on this time interval only. Then, if the significance is above a given threshold, the flux is computed and a light curve point created. Else, the ending time is increased and the significance is re-evaluated over the new interval.

In the end, a light curve is created where each point is exactly long enough to be significantly above the background at a selected level (see e.g. Figure 3.1).

3.2.2 Implementation

In Paris Analysis the choice was made to only create light curve points contained in a single observation run (usually 28 minutes) at a time. This choice was made for three reasons. First it removes the issue on how to deal with the separation time between runs which can be of multiple days depending on the dataset. Second, it avoids the need to check if the existing code is robust when merging events from different, and not full runs. Finally it allowed for the construction of the new time interval creation technique using the already tested code for the generation of light curves with fixed time bins.

The spectral analysis module of Paris Analysis creates each required light curves one after the other in a specific class. There, the fixed time binning method is called for each observation run and loops over the needed time intervals to create light curves points until it reaches the end of the run. In the adaptive binning case we want to only compute the flux if a condition on the significance of the events is met. For each run we hence need to create new points as long as the run end is not reached; and each point is created after looping over their potential duration, stopping when the criteria is met. In order to reduce the computation time, the choice was made to increase the time intervals by 10 seconds steps up to the required significance. And then to reduce by 1 second steps to obtain the shortest interval still above the threshold.

The case when a point reaches the end of the run without enough signal also needs to be dealt with. For this purpose, the choice is left to the user between : 1) creating an upper limit, hence keeping the information about the associated time interval while identifying the lack of significance in the result file. 2) creating a light curve point, thus not all points will have the required significance but the light curve covers all the available data. 3) not saving anything, thus losing a - sometimes large - fraction of available events but keeping a uniformly created light curve.
The detailed algorithm is shown on Figure 3.2.

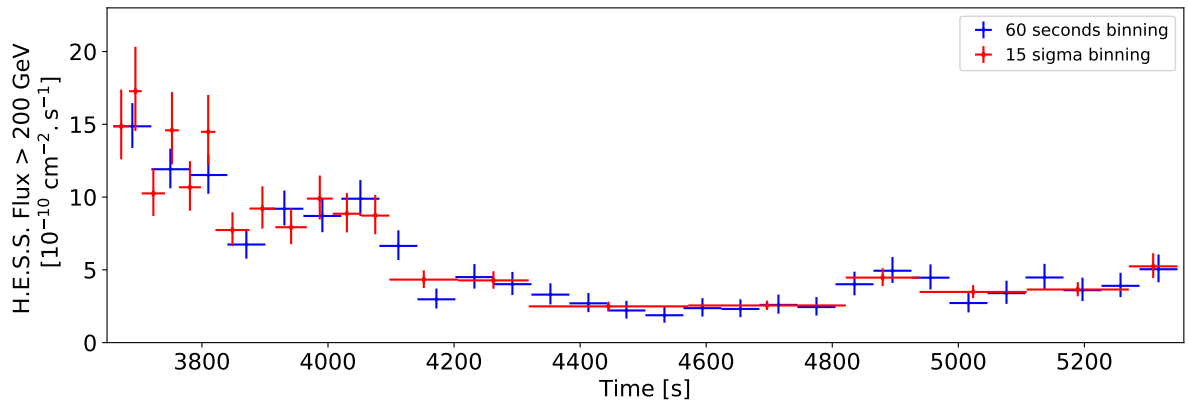

Figure 3.1: Example use of the adaptive light curve binning. Blue points represent a fixed 60 seconds binning while red points are binned to have more than 15 sigma of ON/OFF significance. The run used here is the third and last observation run on a particularly intense flare of PKS 2155-304 detected on July 28th 2006 [22]. This run was chosen as it contains a large flux variation from a very high state to a quieter state of the source. We see the integration time being shorter during periods of higher flux. The end of run without enough statistics is displayed as a point in this case.

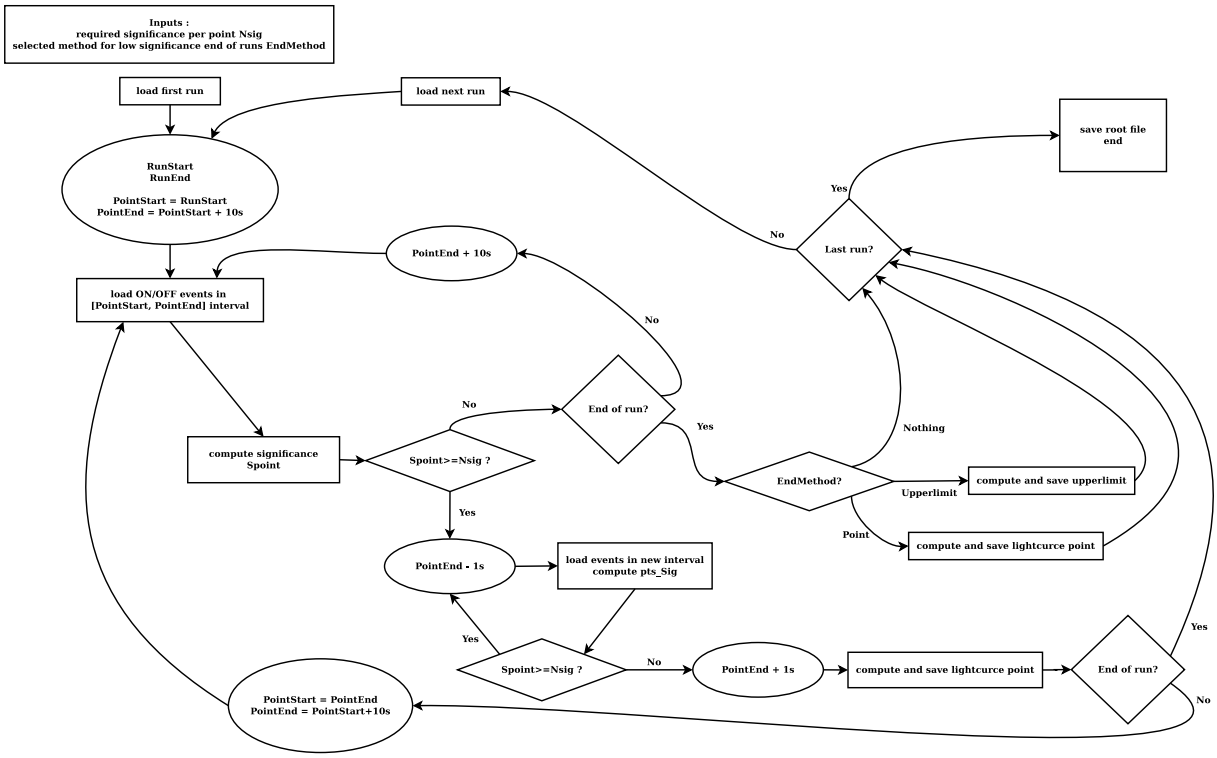

Figure 3.2: Detailed flow of the adaptive light curve algorithm. Squared boxes represent general actions. Diamond boxes represent tests with the test result being displayed on the output arrows. Elliptic boxes represent actions modifying values of time variables.

In term of user control, the adaptive binning light curve can be activated along any other light curve binning and requires the user to input the required significance as a number with decimals in a dedicated field. The choice of the method for the end of runs is done by selecting a button in the "advanced options" panel. Shown on Figure 3.3.

The method was also implemented in a previous version of gammapy[2] : a python analysis software in development for the Cherenkov Telescope Array (CTA). CTA will be an observatory composed of tens of imaging atmospheric Cherenkov telescopes in both hemisphere, and the successor of the current generation of IACT. The implementation was slightly different to the one presented here since the software uses good time intervals instead of observation runs to gather the events but remained similar. Large modification of the code in recent versions removed the adaptive binning creation, but it could be re-added at a later date.

3.2.3 Bayesian significance computation

The usual significance computation in H.E.S.S. follows the equation 17 in Li&Ma [75], adding the sign of the excess, which gives the signed significance of the signal measured in an ON region compared to the hypothesis of a random fluctuation of the background estimated in an OFF region. It can hence be negative if the ON region is subject to a negative fluctuation leading to a negative excess. It is also important to note that this significance computation is obtained using a frequentist statistic requiring tens of ON and OFF events to be reliable. To avoid this issue, a Bayesian significance computation was implemented for the adaptive light curve method and compared to the usual Li&Ma significance[3]. The original version of equation 17 in Li&Ma [75] would be even worse in this case as it would identify important negative excess as high positive significance (as shown in Figure 3.5).

In the Bayesian approach, we compute the probability of the hypothesis "There is a source in the ON region" based on the knowledge of the number of events in the ON and OFF region. The computation is based on Poissonian statistic and is valid for any number of events. Also, since the output is a probability instead of the statistical distance from the average of the observation, the associated significance is always positive. One of the main tool of the Bayesian statistics is the Bayes' theorem :

$$P(A|BI) = P(A|I)\frac{P(B|AI)}{P(B|I)} \tag{3.1}$$

Where $P(X|Y)$ means the likelihood of X knowing Y, A is an information we are interested in, I compile all previous knowledge, and B is a new information. It induces that the addition

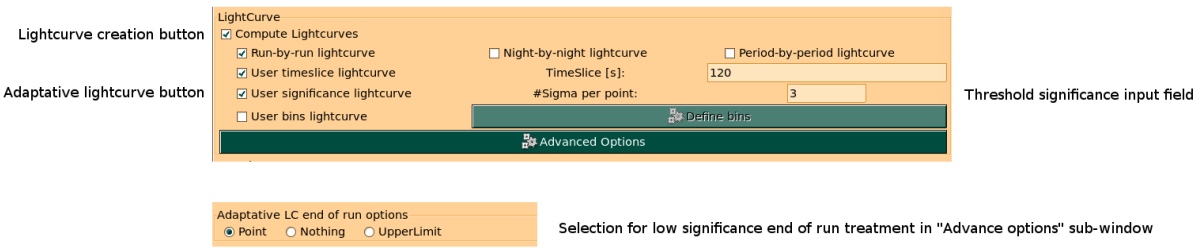

Figure 3.3: Part of the Paris Analysis GUI dedicated to light curve creation with added adaptive light curve functionality.

[2] https://gammapy.org/

[3] Refering, here and if not stated otherwise, to the signed version used in H.E.S.S.

of knowledge in the form of B allows to update our *prior* knowledge of A : $P(A|I)$, to obtain a posterior probability distribution $P(A|BI)$. $P(B|I)$ will be a normalisation factor.

Our goal will be to obtain $P(s=0|N_{ON}I)$, the probability of not having any signal s (average expected value of the number of signal events in the ON region) knowing the number of observed events in the ON region N_{ON} and any additional available information noted I. I will always include the fact that the number of observed events follows a Poisson law, and at some point in the following development it will also include our knowledge of the background b (average expected value of the number of background events in the OFF region) acquired using N_{OFF}.

Since we know that the OFF region contains only background events we have :

$$P(N_{OFF}|bI) = \frac{b^{N_{OFF}}}{N_{OFF}!}e^{-b} \tag{3.2}$$

Applying the Bayes' theorem and assuming no previous knowledge of b in the form of a flat (constant) prior, we trivially obtain :

$$P(b|N_{OFF}I) = \frac{b^{N_{OFF}}}{N_{OFF}!}e^{-b} \tag{3.3}$$

the probability density distribution of the background estimate using our measured N_{OFF}. This information will now be included in I.

Now in the ON region, we have both signal and background, and the expected number of background is $\alpha\ b$ where α is the ratio of acceptance corrected size of the ON and OFF regions. The total expected number of events is hence $s+\alpha\ b$ and :

$$P(N_{ON}|sbI) = \frac{(s+\alpha\ b)^{N_{ON}}}{N_{ON}!}e^{-(s+\alpha\ b)} \tag{3.4}$$

We can once again apply the Bayes' theorem :

$$P(sb|N_{ON}I) = P(sb|I)\frac{P(N_{ON}|sbI)}{P(N_{ON}|I)} \tag{3.5}$$

Now we can use the fact that s and b are independent to write $P(sb|I) = P(s|I)P(b|I)$ with our prior on the signal being taken flat and the Equation 3.3 representing our knowledge of b. Ignoring the normalisation terms we have :

$$P(sb|N_{ON}I) \propto (s+\alpha\ b)^{N_{ON}} b^{N_{OFF}} e^{-(s+\alpha\ b)} e^{-b} \tag{3.6}$$

In order to obtain $P(s|N_{ON}I)$ we now need to integrate over the values of b :

$$\begin{aligned} P(s|N_{ON}I) &\propto e^{-s}\int_0^{+\infty}(s+\alpha\ b)^{N_{ON}}b^{N_{OFF}}e^{-((1+\alpha)b)}db \\ &\propto e^{-s}\int_0^{+\infty}\Big[s^{N_{ON}}b^{N_{OFF}}+N_{ON}s^{N_{ON}-1}\alpha b^{N_{OFF}+1}+... \\ &\quad +N_{ON}s\alpha^{N_{ON}-1}b^{N_{ON}+N_{OFF}-1}+\alpha^{N_{ON}}b^{N_{ON}+N_{OFF}}\Big]e^{-(1+\alpha)b}db \\ &\propto e^{-s}\int_0^{+\infty}\Big[\sum_{i=0}^{N_{ON}}\frac{N_{ON}!}{i!(N_{ON}-i)!}s^i\alpha^{N_{ON}-i}b^{N_{ON}+N_{OFF}-i}\Big]e^{-(1+\alpha)b}db \\ &\propto e^{-s}\sum_{i=0}^{N_{ON}}\frac{N_{ON}!}{i!(N_{ON}-i)!}s^i\alpha^{N_{ON}-i}\int_0^{+\infty}b^{N_{ON}+N_{OFF}-i}e^{-(1+\alpha)b}db \end{aligned} \tag{3.7}$$

We can now perform the integration for each term of the sum (see associated Appendix A) to obtain coefficients c_i, and introduce a global normalisation coefficient N :

$$P(s|N_{ON}I) = N\sum_{i=0}^{N_{ON}}c_i\frac{s^i}{i!}e^{-s} \tag{3.8}$$

Each Poisson law in the sum is normalised, the full normalisation is thus obtained by taking N such that $N\sum_{i=0}^{N_{ON}}c_i = 1 = \sum_{i=0}^{N_{ON}}C_i$. Finally :

$$P(s|N_{ON}I) = \sum_{i=0}^{N_{ON}}C_i\frac{s^i}{i!}e^{-s} \tag{3.9}$$

With :

$$C_i = \frac{(1+\alpha^{-1})^i\frac{(N_{ON}+N_{OFF}-i)!}{(N_{ON}-i)!}}{\sum_{j=0}^{N_{ON}}(1+\alpha^{-1})^j\frac{(N_{ON}+N_{OFF}-j)!}{(N_{ON}-j)!}} \tag{3.10}$$

Applied to $s=0$, and explicitly stating the knowledge of N_{OFF}, the equation simplify strongly :

$$P(s=0|N_{ON}N_{OFF}I) = C_0 = \frac{\frac{(N_{ON}+N_{OFF})!}{N_{ON}!}}{\sum_{j=0}^{N_{ON}}(1+\alpha^{-1})^j\frac{(N_{ON}+N_{OFF}-j)!}{(N_{ON}-j)!}} \tag{3.11}$$

And this probability is then converted in number of equivalent Gaussian standard deviations to obtain the Bayesian significance of the signal.

Comparing the Li&Ma significance and the Bayesian significance, as shown on Figure 3.4 and Figure 3.5 :

- The significances are compatible above a relatively low significance of ~ 3 sigma in the high statistic regime (tens of ON and OFF events). Thus the Li&Ma formula could be used there and the implemented Bayesian computation converges to Li&Ma.

- The Bayesian significance is low but positive in the negative Li&Ma significance region as expected.

- Non negligible differences are visible in the low OFF events number, positive excess region. This implies that there is indeed a need to take the low statistic issue of the frequentist approach into account.

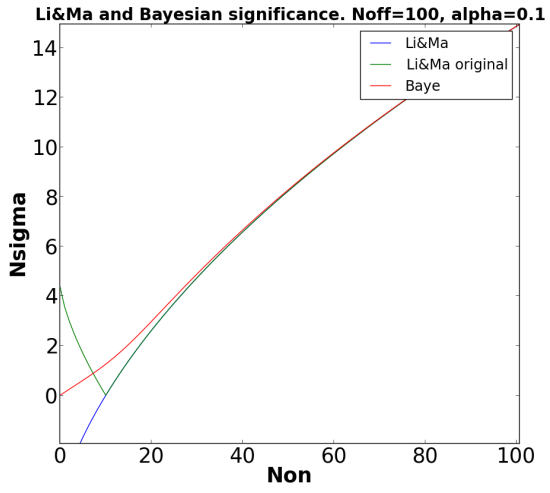

Figure 3.4: Comparison of the significance obtained using the frequentist Li&Ma formula and the newly implemented Bayesian computation. Here as a function of the number of events in the ON region, for a fixed number of OFF events and a ratio of ON/OFF livetime alpha of 0.1. The original, unsigned, Li &Ma formula is also shown.

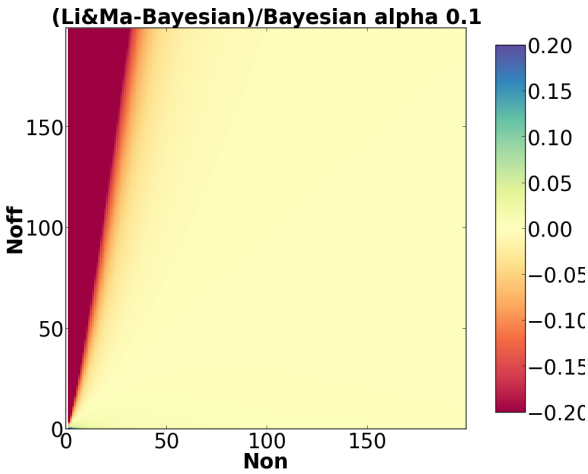

Figure 3.5: Fraction of difference between the significance obtained using the frequentist Li&Ma formula (in blue) and the newly implemented Bayesian computation (in red). The difference is visible at low statistic and low excess as expected.

We can conclude that the usual frequentist significance computation would work to create adaptive binning light curves as requiring less than 3 sigma per point would be very sensitive to signal fluctuations and defeat the interest of the method; but that the Bayesian approach is more stable for this purpose especially considering the shortest points which can be created in intense signal periods.

3.3 Bad time interval filtering

3.3.1 Problematic

When acquiring data, random issues can occur. Be it bad weather conditions, hardware failure or software bugs, it will potentially degrade our dataset. Some of these occurrences are taken into account during calibration or analysis and can hence be ignored. If it is not the case, then the quality of the data needs to be evaluated, which is performed on a run by run basis in the H.E.S.S. experiment.

When an issue occurs during a run, it will either be considered to have a small enough effect to keep the run, at the potential cost of a degradation of the analysis results, or it will be fully discarded. The goal of the bad time interval filtering tool is to remove parts of runs for which the issues are temporary. This is similar to the event filtering using good time intervals used at

other wavelengths such as during X-ray analysis, but with a reversed input logic. Two benefits : some discarded runs could be partially recovered and the global quality of kept runs could be improved.

Since the reasons for the user to remove a part of a run are numerous and complex, and do not affect every analyses in the same way, this tool does not perform the time interval selections but take them as a user provided input. It should also be noted that the tool is used at the analysis level. Therefore it does not require data recalibration. This makes the use of the tool easy, but may lead to biases if rapid observational properties evolution are not taken into account at this point or were incorrectly estimated at the calibration level due to the issue we are trying to remove.

3.3.2 Event filtering implementation

At the start of an analysis, if the tool is active every events in a run with associated intervals to be filtered will have their arrival time checked. If an event time is in a bad time interval it will be flagged to not be used in the analysis afterwards. The total livetime of each run will then be multiplied by the fraction of the run which was kept. The usual analysis can then mostly be performed as usual without further work. Significance studies and map will ignore the flagged events, and the event rate will be corrected for the removed duration since the run livetime is corrected.

Two pieces of information will be saved in the ROOT result file:

- the starting and ending time of each bad time interval
- the fraction of kept time for each run

This information allows the user to see if the tool was used, the input used and the effect it had. It can also be required for the second part of an analysis responsible for the spectral analysis and light curve computation. As stated previously, event rates are corrected on a run wise basis implying that spectrum and light curve will be correctly normalised when using full runs. An issue arises when sub-run binning are used. Indeed one point of the light curve can be fully, partially or not at all included in removed intervals. If the bad time interval filtering tool was used, the following procedure is performed for sub-run binning light curve creation :

- recover the original run livetime using the saved kept time fraction
- for each point find the overlap of the point time interval and every filtered intervals
- correct the livetime of each point

The tool is activated in the Paris Analysis GUI and requires a text file with on each line the number of the run to filter followed by the start of the interval and the end of the interval in Median Julian Day (MJD).

3.3.3 Example : Clouds during Crab Nebula observations

In order to test the tool, an intense source easily detected in one observation run is chosen : the Crab Nebula. Then, an observation run obtained during a night with moving clouds in the sky is chosen with the requirement that the run is partially affected by clouds and partially cloud free. The selection is made based on the trigger rate of the array which is stable under clean observation conditions and drops when clouds occult the Cherenkov light from air showers. The presence of clouds thus reduces the charge collected in the cameras, hiding some low energy events and with notable effects on the reconstruction including a bias of the reconstructed energies to lower values. The trigger rate evolution of the selected run is shown in Figure 3.6. Clear instabilities and a drop are visible at the end of the run which is indicative of the passage of clouds. Comparison will thus be made between the full run and when filtering all events after the thousandth second of the run corresponding to the yellow region in Figure 3.6.

In the full run, with a livetime of 1610 seconds, 285 ON events and 80 OFF events are selected with $\alpha^{-1} = 17.8$ the ratio of the OFF region livetime over the ON livetime. It corresponds to a detection significance of 36.0 sigma, with a signal over noise ratio of 62.3 and 10.45 ± 0.63 photons per minute from the source.

In the filtered run, the livetime is now 958 seconds, and 175 ON events and 55 OFF events are selected with $\alpha^{-1} = 18.2$. It corresponds to a detection significance of 28.0 sigma, with a signal over noise ratio of 56.9 and 10.77 ± 0.83 photons per minute from the source.

The ON events reduction (38.6%) is close to the livetime reduction (40.5%) but the reduction in number of OFF events is more limited (31.25%). This difference could be linked to an energy dependence of the absorption by clouds. The globally lower fraction of removed events compared to the removed livetime is logical as the clouds induced a reduced trigger rate of the telescopes.

When performing the spectral analysis, the reduced statistics induces a reduced usable energy range. The spectrum reconstructed using a power law hypothesis is fully compatible between before and after filtering as shown in Figure 3.7. It indicates that no bias is introduced by the filtering method. The light curve produced with 240 seconds bin is also shown in Figure 3.8. In the case of the full run, a drop of flux is seen at the end of the run. This is consistent with the harshest drop in trigger rate in Figure 3.6 meaning that it did cause a bias in flux if we assume that the source is stationary. The Crab Nebula is generally relatively stable and the time coincidence of the drop in trigger rate and flux reinforces this conclusion.

Comparing with the light curve from the filtered run, we can define three regions. In the first region, corresponding to the first 4 points of both light curves, no filtering is performed and the light curves are fully compatible. The slight differences in flux normalisation come from the difference in spectrum. The second region is the partially filtered region, corresponding to the 5th point. Here, the light curve point created in the filtered run case is only produced using the very beginning of the interval. Still the average flux is compatible with the full run case, i.e, no bias is seen. The large errors are explained by the low statistics available. A more correct way to display this point in the filtered run case may be to have it expand only up to the start of the filtered interval. The third and last region is the fully filtered region. Here no points are created for the filtered run as expected.

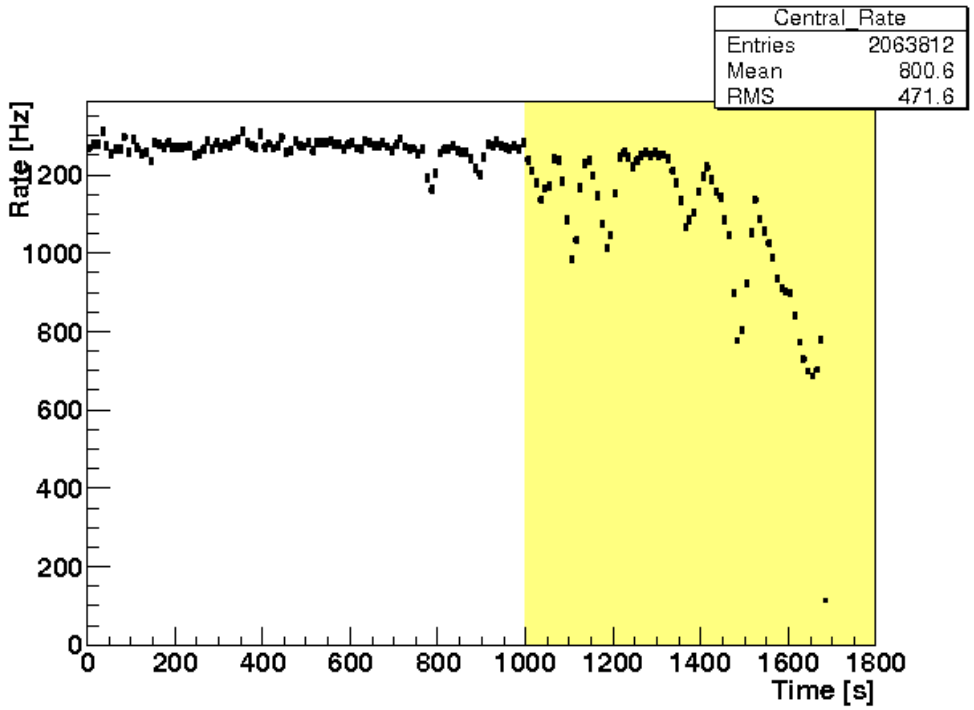

Figure 3.6: Trigger rate evolution of an observation run taken on the Crab nebula. Drops are visible and associated to clouds passing in front of the telescopes. The yellow area will be filtered to remove the affected part of the run.

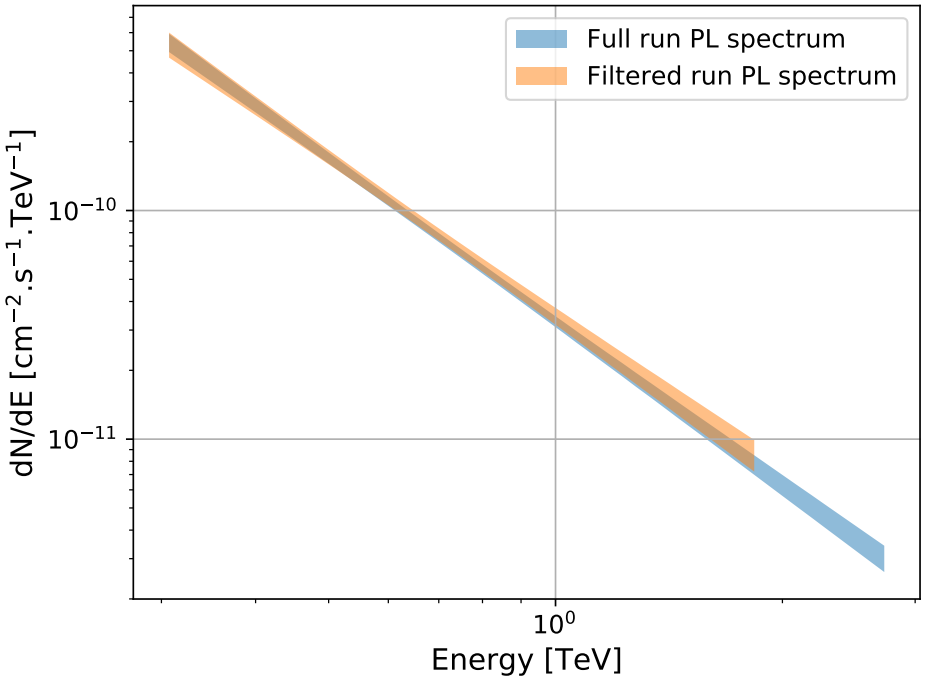

Figure 3.7: Comparison of the spectra obtained using a power law hypothesis between the full run and the run after applying a filter over the time period with unstable trigger rate.

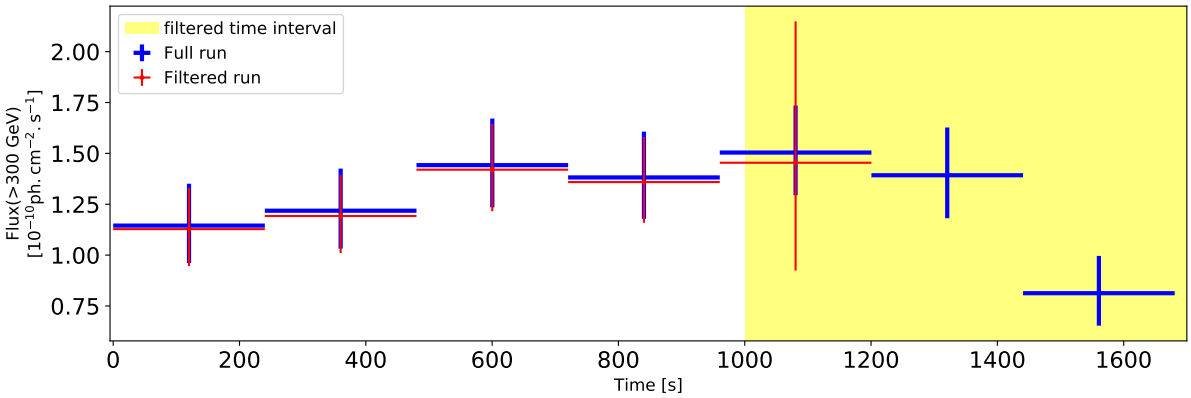

Figure 3.8: Comparison of the 240 binned light curves obtained with the full run and the run after applying a filter over the time period with unstable trigger rate. The yellow area corresponds to the filtered interval.

Chapter 4

Flare observations and analysis

Sommaire

4.1 The H.E.S.S. Target of Opportunities AGN program

The extragalactic sky seen at VHE is dominated by blazars but the low fluxes reaching us in this energy range imply that only the brightest[1] sources can be reliably detected in a reasonable time, if at all. Consequently, a large number of sources of VHE photons are only detected when observed in an above average bright state. In order to improve its potential scientific output, the H.E.S.S. experiment runs a variety of Target of Opportunities (ToO) programs. A ToO program makes use of available time sensitive information to perform motivated changes to the observation schedule. Along with the AGN one, the currently active extragalactic ToO programs include :

- Neutrinos : IceCube observes a diffuse flux of astrophysical neutrinos without identified sources. While answering the question of their origin would be of interest in itself, it would also improve considerably our knowledge of the physics of said sources. Indeed, neutrinos are produced through hadronic processes and would be a strong discriminant between leptonic and hadronic origins of the observed electromagnetic emissions at HE and VHE. The neutrino ToO program aims at detecting a VHE counterpart to astrophysical neutrinos. To do so, the program triggers observations following the detection of a neutrino with a very high probability of being of astrophysical origin – generally associated with an energy above the atmospheric neutrino energy – and reconstructed with a good spatial precision. A hint of association with a VHE detected blazar was recently obtained [36] but we are still far from a full understanding of this domain.

- Gravitational waves : With the start of the LIGO and Virgo experiments, and the regular detection of gravitational waves from mergers of compact objects (black holes and neutron stars), GW observation is now an active field of astronomy. The merging of two neutron stars is expected to produce a strong EM counterpart and was observed to do so [44]. In case of mergers involving black holes, little to no EM emissions are expected. The GW ToO program of H.E.S.S. aims at detecting VHE photons after a neutron star-neutron star merger detected as GW or, less likely, after novel event types such as black hole-neutron star mergers.

- Gamma-ray bursts : GRB are short flashes of gamma-rays. They are typically observed as an intense burst of a few seconds followed by an afterglow lasting hours to days. The burst is associated to an explosive process while the afterglow comes from the shocked material around the original explosion. Long GRB are usually considered to be spawned by the death of massive stars [82]. Short GRB on the other hand are associated with the merging of compact objects. It was directly observed with the spatially and temporally coincident detection of a short GRB and gravitational waves from the merging of two neutron stars [44]. In H.E.S.S., the GRB ToO program goal is the detection of both the prompt emission – which requires an automatic and fast response to alerts – and the afterglow. Thanks to such programs, the first detections of GRB at VHE were achieved in the two previous years with two seen with H.E.S.S. [83][84] and one with MAGIC [85].

[1] Speaking here of the flux density reaching Earth, and not the intrinsic luminosity at the source. Absorption plays an important role in suppressing the flux of distant sources at VHE

The AGN target of opportunity program aims at observing blazars in a flaring state. To do so, the group gathers multi-wavelength information from private communication and freely available data on a daily basis. If an interesting increase in flux is observed from a source, it is looked at in more details. First the available MWL data is compared to predefined thresholds, aiming to reject weak events that would carry no positive output. Visibility from the H.E.S.S. site is checked and additional information, including in particular the source redshift, are added to the discussion deciding on an observation strategy. The thresholds and general guideline are defined in the AGN ToO observation proposal of which I have been a co-instigator for several years. During the last proposal round, covering the observations for 2020, the AGN ToO was granted a total of 12 class-A[2] triggers divided between possible origin of the trigger (e.g. optical alerts, HE alerts, ...) for a total observation time of 110 hours. If the decision is taken to observe the AGN, the shifters on site are tasked with scheduling observations the following night. Then, every day, updated MWL data and real time analysis results of the previous night of observations with H.E.S.S. are used to decide on continuing or stopping the ToO observations.

The sources of information on the multi-wavelength status of AGN are :

- Multi-wavelength public alerts, distributed for example via Astronomer's Telegrams[3] and/or Gamma-ray Coordinates Network (GCN)[4].
- Public data from several experiments like Swift-XRT and FACT.
- Optical data obtained with the dedicated ATOM telescope located at the H.E.S.S. site.
- Private alerts from other collaborations operating facilities in the VHE domain, namely MAGIC, VERITAS, FACT and HAWC shared in the context of Memoranda of Understanding (MoU).
- Automatic, daily analysis of *Fermi*-LAT data using aperture photometry and a full likelihood analysis. These analysis are performed using the FLaapLUC pipeline [86].

The scientific value of AGN ToO observations is varied depending on the standard source flux, the brightness and duration of the flare, the multi-wavelength coverage available, the source redshift, ... Additionally, since the observations are time sensitive and IACT suffer from environmental constraints and limited observation windows, ToO data are prone to be of poor quality or low use.

4.2 Flare analysis

I performed the analysis of multiple flaring events observed during my thesis (or slightly before) from two sources : 3C 279 and PKS 2022-077. 3C 279 is a well known source already detected at VHE. Acquiring new spectral and resolved temporal information on the source, and the possibility of multi-wavelength studies motivated the observations. PKS 2022-077 was never detected at very high energy and is located at a high redshift for VHE observations as absorption

[2] Corresponding to high priority observations.
[3] www.astronomerstelegram.org/
[4] https://gcn.gsfc.nasa.gov/

by the EBL is important. Here temporally detailed data are unlikely since dividing a low excess in multiple time bins would show variations dominated by Poisson fluctuations, but a detection would be a new interesting result.

4.3 3C 279 flares in 2017 and 2018

3C 279 is a Flat Spectrum Radio Quasar (FSRQ) located at a redshift of $z = 0.536$ which is known for its variability at high energy (HE) and was previously detected by H.E.S.S. during a period of high activity seen with *Fermi*-LAT in 2015 [87]. Prior to this detection, 3C 279 was only detected twice at VHE by MAGIC in 2006 and 2007 [88][89] during bright optical flares. The source was active again in 2017 and 2018 and the observation and analysis of this activity is described in the following. In 2017, observations on 3C 279 were triggered twice following high states detected in the optical band. Later in 2017 and in 2018, observations were triggered four additional times following high states detected at HE with *Fermi*-LAT and brought to attention by alerts issued with `FLaapLUC`.

Most of the following study was shown at ICRC 2019 and was described in an associated proceeding [90]. New development using stereo analysis and concerning the June 2018 observations are also discussed.

4.3.1 High and Very High Energy Observations

As stated in subsection 2.3.3, all H.E.S.S. analysis are cross-checked with two independent calibration and analysis chains to ensure robustness of the results. I performed the analysis using Paris Analysis and the Model reconstruction and cross checks were obtained with ImPACT.

4.3.1.1 Four undetected flares

The choice was made to perform an analysis in Mono mode using only the CT5 telescope. This decision was taken following two main considerations. First, the understanding of the calibration of the recently upgraded HESS1 cameras, at that time, was still in development and potentially unreliable. Second, the source redshift is high enough to observe a non negligible absorption by the EBL at the higher energies, implying that a reduced energy threshold could be needed to detect the source. The VeryLoose cut were applied since the source has a soft spectrum and is located away from the galactic plane.

During the bright optical flare of March 2017, both observations with H.E.S.S. led to no detection in respectively 5.1 hours and 4.1 hours of live time. The HE flare seen by *Fermi*-LAT on the 25th of June 2017 was also not detected at VHE but was only covered by 0.7 hours of live time. The reduced length of usable observation by H.E.S.S. is due to bad weather. Observation times are displayed in Figure 4.3 along with multi-wavelength light curves. We see that the first observation in March occurred before the maximum activity in optical and during a quiescent state at high energy. The second observations occurred after the main optical flare and between two HE flaring events. Finally, the June observations, already very limited in duration, were obtained after a large decrease in the flux of the HE flare at the origin of the observations. Similarly, the February 2018 HE flare declined when H.E.S.S observation started. No significant excess was obtained with 4.1 hours of observation time.

4.3.1.2 January 2018 : Serendipitous detection of a short VHE flare

For the reasons stated in the previous section, an analysis in Mono mode with VeryLoose cuts was performed on this dataset.

In January 2018, bad weather delayed H.E.S.S. observations for more than a week after the decision to trigger observations was taken following the detection of enhanced activity at high energy by *Fermi*-LAT. While most of the HE flare was missed, a VHE flare was observed during the night between January 27 and 28 [91] while the high energy flux remained low. During the VHE flare night, a detection at a level of significance of 10.7 sigma was achieved with 1.7 hours of live time. The full campaign amounts for a total of 5.0 hours of live time. The full light curve is displayed in Figure 4.4.

It can be noted that this dataset was affected by a problem in the camera electronic of CT5 for a duration of 4 minutes during one of the runs of the flare night. During this time, 20% of the pixels in the camera were considered broken due to a problem with the electronic pedestals. While the overall run passed the run quality selection cuts, I developed the interval filtering tool described in section 3.3 to remove the problematic interval from the analysis. The effect on the analysis results was marginal : same signal over noise ratio, very close significance and compatible spectral analysis with derived spectrum parameter differing by $\sim 10\%$ of the error on these parameters. This is good since the run was accepted using the usual run selection, but means that the new filtering tool was not needed in this case.

4.3.1.3 June 2018 : Multiple day detection of a decreasing flare

Mono analysis

A full coverage of the decreasing phase of a HE flare seen by *Fermi*, as well as an extensive post-flare monitoring, was achieved in June 2018. After its first two nights of observations, H.E.S.S reported the detection of the source in the real time analysis both nights along with a report by ATOM of enhanced flux in the optical band [92]. A preliminary analysis, in mono mode with Loose cuts, of the full data set representing 18.7 hours of observation time reaches a significance of 11.8 sigma. Loose cuts are used instead of VeryLoose ones due to a poorly normalised background in maps created with the latter. This dataset contains low state observations acquired during the post-flare monitoring, which dilute the significance of the flare. Using a Bayesian block test [93], the data set is divided between periods of time corresponding to the high and low state of the source. The Bayesian block test identifies the optimal partition of the observation time into successives blocks characterised by significantly different event rates. To do so, it computes the likelihood of a given partition as the sum of the likelihood of each block fitted by a constant event rate and Poissonian variations. The optimal partition is thus obtained as the partition with the maximum likelihood. Details of the implementation in H.E.S.S. are given in [94]. Further analysis of the high state from MJD 58271 to MJD 58277 gives a significance of 13.5 sigma in 12.6 hours. Additionally, a very preliminary light curve was produced using a power law spectrum and fixing the photon index at a value of 3.7. It seemed to confirm the 6 nights high state and showed a decreasing trend consistent with the multi-wavelength light curves (shown in [90]).

When performing the spectral analysis of the high state period in mono mode, large tensions arise between the two analysis chains. An extensive search for the origin of the discrepancies was performed with no results.

New software version and stereo analysis

Since large developments occurred including new calibrations, bug fixing, and new telescope simulation; the decision was made to switch to the next main software version for both chains. This choice was expected to carry multiple advantages :

- correction of bugs potentially affecting the mono analysis. First, a bug causing the simulation to trigger excessively on NSB events. Second, a bias in the reconstructed energy of simulated events leading to an overestimated effective area at low energy.
- availability of run wise simulations[5] for the spectral analysis
- possibility to perform a stereo analysis using all 5 telescopes. The stereo analysis is expected to allow for a more precise reconstruction and better discrimination than in mono leading to improved results if the signal is not limited to the lowest energies.

Sadly a new bug affecting every analysis in mono appeared, suppressing the available statistic and biassing the fluxes to lower values. The new mono analysis is thus currently unusable in Paris Analysis. Exchanges with experts seem to indicate an origin of the issue with the Mean Scale Shower Goodness estimation. This is being investigated.

The new analysis in Stereo mode with CT1 to 5, with VeryLoose cuts, of the full data set representing 17.7 hours of observation time[6] reaches a significance of 19.7 sigma. Using the Bayesian block test, the previous division between periods of time corresponding to the high and low state of the source is found again. Further analysis of the high state from MJD 58271 to MJD 58277 gives a significance of 21.9 sigma in 12.0 hours with a signal over background ratio of 0.8 (see Figure 4.1 and Figure 4.2).

The slope of the new spectrum extraction, assuming a power law, is here compatible with ImPACT. While this is already a large improvement compared to the previous case, a discrepancy in normalisation is observed and the energy threshold in the ImPACT framework is abnormally high. Using the run wise simulation with Model, the difference in normalisation is reduced to a factor of ~ 1.5.

Similar differences in normalisation are seen by other analyses in the collaboration. Further work is thus required before a fully exploitable analysis of this dataset can be performed. A first overview of the spectral and variability properties is given in subsection 4.3.4.

4.3.2 Contemporaneous multi-wavelength observations

The flares were followed by multiple instruments covering a large variety of wavelengths. Details of the associated analysis performed by experts from the task force are given in this section as described in the ICRC 2019 proceeding [90].

[5] Usually, the spectral analysis uses a set of pre-produced tables giving the expected response of the array for diverse observation conditions and array configurations. Run wise simulations instead use specific tables produced for each run and taking into account the exact status of the telescopes during the run [95].

[6] the run selection is slightly different than the mono one as it takes the CT1-4 telescopes into account

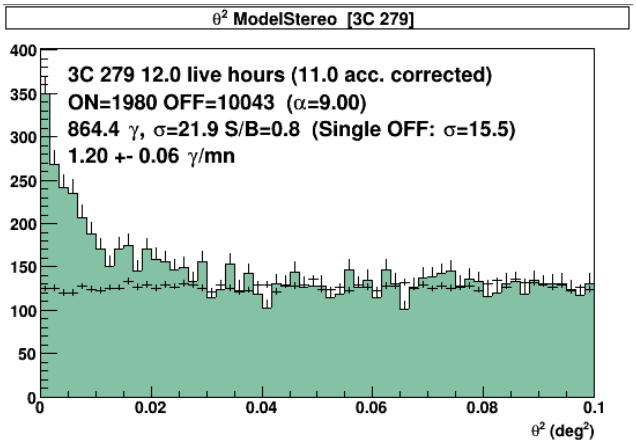

Figure 4.1: Histogram of the distribution of events in the ON and OFF region for 3C 279 in June 2018. θ is the angular distance between the event and the center of the ON (or OFF) region. The green bars represent the distribution of ON events while the black points are the distribution of OFF events scaled by α. A clear excess above the estimated background is visible at the center of the ON region. Events with $\theta^2 < 0.15$ are used to estimate the excess. This cut is chosen to account for the point spread function (PSF) of the instrument.

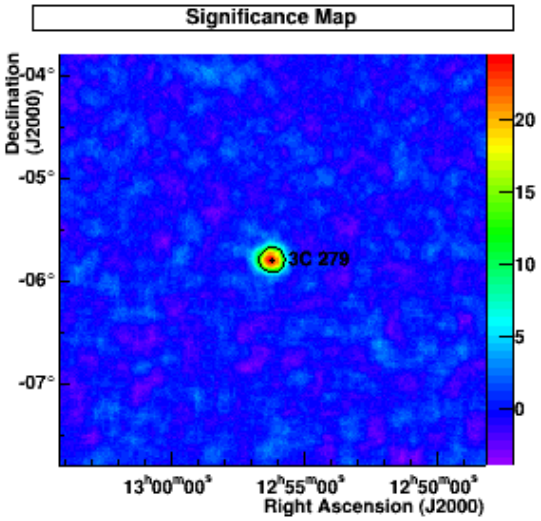

Figure 4.2: Map of the significance of the signal in the field of view around 3C 279 in June 2018. The map was created using the ring background technique (subsubsection 2.3.3.3). A strong, significant peak is visible at the position of 3C 279. The black circle around the source position is the PSF.

4.3.2.1 *Fermi*-LAT data

The GeV energy range is monitored by the *Fermi*-LAT telescope. The analysis of the data was done using the standard science tools provided by the *Fermi* collaboration (version 10.0.5) with Instrument Response Functions (P8R2) for photons of the SOURCE class (evclass 128, evtype 3) in the energy range 100 MeV - 500 GeV. The region of interest was a square with a side of 20 degrees centred on the source position. The background model was based on the 3FGL catalogue [96] and the diffuse emission models `gll_iem_v06.fits` and `iso_P8R2_SOURCE_V6_v06.txt`. The final parameters were obtained after a BINNED maximum likelihood fit. The daily light curves were obtained from the full time interval models fixing all the background sources except those flagged as variable in the 3FGL. For light curves with a shorter time binning, the starting point was the model of the daily interval with all parameters fixed except those of 3C 279. The data for 2017 were analysed in the time interval from 2017-02-01 to 2017-08-01 and the light curve is shown in Figure 4.3. The 2018 dataset was instead analysed from 2018-01-01 to 2018-06-20. Part of the light curve are shown in Figure 4.4 for January 2018 and Figure 4.5 for June 2018. The data show strong variability of the flux and of the photon index of the source.

4.3.2.2 Swift data

The Neil Gehrels *Swift* observatory [97] is comprised of three instruments, among which the XRT [98] detects X-rays between 0.2 and 10 keV, and the UVOT observes at UV and optical wavelengths. Following the detection of flaring activity at various wavelengths, ToO observations

have been requested to the Neil Gehrels *Swift* Observatory. *Swift* observed 3C 279 with two instruments: the X-Ray Telescope (XRT) and the UV/Optical Telescope (UVOT). Analysis of Swift observations has been performed using HEASOFT 6.23. All XRT spectra are consistent with a power-law emission absorbed by Galactic material (model tbabs*powerlaw in Xspec). The absorbed integral flux between 0.3 and 10 keV is reported in Figure 4.3 and Figure 4.4.

4.3.2.3 ATOM data

The Automatic Telescope for Optical Monitoring [99] is an optical telescope located at the H.E.S.S. site in Namibia. It provides optical monitoring on known gamma-ray emitters as well as multi-wavelength support for target-of-opportunity events and covered all presented events in R and B bands. Data was reduced and analysed using ATOM's automatic analysis pipeline ADRAS version 2.6.12. Fluxes are obtained via differential photometry using between 2 and 4 custom calibrated comparison stars. Light curves are displayed in Figure 4.3 for 2017, Figure 4.4 for January 2018 and Figure 4.5 for June 2018.

4.3.3 Multi-wavelength correlation study

The 2017 and 2018 ToO observation campaigns on 3C 279 led to two particularly interesting H.E.S.S. datasets. For the January 2018 short VHE flare, the high significance short time scale and strong VHE variation mirrored by a weaker HE evolution add new interesting properties compared to the previous detection. The June 2018 dataset on the other hand is particularly interesting due to the extended observation with H.E.S.S. observations covering multiple days of HE activity. This allowed for the strongest detection of 3C 279 with H.E.S.S. to date and access to evolution on time scale of multiple days.

During all those campaigns, multi-wavelength observations were performed. Two behaviours concerning the correlation between optical and HE can be observed. Some flares were visible in HE while the optical flux remained constant. This can be seen with the HE flare after April 2017 (see Figure 4.3). While others displayed strong increase in both energy bands. For each one when H.E.S.S. also observed, we looked at the correlation between the optical fluxes seen by ATOM and HE fluxes seen by *Fermi*.

To compute the uncertainties on the correlation coefficients, a set of simulated datasets is built. For each point in the correlation plot, 500 new ones are simulated having a 2D tilted Gaussian distribution with the errorbars as width and the Pearson's coefficient derived from the original points as a correlation factor. The final result is a distribution of correlation coefficients. Here we report the 50th percentile as the reference value and we use the 16th and 84th ones to derive the uncertainties on it.

Between MJD 57805 and 57840, corresponding to the optically active flares of early 2017, elevated fluxes in optical or HE are associated with elevated fluxes in the other band (See Figure 4.6) but the correlation is quite loose (Pearson coefficient $= 0.61 \pm 0.05$). Between MJD 58130 and 58148, corresponding to the January 2018 flare, large HE increase with low optical flux increase as well as optical increase with no HE increase are visible (See Figure 4.7). Hence a low correlation (Pearson coefficient $= 0.41 \pm 0.02$). Between MJD 58268 and 58288, corresponding to the June 2018 flare, a strong correlation is visible (See Figure 4.8). The Pearson coefficient reaches 0.91 ± 0.03 and HE variations appear more than twice as important as optical variations.

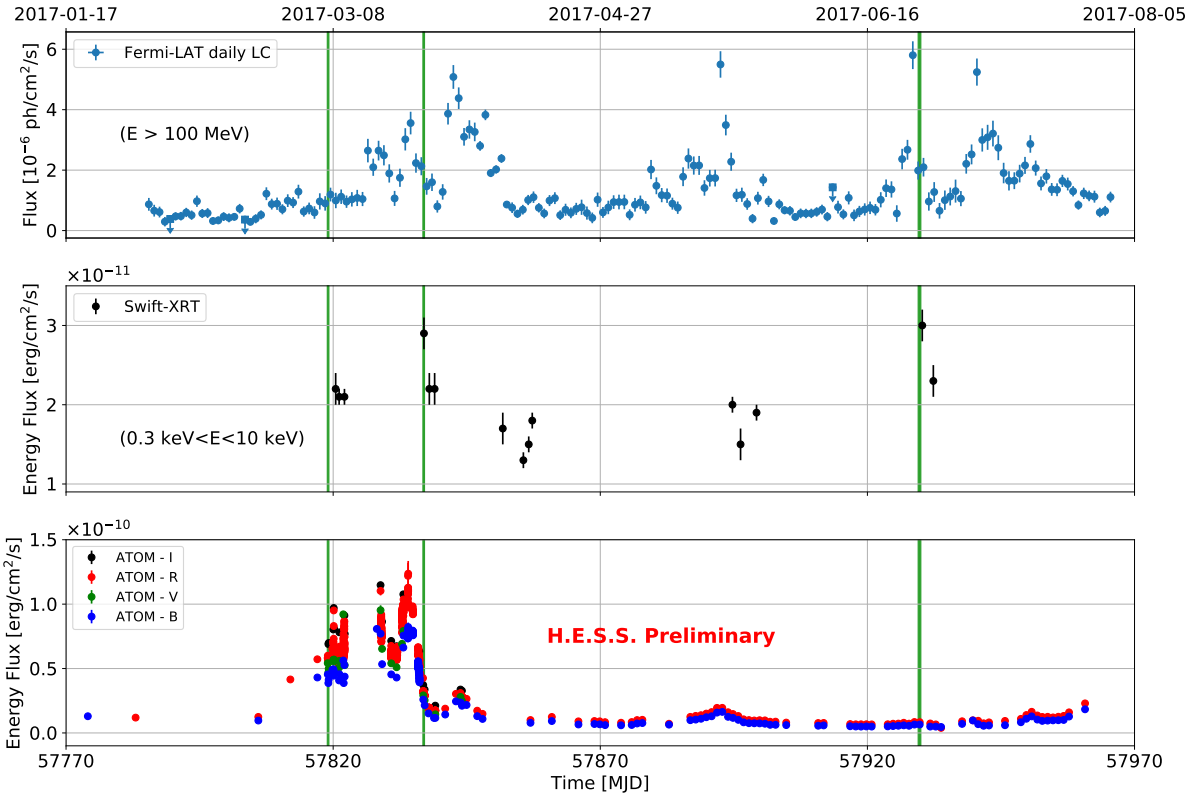

Figure 4.3: Multi-wavelength observations of 3C 279 in 2017. H.E.S.S. time of observations are displayed as green vertical lines.

4.3.4 Discussion on the VHE detections

The previous detection with H.E.S.S. of 3C 279 in June 2015 [87] achieved a significance of 8.7 σ in one night during the decreasing phase of one of the brightest flare of the source as seen with *Fermi*-LAT [100]. The associated spectral analysis, with an energy threshold of 66 GeV, was performed assuming a power law spectrum. A photon index of $4.2 \pm 0.3_{stat} \pm 0.2_{syst}$ was found. The average flux, integrated above 100 GeV was $6.5 \pm 0.6_{stat} \pm 1.3_{syst} \times 10^{-11}$ cm^{-2}s^{-1}. The simultaneous spectra at HE and VHE allowed to derive constraints on the position of the emission region. Indeed, high and very-high energy gamma-rays are assumed to originate from the same process and consequently to be characterised by a common intrinsic spectrum. Additionally, radiation from the broad line region can absorb VHE photons. Thus the opacity affecting the VHE photons escaping the AGN in the jet is dependent of how deep in the BLR photon field the emission region is located. The BLR is modeled using the model by Finke [101], which derives the stratification of the emission lines in the BLR based on reverberation mapping observations. The model allows for two geometries: a simple spherical shell and an infinitesimally thin ring motivated by observations of a flattened BLR [102]. Both geometries were used with the ring geometry leading to lower opacities. For the intrinsic spectrum, three spectral shapes are tested. Namely a log-parabola, a broken power law and a power law with a sub-exponential cut-off. Additionally, the absorption by the EBL is taken into account using the model by Franceschini et al. [103]. For each spectral shape and BLR geometry the distance to the central black hole and the spectrum parameters were optimised together. The study showed no preference for the

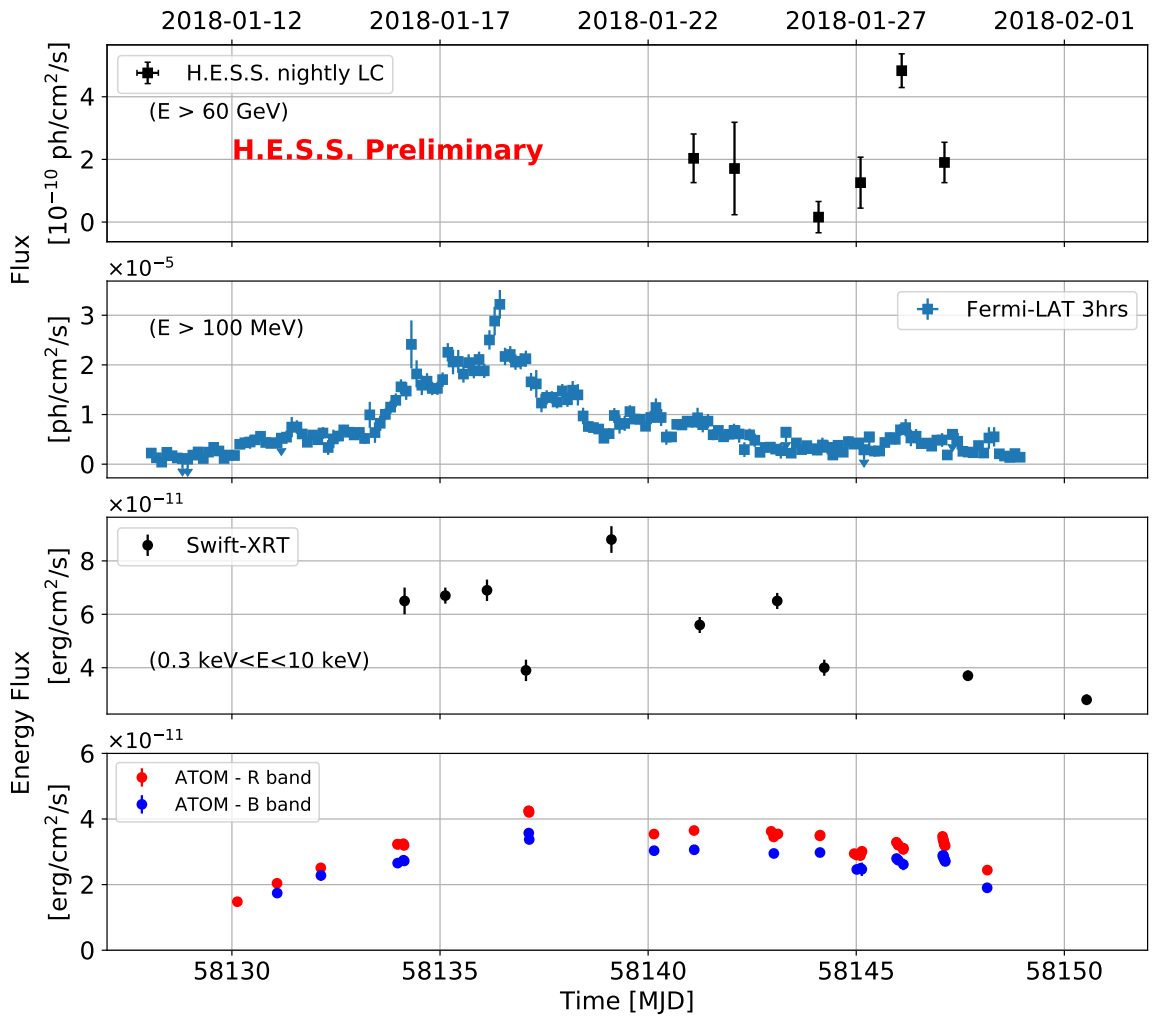

Figure 4.4: Multi-wavelength observations of 3C 279 in January 2018. Very different variability behaviours are visible between all wavelengths. A nightly binning is applied to the ATOM observations.

existence of an absorption feature. The most conservative lower limit on the distance between the central SMBH and the emission region thus places it outside the BLR.

The January 2018 flare is interesting as it was a short flare at VHE mirrored only mildly at HE. The flux at VHE during the flare night was characterised by a flux more than a factor two above the values of the day before and after. At HE, only an increase by a factor 1.5 was observed. Assuming a power law, the spectrum of 3C 279 extracted during the flare night with H.E.S.S. is of photon index 4.35 ± 0.29 with an energy threshold of 60 GeV; very similar to the index from June 2015. Estimating the absorption coefficient by the BLR using the model by Finke [101], values similar to the case of June 2015 are found. Thus similar constraints on the position of the emission region are expected implying an emission region outside the BLR [104]. Slight tensions were observed with the cross-check analysis. In light of the way larger spectral issue observed in June 2018 and the posterior discovery of bugs, a re-analysis will likely be performed later. It may also take advantage of the availability of the new simulations for the upgraded HESS1 cameras to perform a stereo analysis.

The detection in June 2018 is the most significant one at VHE to date. It is also the detection covering the longest period of time with a high state of 6 nights. Previously, only the first detection by MAGIC covered 2 nights [88] (with only the second one being independently significant at more than 5σ). Using the Stereo analysis including all 5 telescopes, two spectral hypotheses are fitted to the high state as seen with H.E.S.S. Assuming a power law, the spectrum of 3C 279 is of photon index 4.5 ± 0.2 above a threshold of 91 GeV. Alternatively, assuming an intrinsic power law affected by the EBL using the model by Franceschini et al. [103], the photon index of the power law at the source is 3.0 ± 0.2 (Figure 4.9). No spectral hypothesis is significantly preferred with a χ^2 of 251.3 with EBL and 256.1 without EBL for 247 degrees of freedom.While the fitting process cannot differentiate significantly between the two hypotheses, the intrinsic spectrum of the source is obviously affected by the EBL. Extracting the absorption coefficient from the Franceschini model[7], an attenuation of the flux of around 20% is expected at ~ 105 GeV, and increase with energy reaching, e.g., 80% at ~ 260 GeV. The light curve corresponding to the integrated flux above 100 GeV is shown in Figure 4.5. It was produced using the power law with EBL spectrum obtained in the 6 nights high state. The VHE light curve tracks very nicely the evolution of the HE and optical light curves. This indicates a common emission region and process. The existence of a multi-wavelength coverage of the flare is promising for time dependent modelling. The strong correlation between wavelengths indicates a common emission process, consequently the model will be constrained over a large energy range. Additionally, the variability carries information on , e.g., particle escape time, evolution of the emission region properties,...; which adds additional constraints to the models.

4.3.5 Conclusion

3C 279 is located at a redshift high enough to observe a significant absorption of VHE photons by the EBL. Being an FSRQ, its SED also peaks at lower energy than BL lacs objects. The double detection by H.E.S.S. of the source in 2018 during flaring activities is thus exciting especially considering the specificities of those detections. The January 2018 flare is unique in that it was a serendipitous detection of a short VHE flare with little HE counterpart. It is likely to be re-analysed before a deeper study is performed in light of the new development in software and the access to stereo analysis. The June 2018 flare is the most promising dataset as it was detected for multiple days by at least 3 instruments in optical, at high energy and at very high energy. The exploitation of the VHE data was delayed significantly by the appearance of bugs in the experiment software in a period of development of the software requiring large changes and simulations to account for the new HESS 1 cameras.

A deep study of the flaring events of 2017 and 2018 is planned in the future and will be covered in a dedicated paper.

[7] http://www.astro.unipd.it/background/

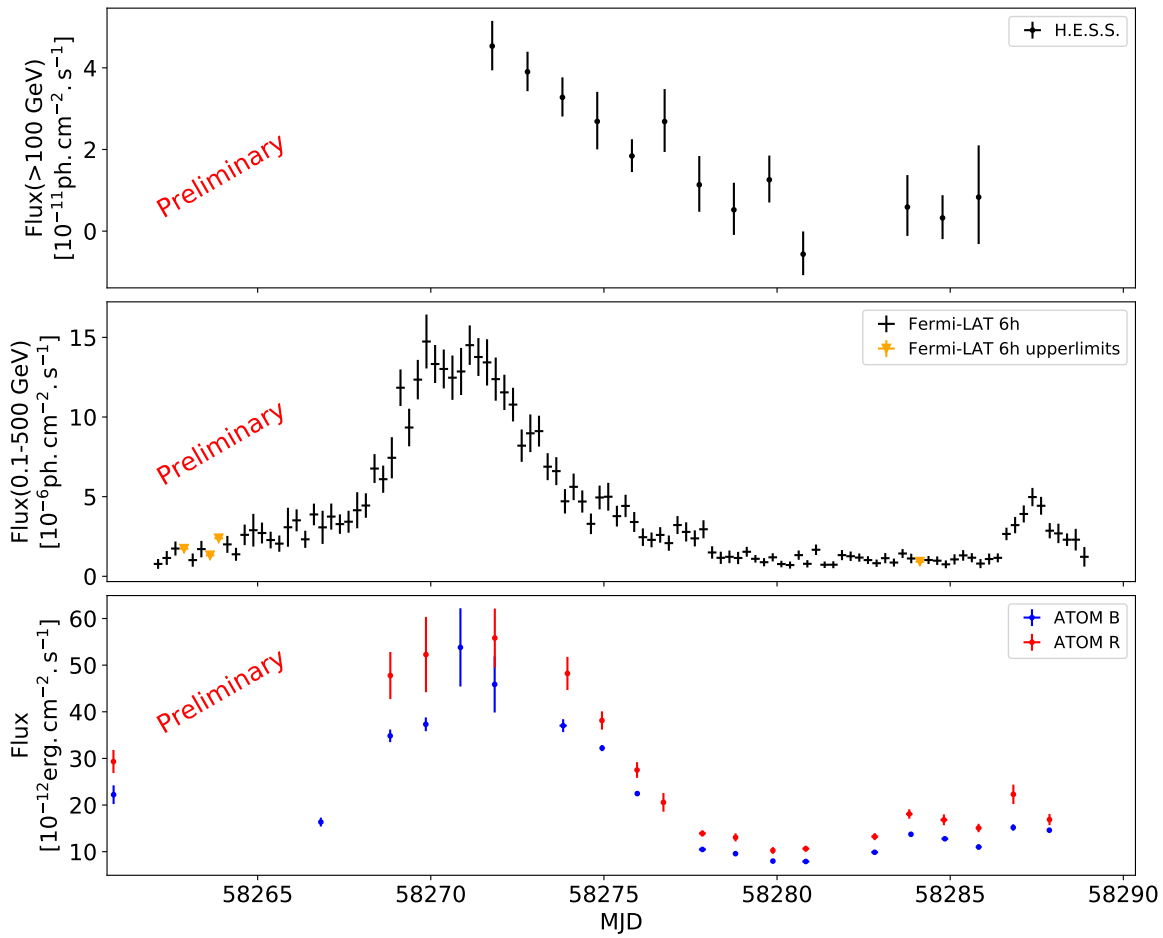

Figure 4.5: Multi-wavelength observations of 3C 279 in June 2018. Top panel : H.E.S.S. preliminary light curve above 100 GeV. Obtained using the Stereo analyis with CT1-5 and a power law with EBL spectral hypothesis. Middle panel : The *Fermi*-LAT light curve with 6 hour bin and flux integrated between 100 MeV and 500 GeV is displayed with black points and orange triangles for the upper limits. Bottom panel : Optical flux seen by ATOM in the R and B band with a nightly binning

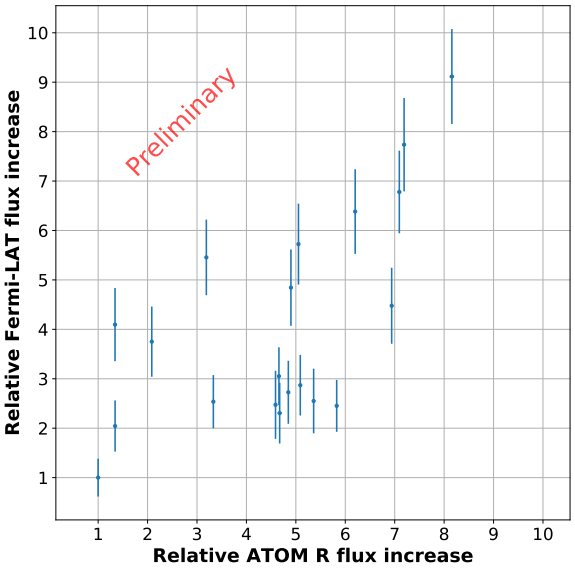

Figure 4.6: Comparison between the flux variation of *Fermi*-LAT and ATOM R during the optical flare of 2017 from MJD 57805 to 57840

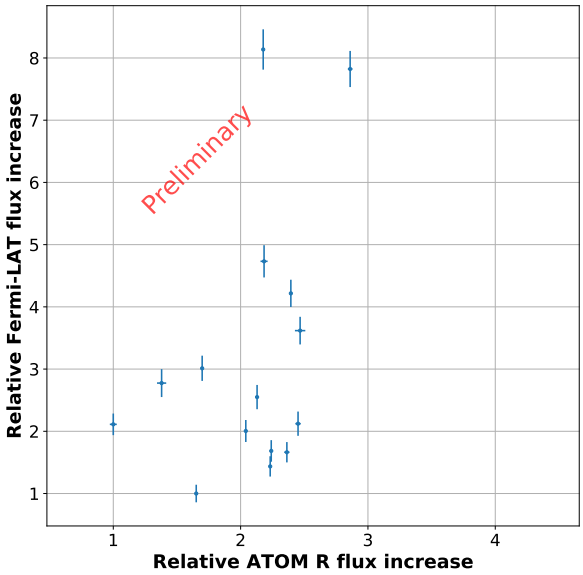

Figure 4.7: Comparison between the flux variation of *Fermi*-LAT and ATOM R during the January 2018 flare from MJD 58130 to 58148

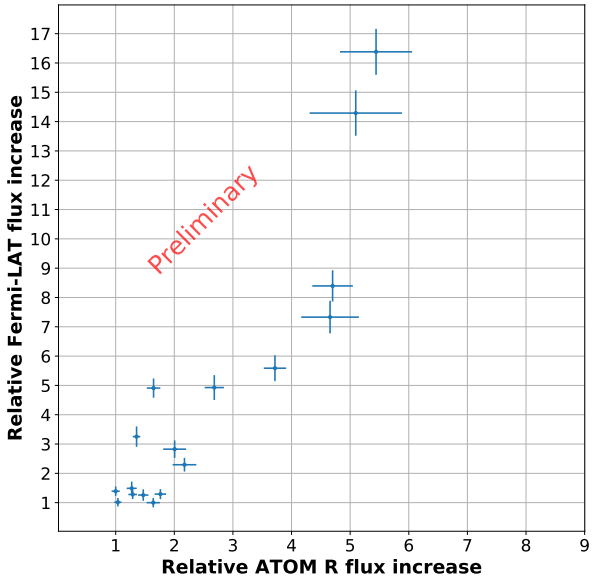

Figure 4.8: Comparison between the flux variation of *Fermi*-LAT and ATOM R during the June 2018 flare from MJD 58266 to 58288

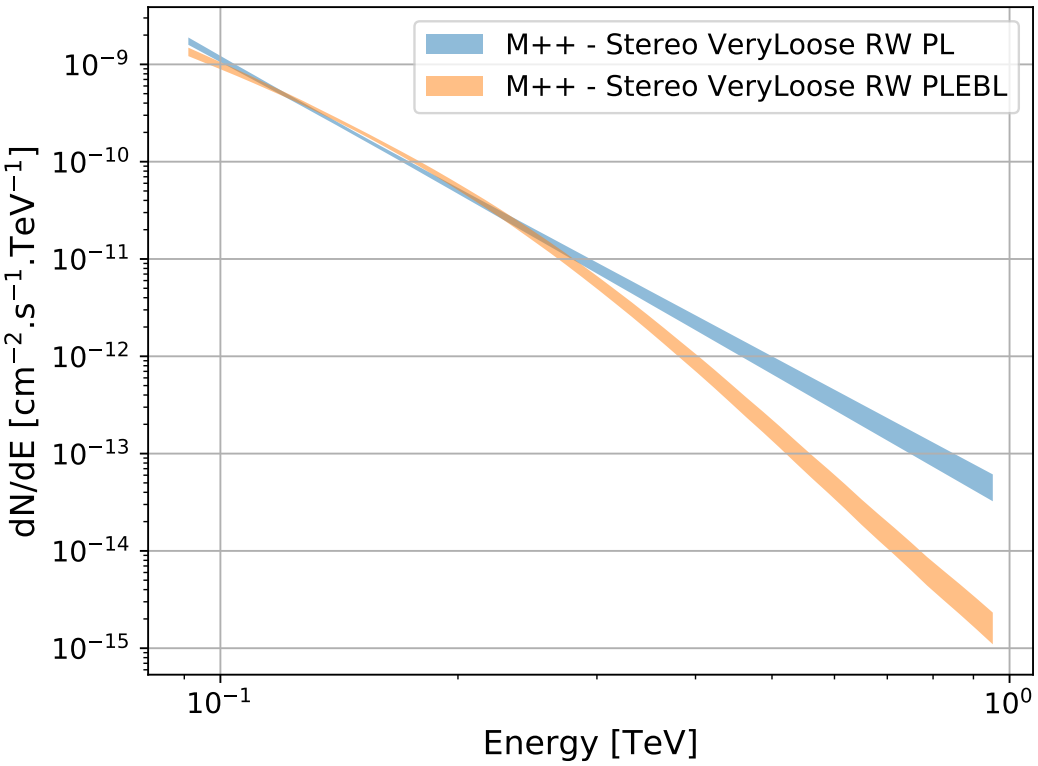

Figure 4.9: Spectrum of the June 2018 flare of 3C 279. The spectral hypothesis used are a simple power law, and a power law with absorption by the EBL using the model by Franceschini et al. [103].

4.4 PKS 2022-077 flares in 2016 and 2017

PKS 2022-077 is a flat spectrum radio quasar located at a redshift of z = 1.388. Even if PKS 2022-077 intrinsic emission at VHE were significant, absorption by EBL photons makes detections impossible or would require an exceptionally bright AGN. As part of the AGN ToO program, H.E.S.S. observations were triggered following a high state detected with AGILE [105] and *Fermi*-LAT [106] in April 2016, and in September 2017 and October 2017 following private communication from the *Fermi*-LAT team and alerts issued with FLaapLUC.

The following study was shown as a poster at ICRC 2019 and was described in an associated proceeding [107]. This work was performed by the members of the task force in which I was coordinator and responsible for the H.E.S.S. main analysis.

4.4.1 High and Very High Energy Observations

The April 2016 flare was observed by H.E.S.S. for 56 minutes at the start of the flare. The observations were limited by the short observation window available from the H.E.S.S. site at the time : the source was elevated only for a short duration at the end of the dark time. During the September 2017 flare, 155 minutes of observation were possible at the start of the flare and 358 minutes at the end. The peak of the high energy flare could not be observed by H.E.S.S. due to technical issues preventing CT5 from observing. In October 2017, the decreasing phase of the high energy flare was observed for 336 minutes. Detailed observation times are displayed on Figure 4.11-a.

Since PKS 2022-077 is located at a high redshift, and absorption by the EBL is more efficient at higher energies, an analysis with a lower energy threshold is more likely to detect an excess signal. Consequently, analysis of the data taken for each flare was performed in mono mode using CT5 only and using VeryLoose cuts. As stated in subsection 2.3.3, all H.E.S.S. analyses are cross-checked with two independent calibration and analysis chains to ensure robustness of the results. I performed the analysis using Paris Analysis and the Model reconstruction and compatible results were obtained with ImPACT.

No detection was possible for each period (see, e.g., Figure 4.10) and only upper limits on the flux could be derived. The 95% C.L. differential upper limits obtained assuming a photon index of -3 are shown in Figure 4.12. The 95% C.L. integral upper limits above threshold are also produced with the same spectral hypothesis. The difference in energy threshold is due to different zenith angle of observation i.e. different elevation of the source during observation. For each flare the zenith angle, energy threshold and integral upper limit are compiled in Table 4.1.

4.4.2 Multi-Wavelength campaign

The flares were followed by multiple instruments covering a large variety of wavelengths. Details of the associated analysis performed by experts from the task force are given in this section as described in the ICRC 2019 proceeding [107]. While not the expert for this publication,

Flare	Zenith	$E_{threshold}$	Flux($> E_{threshold}$) (ph.cm^{-2}.s^{-1})
April 2016	37.0	108 GeV	$< 3.3 \times 10^{-11}$
September 2017	20.1	73 GeV	$< 5.2 \times 10^{-12}$
October 2017	24.6	73 GeV	$< 9.1 \times 10^{-12}$

Table 4.1: H.E.S.S. zenith of observation, energy threshold and integral upper limits

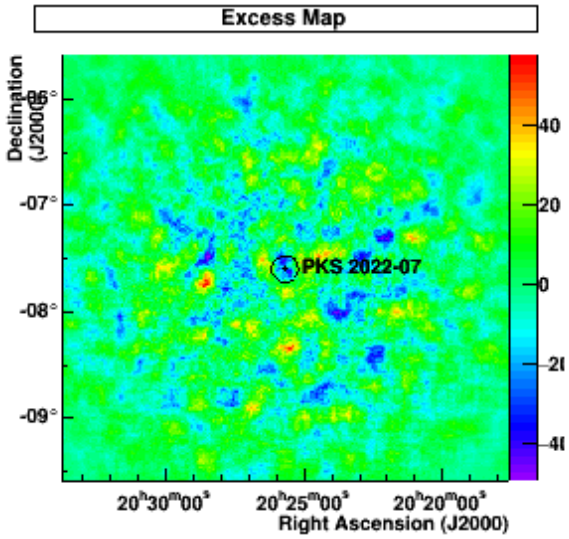

Figure 4.10: VHE excess map of PKS 2022-077 in September 2017. The map is compatible with pure background. Created using the ring background technique (subsubsection 2.3.3.3).

I used this occasion to learn how to perform a simple *Fermi*-LAT data analysis on the September and October 2017 datasets.

4.4.2.1 High Energy observations

AGILE is a space mission containing two instruments: a gamma-ray detector, sensitive to photons with energy in the range 30 MeV–50 GeV, and a hard X-ray detector, sensitive in the range 18–60 keV. AGILE reported [105] a flux of $(2.3 \pm 0.8) \times 10^{-6}$ ph cm^{-2} s^{-1} ($E > 100$ MeV) integrated from 2016-03-25 12:00 UT to 2016-03-27 12:00 UT.

Fermi-LAT data were analysed in several subsets, in order to have contemporaneous results with the HESS observations (Table 4.2) for the three flares. We used the standard *FermiTools*[8] software version `1.0.0` and the Pass 8 event selection (event class and instrument response functions `P8R3_SOURCE_V2`). For each flare, spectra and light curves were derived using the binned likelihood analysis `gtlike` package in the energy range 100 MeV to 500 GeV. The region of interest is 10°of radius, and the recommended selection of time intervals are used (`DATA_QUAL>0 && LAT_CONFIG=1`). Events are selected with a zenith angle below 90°. The source input model was built based on the 3FGL catalogue, using the `make3FGLxml` user-contributed script, and includes the Galactic interstellar emission model (`gll_iem_v06`) and the relative isotropic diffuse emission template (`iso_P8R3_SOURCE_V2`). The likelihood fit is performed iteratively: first, the model is used as per the 3FGL catalogue. In a second step, sources for which TS<9 and contributing to less than 5% of the event counts in the whole data set have all their parameters fixed[9]. Finally, in a third iteration, the parameters of all sources beyond 3°from PKS 2022-077 are fixed. Considering the short time intervals for the flares presented in this study, we assume a power-law shape for the spectrum of PKS 2022-077, even though PKS 2022-077 is best described with a log-parabola spectrum in the 3FGL catalogue [96][10]. We checked with a log-likelihood ratio test for each flare period that a log-parabolic spectral shape does not improve significantly

[8] https://github.com/fermi-lat/Fermitools-conda

[9] The test statistic (TS) used here is -2ln of the ratio of likelihood of the source and no source hypothesis.

[10] As well as in the 4FGL catalogue [108].

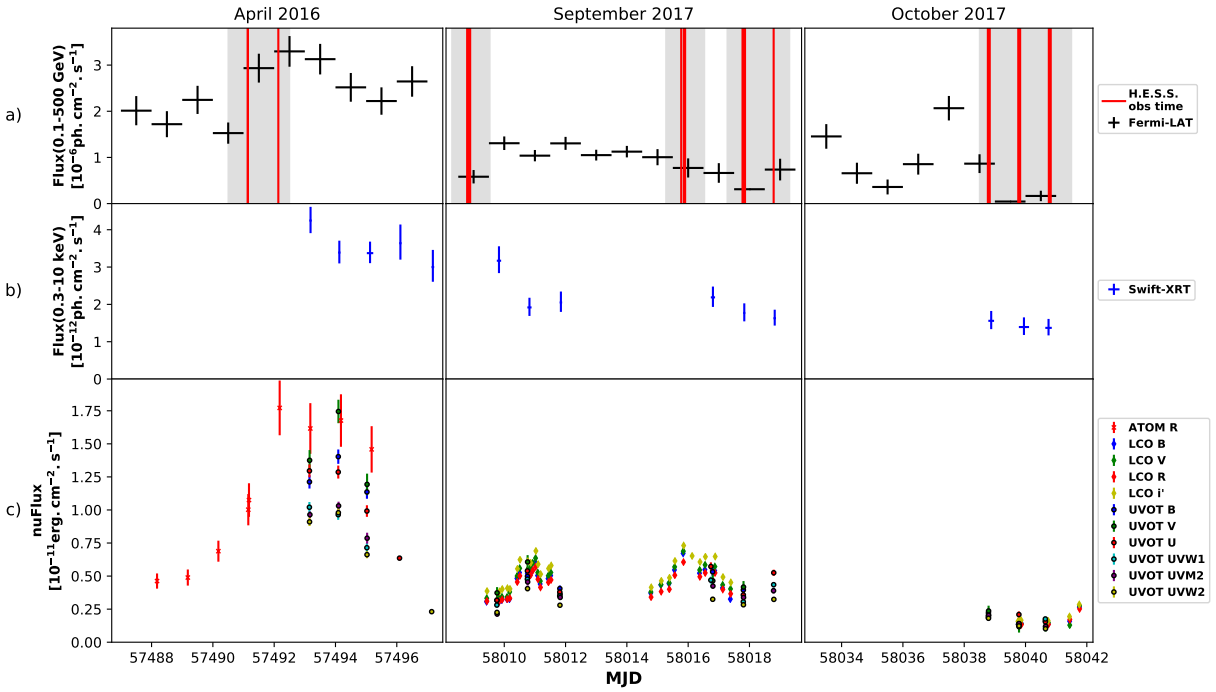

Figure 4.11: Multi-wavelength observations of PKS 2022-077. **a)** *Fermi*-LAT daily binned light curve integrated between 100 MeV and 500 GeV. Red lines represent H.E.S.S. observations and the shaded grey areas cover the time windows used for the *Fermi*-LAT spectral analysis (shown in Figure 4.12). **b)** X-rays light curve with *Swift*-XRT integrated between 0.3 and 10 keV. **c)** optical fluxes with ATOM and LCO and optical/UV fluxes with *Swift*-UVOT.

the fit results[11]. The most intense flare was found to happen in April 2016 but was not the most covered with H.E.S.S. The daily binned light curve is displayed on Figure 4.11-a.

4.4.2.2 X-ray observations

Swift-XRT observations were triggered following the H.E.S.S. observations. XRT data, which were all acquired in the standard photon counting mode, are analysed using the `HEASoft` suite version 6.22.1. Events are cleaned using the standard criteria from `xrtpipeline`. Data from PKS 2022-077 are extracted within a circle of 20 pixels, and the background is taken from an annular region with an inner radius of 50 pixels and outer radius of 160 pixels. `XSpec` version 12.9.1p is used for the spectral analyses, where events below 0.3 keV are excluded. Accounting for a Galactic hydrogen column of $3.24 \times 10^{20}\,\mathrm{cm}^{-2}$ [109], energy flux measurements, assuming

Flare	Calendar date	MJD	MET	Duration (h)	Model	Flux 0.1−500 GeV (ph.cm^{-2}.s^{-1})	Photon index	Range (GeV)	Signif
apr16	12 Apr 2016 at 12:00−14 Apr 2016 at 12:00	57490.50−57492.50	482155204−482328004	48.0	PL	$(2.53 \pm 0.21) \times 10^{-6}$	1.83 ± 0.05	0.1−25	30.7
sept17-a	12 Sep 2017 at 07:00−13 Sep 2017 at 12:46	58008.29−58009.53	526892408−526999588	108.8	PL	$(5.77 \pm 0.87) \times 10^{-7}$	2.0 ± 0.1	0.1−10.7	17.0
sept17-b	19 Sep 2017 at 06:33−20 Sep 2017 at 12:47	58015.27−58016.53	527495609−527604445						
sept17-c	21 Sep 2017 at 06:34−23 Sep 2017 at 07:24	58017.27−58019.31	527668446−527844258						
oct17	12 Oct 2017 at 12:00−15 Oct 2017 at 12:00	58038.50−58041.50	529502405−529761605	72.0	PL	$(3.12 \pm 0.79) \times 10^{-7}$	2.2 ± 0.2	0.1−2.2	7.9

Table 4.2: *Fermi*-LAT spectral analysis results

[11] With ΔTS of respectively 7.8, 4.4 and 1.0 for April 2016, September 2017 and October 2017.

a power-law spectral shape, in the energy range 0.3–10 keV for each exposure contemporaneous with H.E.S.S. observations are reported on Figure 4.11-b.

4.4.2.3 Optical observations

Simultaneously with Swift-XRT, PKS 2022-077 was monitored in the ultraviolet and optical bands between 170 and 600 nm with Swift-UVOT. All ultraviolet and optical magnitudes and fluxes have been calculated using `uvotsource` procedure including all photons from a circular region with radius 5". The background was determined as a circular region with a radius of 10". UVOT light curves are on Figure 4.11-c. All data points are corrected for dust absorption using the extinction derived from the measured extinction in the B-V band following [110]. In this case, the reference extinction used is $E(B-V) = 0.0328$.

ATOM provides optical monitoring on known gamma-ray emitters as well as multi-wavelength support for target-of-opportunity events and covered the 2016 flare event in R band. Data was reduced and analysed using ADRAS 2.4.14. Fluxes are obtained via differential photometry using between three and six custom calibrated comparison stars. The associated light curve is shown on Figure 4.11-c.

The *Las Cumbres Observatory* (LCO) is a worldwide network of robotic telescopes. During the 2017 flares, LCO observed the target in B,V,R,i′ filters. Pre-reduction was performed with the LCO pipeline and differential photometry was performed using PyRAF. Differential photometry was performed using six comparison stars in the same field of view with magnitudes derived from the PanSTARR1 survey [111]. The light curve is shown on Figure 4.11-c.

4.4.3 Study of the high energy cut-off

4.4.3.1 Problematic

Extrapolating the *Fermi*-LAT power-law spectra near-simultaneous with H.E.S.S. observations for each flare (taking all *Fermi*-LAT observations in the grey areas on Figure 4.11-a, also detailed in Table 4.2) and taking into account absorption by the EBL with the model by Dominguez et al. [112], we can compare them with the H.E.S.S. differential upper limits (Figure 4.12). The 95% C.L. upper limits at VHE probe lower fluxes than the *Fermi*-LAT extrapolated spectra. Clearly, a simple power-law extrapolation and standard EBL absorption are not compatible with the non-detection in April and September, whereas the H.E.S.S. upper limits for October can be explained with a simple power-law extrapolation of the intrinsic blazar spectrum.

To explain the non-detection at very high energy, three hypotheses are tested independently using a code by Manuel Meyer. The first hypothesis is the existence of an intrinsic cut-off in the emission region between the *Fermi*-LAT and H.E.S.S. energy ranges. This cut-off would be naturally linked to the maximum energy of the particles accelerated in the jet. The second hypothesis is a different normalisation of the EBL than the one from the model used in the extrapolations. The last hypothesis is the absorption of the VHE photons in the broad line region (BLR) around the AGN. This would imply that the emission region is close enough to the central black hole to be affected by the BLR. All constraints are reported as one-sided 95 % confidence levels.

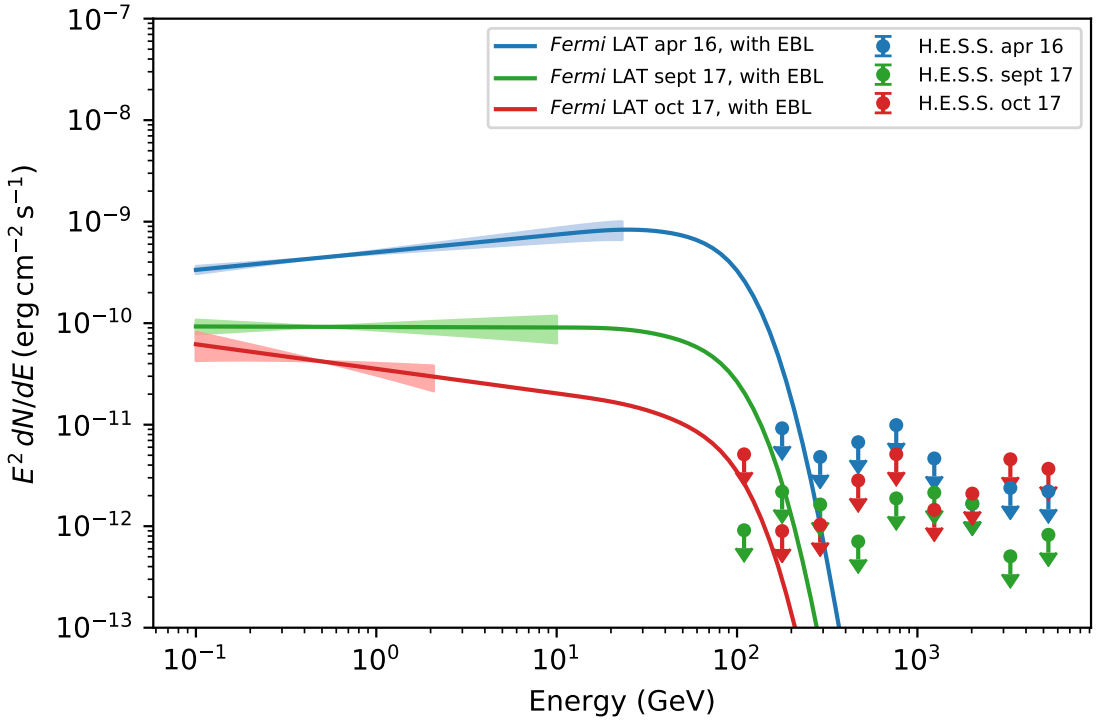

Figure 4.12: H.E.S.S. 95% C.L. differential upper limits obtained for each observation campaigns. Contemporaneous *Fermi*-LAT power law spectra obtained from the greyed period on Figure 4.11-a) (see also Table 4.2) and extrapolated at VHE with the same power law corrected by the EBL absorption following the model by Dominguez et al. [112] are also displayed.

4.4.3.2 Profile likelihood ratio test

To perform the study, we assume that the H.E.S.S. measurements are Gaussian random variables and accordingly, the H.E.S.S. upper limits in each energy bin can be translated into a Gaussian likelihood profile, see Figure 4.13.

The *Fermi*-LAT spectrum is extrapolated taking into account the hypothesis under study. For a given extrapolation of the *Fermi*-LAT SED, the predicted flux level is used in each energy band to obtain the likelihood of this upper limit bin. The summed likelihood obtained by summing over each bin thus gives the likelihood of obtaining the H.E.S.S. upper limit given the extrapolated *Fermi*-LAT SED. Using a profile likelihood ratio test [113], we can then evaluate if a given extrapolation is compatible with the H.E.S.S. data.

The likelihood ratio test statistic $\lambda(\pi)$ is the ratio of the likelihood of our hypothesis evaluated at a value of the control parameter π over its maximum. A property of this statistics is that $-2log(\lambda)$ converges to a chi-square random variable with k degrees of freedom (Wilk's theorem [114]; see also, e.g., theorems 10.3.1 and 10.3.3 in [115]), where k is the number of degrees of freedom in our hypothesis (one in our case). Performing a likelihood ratio test consists in selecting the region of the parameter space where $-2log(\lambda) <$c. In our case, c is selected to correspond to a 95% one sided confidence level. The test statistic (TS $= -2log(\lambda)$) variation for a distribution with one degree of freedom corresponds to c $= 2.71$ for the limits we want to derive. For each hypothesis, π is the varying parameter. The $-2log(\lambda)$ distribution for the

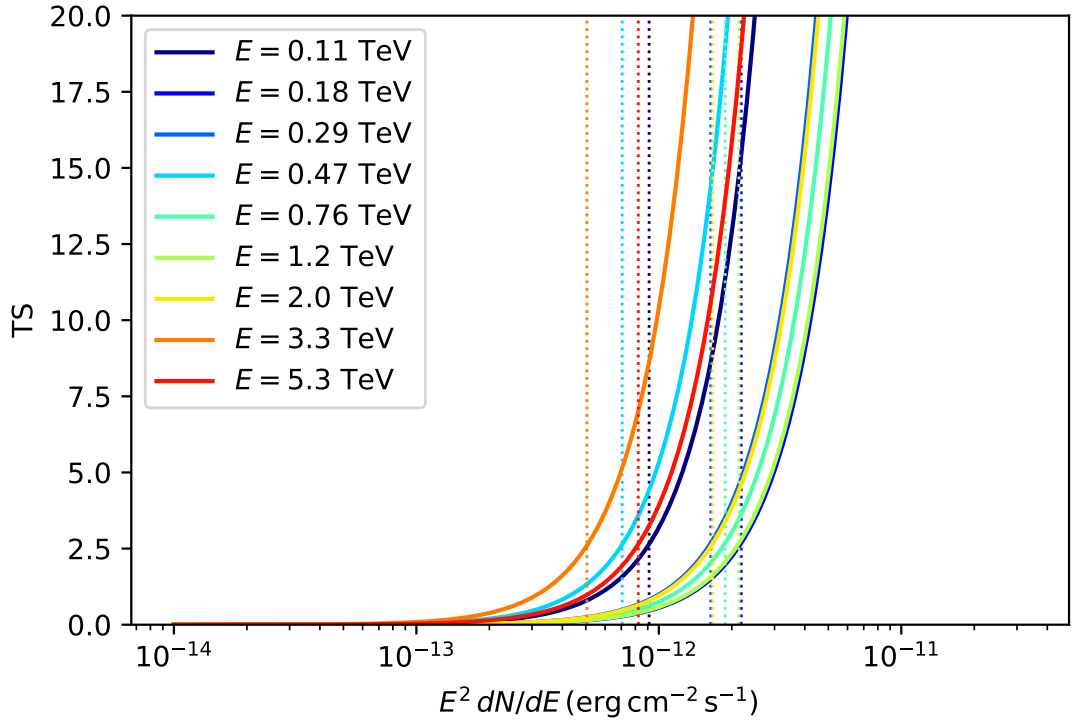

Figure 4.13: Profile likelihood of the flux of PKS 2022-077 for each energy corresponding to a differential upper limit point of the September 2017 flare. The dotted lines correspond to the associated 95% CL flux upper limit. Since the profile likelihood follow a χ^2 distribution with one degree of freedom, the 95% upper limits (one sided) correspond to a TS value of 2.71

energy cut hypothesis applied to April 2016 and September 2017 is shown in Figure 4.15. The true maximum of our likelihood is for the lowest possible flux. It is here evaluated using the maximum over the explored range of our parameter, which is correct as long as the likelihood is near constant farther outside of the tested range. It seems to be verified in Figure 4.15 were the TS remains constant = 0 at the lowest value of energy of the cut-off. A similar procedure is applied for the other two hypotheses.

4.4.3.3 Results

First, we vary the normalization, n_{EBL}, of the EBL photon density (modeled with model of Dominguez et al. [112]) and compute the profile likelihood as a function of n_{EBL} as displayed in Figure 4.14. We find that one would have to increase the EBL density by at least a factor of 3.07 and 1.39 for the September 2017 and April 2016 observation campaigns, respectively. Such high levels of the EBL are not compatible with luminosity functions of galaxy and other gamma-ray measurements [112, 116].

Next, we test the hypothesis of an intrinsic cut-off in the emission region, represented by a power law spectrum modified with an exponential cut-off at energy E_{cut}. Again computing the profile likelihood this time as a function of E_{cut} (Figure 4.15) we find that $E_{\mathrm{cut}} < 128$ GeV for the April 2016 flare and $E_{\mathrm{cut}} < 35$ GeV for the September 2017 flare. In a scenario where very high-energy gamma-rays are produced in inverse Compton scattering of electrons with external

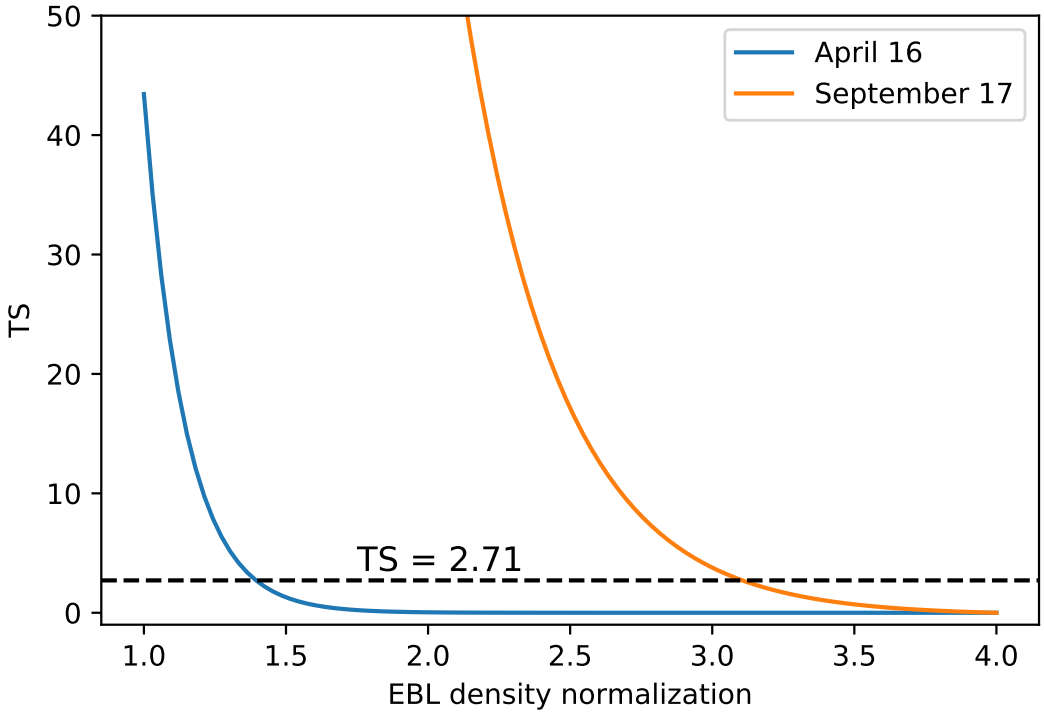

Figure 4.14: Test Statistic obtained with the profile likelihood ratio test as a function of the EBL normalisation in our modified EBL density hypothesis for the April 2016 and September 2017 flare. The dashed line correspond to the 95% probability limit on the parameter space of the hypothesis. Here the function is monotonous so only a lower limit on the value of n_{EBL} is derived.

radiation fields, as commonly assumed for FSRQ [117], this would imply a cut-off or break in the electron distribution at a Lorentz factor in the comoving frame $\gamma' = \delta_{\rm D}^{-1}\sqrt{E_{\rm cut}(1+z)/(2E_0)}$ if the electrons scatter predominantly off photons at energy E_0 in the Thomson regime [101] and where $\delta_{\rm D}$ is the Doppler factor. Assuming $\delta_{\rm D} = 20$, we arrive at $\gamma' \lesssim 3.2\times10^3$ for scattering off BLR photons at 10 eV, $\lesssim 1.4\times10^3$ for scattering with accretion disk photons at 50 eV, and $\lesssim 3.2\times10^4$ for scattering with photons of the dust torus at a temperature of 1000 K for $E_{\rm cut} < 35$ GeV.

Lastly, we test if the cut-off could be due to the interaction of VHE gamma-rays with BLR photons. Following Ref.[118], we use the BLR model of Finke [101], where we assume the ring geometry, and calculate the profile likelihood as a function of the distance r of the gamma-ray emitting region to the central supermassive black hole as shown in Figure 4.16. Searching the literature, we did not find estimates of the disk or Hβ luminosity and neither for black hole mass of PKS 2022-077. Therefore, we assume $L_{\rm disk} = 10^{46}\,{\rm erg.s^{-1}}$ and $L({\rm H}\beta) = 10^{43}\,{\rm erg.s^{-1}}$, which corresponds to a total BLR luminosity of $0.03L_{\rm disk}$ using the scaling relations of Ref.[101], and a black hole mass $M_\bullet = 10^9\,M_\odot$, where $M_\odot$ is the solar mass. While these values can vary strongly from one source to the other, the limit we derive (given in cm) depends only on $L(\mathrm{H}\beta)$. Most radio loud AGN are measured to have $L(\mathrm{H}\beta) > 10^{43}\,{\rm erg.s^{-1}}$ [119] so our limits will likely be over-

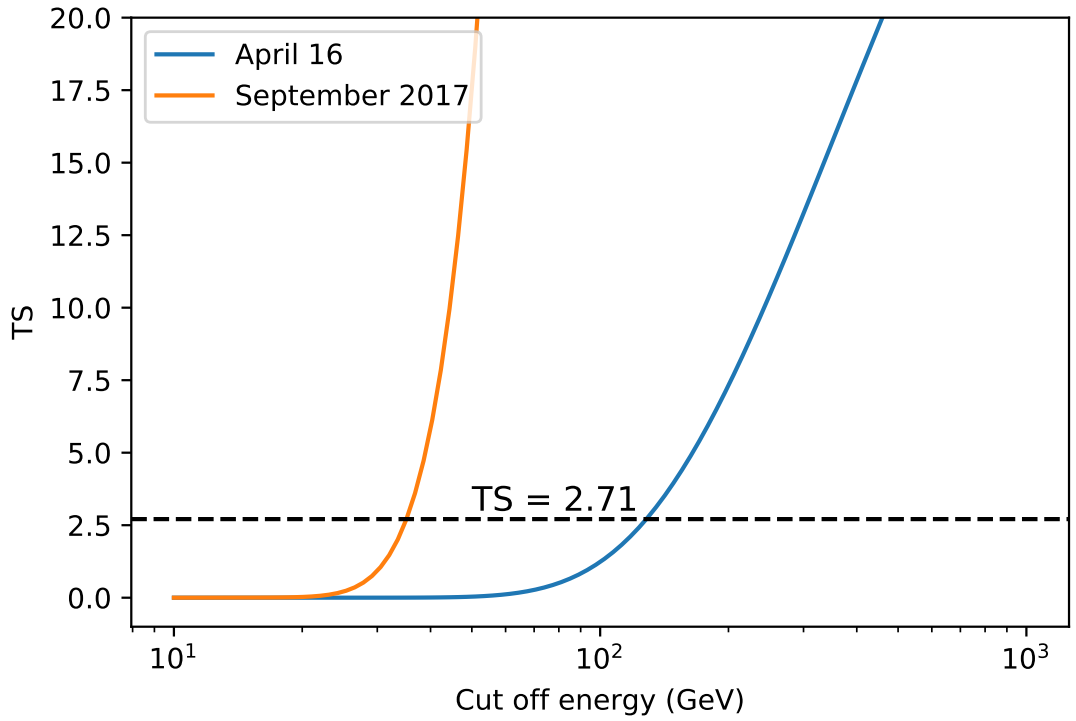

Figure 4.15: Test Statistic obtained with the profile likelihood ratio test as a function of the cut-off energy in our intrinsic cut-off in the emission region hypothesis for the September 2017 flare. The dashed line correspond to the 95% probability limit on the parameter space of the hypothesis. Here the function is monotonous so only an upper limit on the value of E_{cut} is derived.

constrained[12]. The H.E.S.S. data are compatible with a power-law extrapolation of the LAT spectrum and BLR absorption if the emission region is closer than $r = 1.8 \times 10^{17}\,\mathrm{cm} \sim 1200\,r_g$ ($r = 9.5 \times 10^{16}\,\mathrm{cm} \sim 650\,r_g$) for the April 2016 (September 2017) flare, where $r_g = GM_\bullet/c^2$ is the gravitational radius with the gravitational constant G and the speed of light c.

4.4.4 Conclusion

After the detection of bright activity phases at high-energy gamma-rays, H.E.S.S. observed PKS 2022-077 in three occasions in April 2016, and September and October 2017 leading to no detection at very high energies. Even with the strong EBL absorption expected at a redshift of 1.388, the extrapolation of the high-energy gamma-ray spectra is incompatible with the upper limits derived for the April 2016 and September 2017 flares. Three hypotheses were tested to explain the non-detection by H.E.S.S. using a profile likelihood ratio test. A correction to the EBL density compared to the model by Dominguez et al. is ruled out due to the large correction factor which would be needed and is incompatible with the measured values. Rather, the non-detection is either caused by a break in the emitted spectrum or absorption of VHE photons

[12]For instance, $r \leq 9.5 \times 10^{16}\,\mathrm{cm}$ in September 2017 becomes $r \leq 4.5 \times 10^{17}\,\mathrm{cm}$ when increasing the assumed luminosities by a factor 10.

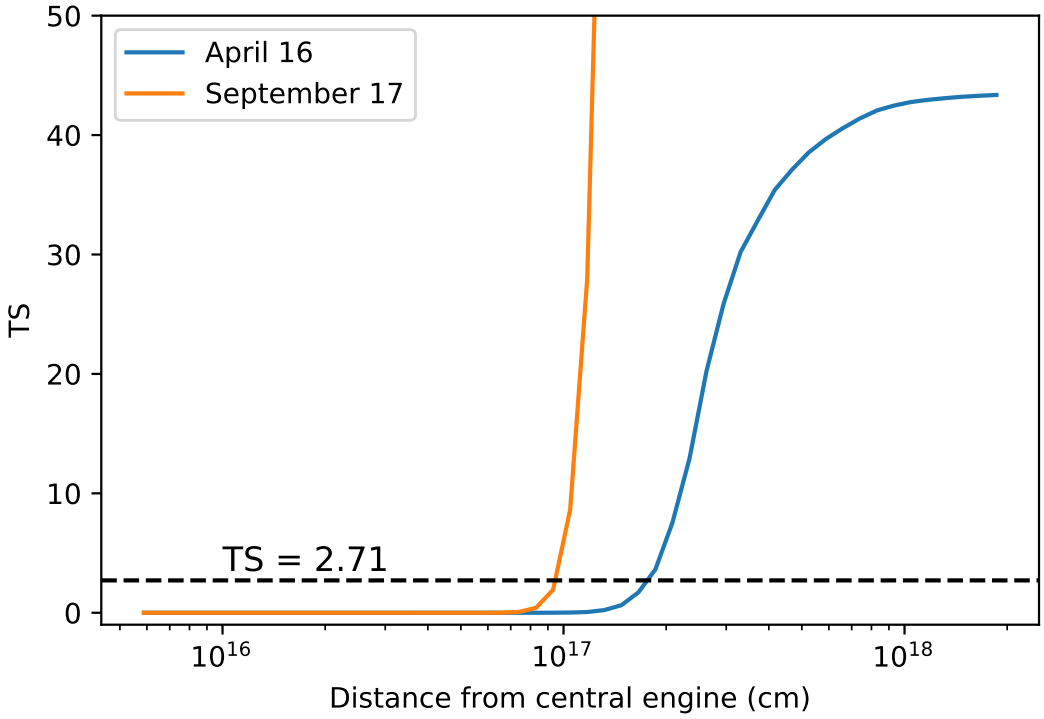

Figure 4.16: Test Statistic obtained with the profile likelihood ratio test as a function of the distance from the central black hole in our absorption by BLR photons hypothesis for the April 2016 and September 2017 flare. The dashed line correspond to the 95% probability limit on the parameter space of the hypothesis. Here the function is monotonous so only an upper limit on the value of r is derived.

in the BLR if the emission region is closer to the central black hole than several hundreds of gravitational radii.

4.5 The extragalactic Round Up

The Round Up is a service task in the H.E.S.S. collaboration. The Round Up consists in a semi-automatic analysis of all the extragalactic observations taken by H.E.S.S. excluding very sensitive datasets. As the responsible of this task for more than two years, I had to maintain the dedicated software, perform the analysis and regularly present the results to the collaboration. The analysis is performed once a month on the most recent calibrated observation period.

The goals of the Round Up are to:

- Give an overview of the recent observations.
- Identify observations with an excess at the source position.
- Search for variability on source and in the field of view.

- Guaranty the analysis of datasets of a priori low interest.

- Find issues with the data acquisition or calibration.

The first step in performing a Round Up is creating a list of all extragalactic observation runs from the previous period. Then apply the run quality selection cuts to obtain two lists : one for the mono analysis and one for the combined3 analysis. Combined3 is an analysis profile combining the events using for each event the reconstruction with the best likelihood between a mono reconstruction with CT5, a stereo reconstruction with CT1-5, or a stereo reconstruction with CT1-4.

The Round Up graphical interface takes the run lists as input to submit the job to perform an analysis of each run individually. It is also able to check which run failed and re-submit the associated jobs.

Once all runs are successfully analysed, the merging by source needs to be performed. To do so, the software makes use of the python module `scikit-learn`[13] to cluster the runs based on the source name and observation direction. The merging of each cluster is then performed giving a results file for each source and analysis profile. The results files are usual Paris Analysis results files which can be explored manually, but the Round Up GUI can be used to create (and save) a variety of plots including excess and significance maps, acceptance maps, excess vs time graphics, ... It also provides basic informations such as livetime and total source significance.

Afterwards, a secondary analysis can be performed aiming at identifying variability and transient hotspots in the field of view. This makes use of a different approach to the usual ON/OFF technique. Here the ON region and the OFF region are taken at the same position but at different times. For a given position covered by N observation runs, the ON-OFF test [120][121] will iteratively consider each run as the ON run and the remaining N-1 runs as OFF runs. The significance of the variation of the ON run away from a stationary state is obtained using the equation 17 in Li&Ma [75] with N_{ON} the number of events at the tested position in the ON run, N_{OFF} the number of events at the tested position in the OFF runs and α the ratio of integrated acceptance at the tested position in the ON run over the integrated acceptance at the tested position in the OFF runs. If the tested position is not variable in time, the distribution of significance obtained should be centred on zero with a symmetric Gaussian dispersion. If variability occurred at the position instead, the run with an excess flux will be characterised by a larger positive significance. Thus, in order to search for transients, maps are created by taking the maximum significance observed at each position during the ON-OFF test. An example of such a map is shown on the left of Figure 4.17. In order to not overestimate the significance of the excess observed, the map needs to be corrected for the trial factor. Indeed, the esperance of encountering a random fluctuation with probability p over N measurement is N$\times p$. The useful map to search for transient is thus the post trial ON-OFF test map such as the right of Figure 4.17.

The Round Up I performed covered 28 lunar periods for a total of around 1500 runs per profile. Over this time, no serendipitous transients are found in the field of view. Variability feature from the observed sources were reported on multiple occasions. The Round Up also served as the only analysis of ToO observations on PKS 0346-27 for which the flux at high energy,which high state was at the origin of the H.E.S.S. trigger, quickly reduced, and no signal was detected in the real time analysis on site. Additionally the sky was hazy the following nights, preventing ToO observations. It allowed to check that these runs contained no exploitable signal.

[13] https://scikit-learn.org/

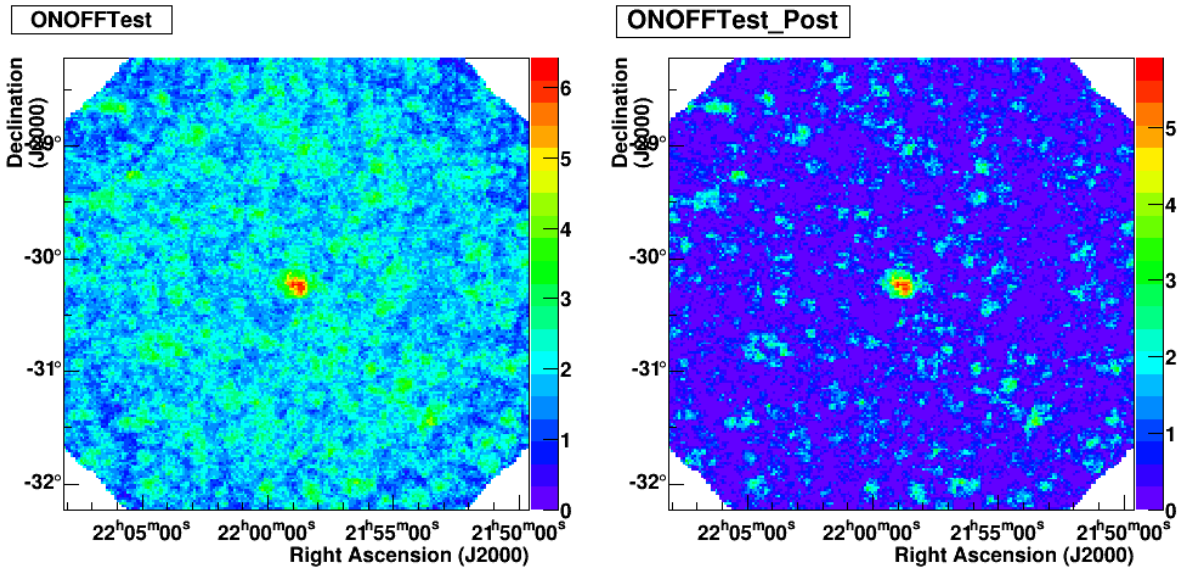

Figure 4.17: ON-OFF test significance maps created using 26 runs taken on PKS 2155-304 in a single observation period with H.E.S.S. The runs were taken before the full moon of September 2018 in the context of the monitoring program of the source [25][122]. The observation strategy consisted in performing one to two observation runs per night when possible, except during the night of the high state seen by the real time analysis in the first runs, when additional runs were taken. *left* : before trial correction. *right* : after trial correction. A significant variability is visible at the center of the map corresponding to the position of PKS 2155-304. No significant variability is observed elsewhere in the field of view.

The flare being globally unremarkable and the H.E.S.S. observation confirmed to contain no excess, no dedicated task force were created for this dataset.

Chapter 5

Characterisation of AGN flares

Sommaire

5.1 Goals

A task was recently started in H.E.S.S. aiming at characterising the temporal structure of all prominent flares detected in AGN at very high energy with H.E.S.S. Making use of common indicators such as the doubling time scale, the goal is to derive constraints on the acceleration and cooling mechanism as well as the emission region size for a small population of flaring AGN. This will allow to create a compilation of AGN flares analysed with the same software and calibration version and displayed in a common format. Inherently common properties will be highlighted and separated from properties changing from flare to flare. In a second step, flares with particularly high quality will be studied in more details. For example, spectral variability will be investigated. More sophisticated analysis such as the search for energy dependent time-lags will also be considered. Energy dependent time lags can be associated with acceleration and cooling in the emission region, or with Lorentz invariance violation[1] during the propagation of photons.

5.2 Procedure

The first and ongoing step of the work to be performed is the analysis of all selected flares with common settings. Since the telescopes evolved during the experiment, three analysis configurations are selected for :

- Flares observed before the installation of the fifth H.E.S.S. telescope
- Flares observed with CT5 but before the upgrade of the HESS1 cameras
- Flares observed after the upgrade of the HESS1 cameras

For each flare, a spectrum and light curves will be produced. The light curves will be produced with nightly, run wise, 4 minutes and 1 minute binning when possible. If the statistics is high enough, a light curve with an adaptive binning will also be created using the method described in section 3.2.

Then, the light curves will be studied systematically using basic indicators and more complex analysis when possible. Among the indicators currently considered are the variability amplitude, flux-doubling time, rise-time, fall-time and duration of the flare. Some of these quantities are computed over the full flare while others use the individual flux points. Quite often, the usual definitions tends to assume a fixed time binning incompatible with the adaptive light curve creations. I consequently tested, and if needed adapted, some indicators for this purpose in section 5.3.

The third step will be the exploitation of available multi-wavelength data with potentially cross-correlation study and search for a time lag compared to VHE.

Finally, all of the above will be combined to derive physical constraints.

[1] A quantity is said Lorentz invariant if it is not modified by a Lorentz transformation. The current theory of relativity is based on the assumption that Lorentz invariant quantities exist including in particular a maximum velocity for any object in the Universe, at which any massless object travel in the vacuum. Lorentz invariance violation generally concerns any deviation from Lorentz invariance. Some theories predict a violation of the Lorentz invariance principle. For example some quantum gravity theories predict a modification of the dispersion relation of photons (e.g. [123]) leading to a dependence of the speed of light on its energy. In this case, the travel time of high energy photons would be different to the travel time of low energy photons.

5.3 Tools for non uniform time binning

5.3.1 Normalised excess variance

5.3.1.1 Computation of σ^2_{NXV}

The normalised excess variance σ^2_{NXV} is a measure of the difference between the observed variation of a light curve and the expected variations based on pure statistical fluctuations, normalised by the global flux average μ and number of points N. It is defined as [124]:

$$\sigma^2_{NXV} = \frac{1}{N\mu^2}\sum_{i=1}^{N}(x_i-\mu)^2 - \sigma_i^2 \tag{5.1}$$

where the x_i and σ_i are respectively the flux and error of the point i. In application, σ_i is divided into an upper and a lower error. I thus used the lower error if $x_i > \mu$, the upper error if $x_i < \mu$ and the average error if $x_i = \mu$.

σ^2_{NXV} should be close to zero if the fluctuations of the lightcurve are purely statistical and positive if the average variations are larger than the statistical errors. If the errors are wrongly estimated, σ^2_{NXV} will also be non-zero and positive if errors are underestimated or negative if errors are overestimated.

A simple modification of the normalised excess variance allows to account for variable time binning. Indeed it is quite simple to see that $1/N$ is equivalent to a normalisation by the duration of observation. Additionally, shorter points are less representative of the global difference to the average compared to point integrating a large duration. The point wise excess variance will thus be weighted by the duration of the point.

$$\sigma^2_{NXV} = \frac{1}{T\mu^2}\sum_{i=1}^{N} t_i\{(x_i-\mu)^2 - \sigma_i^2\} \tag{5.2}$$

where the t_i is the duration of the point i and $T = \sum t_i$ is the duration over which the normalised excess variance is computed.

The error on σ^2_{NXV} for large N is $s/(\mu^2 N^{0.5})$ [124][2] where s is the variance of $(x_i-\mu)^2 - \sigma_i^2$:

$$s^2 = \frac{1}{N-1}\sum_{i=1}^{N}\{[(x_i-\mu)^2 - \sigma_i^2] - \sigma^2_{NXV}\mu^2\}^2 \tag{5.3}$$

Replacing by the weighted variance:

$$s^2 = \frac{1}{T-1}\sum_{i=1}^{N} t_i\{[(x_i-\mu)^2 - \sigma_i^2] - \sigma^2_{NXV}\mu^2\}^2 \tag{5.4}$$

It was previously noted [126] that σ^2_{NXV} can depend on the observation length as long term variability can lead to large deviation from the average. It is thus ill suited to compare flares of vastly different length. It will be possible to compare the normalised excess variance depending on the used binning. Indeed it should increase if the binning becomes short enough to resolve otherwise averaged variability features. The normalised excess variance can also be computed day by day and run by run. This would allow to see if the source variability evolved during the flare, and to compare same length periods between flares.

[2] The formula for s in this reference had a typo, the correct formula can be found in [125].

5.3.1.2 Tests on intense flares

This is tested on three datasets. The first is one the most intense flares of PKS 2155-304 observed for three full observation runs early of July 28th 2006 [22]. The second is another of the most intense flares of PKS 2155-304 observed for fifteen full observation runs only two days after the previous flare the night between July 29th and 30th 2006 [127]. The final flare I will use in this study is a flare of PKS 1510-089 observed for ten days in May 2016 [128]. Since only two nights contained significant signal, I will limit my analysis to this period.

Following the original publication [22], the light curve for the first flare of PKS 2155-304 is created assuming a broken power law spectrum and using a threshold of 200 GeV. The binning used are run wise, 240 and 60 seconds, and adaptive 5 and 15 sigma per point. The use of 15 sigma per point is possible only for such an exceptional flare.

For the second flare of PKS 2155-304, the energy threshold varied during observation, and the energy threshold of 700 GeV applicable over the full time window will be used with a spectral shape corresponding to a power law with an exponential cut-off as discussed in [127]. The binning used are run wise, 240 and 60 seconds and adaptive 5 and 15 sigma per point.

Once again following the associated publication [128], a power law spectrum and a threshold of 200 GeV will be used for the flare of PKS 1510-089. The binning used are run wise, 240 seconds, and adaptive 5 sigma per point.

All adaptive light curves are created using an under significance threshold point at the end of runs (see 3.2 for explanation). Also, in order to better estimate the background for short binning, OFF events will be integrated over time windows extended by 60 seconds before and after the time interval of sub-run light curve points.

Normalised excess variance of the full flares

For each flare, the normalised excess variance is computed over the full period for each light curves. Results are shown in Table 5.1. For the flare of July 28th from PKS 2155-304, it is quite evident that the normalised excess variance increases when going from a run wise to a minute or seconds scale light curve. This is consistent with the minute scale variability reported at the time. Another increase is seen when using the 5 sigma per point adaptive binning, which often creates points over less than 5 seconds in this case. This hints at even shorter time variability with significant variations over a few seconds as visible on the light curve (see, e.g. a zoom over a period of 200 seconds of the first run in Figure 5.6). In the case of the second flare of PKS 2155-304, the normalised excess variance seems stable with the change of binning. The variability consequently seems to be dominated by a relatively slow variability over the full observation. A small increase is also visible when using the 5 sigma per point adaptive binning, hinting again at shorter time variability. Finally, in the case of the flare of PKS 1510-089, the normalised excess variance is compatible between each binning. This is logical when considering the large flux variation between the two nights included here.

The ~ 200 seconds variability reported for the first flare of PKS 2155-304 was already, by argument of causality, implying problematic limits on the size R and the Doppler factor δ_D of the emission region. Indeed, the variability time scale t_{var} should be limited to the light crossing time of the region at the origin of the emission. In the observer frame it means $R \leq ct_{var}\delta_D/(1+z)$ with c the speed of light and z the redshift of the source. Scaling by the central black hole Schwarzschild radius $R_S = 2GM/c^2$ – a natural minimal scale for R – and using the mass of the black hole and redshift of PKS 2155-304, it was found that [22] $\delta_D \geq 60 - 120R/R_S$. This implies a value of δ_D much greater than the typical ~ 10 derived for blazars. Using the same

argument with a time scale of ~ 10 seconds would imply a Doppler factor or a compacity of the emission region greater by more than an order of magnitude. Explaining such short variability while conserving more reasonable properties of the emission region requires an origin of the variability unrelated to the black hole scale. At this point it is important to remember that the jet is an outflow produced by (relativistic) magneto hydrodynamic (MHD) processes. Detailed MHD simulations show that instabilities develop in jet thus creating non axisymmetric jets (i.e. symmetric around the jet axis) [129] with occurrences of local instabilities such as magnetic line reconnection at the origin of particle acceleration. This magnetic reconnection was invoked as the mechanism at the origin of fast TeV variability in AGN [130]. Using another mechanism, [131] invoked the development of electric field oscillations due to instabilities in the ion plasma near the base of the jet. This effect could be responsible for variability over time scales of hundreds of seconds while keeping a unique extended emission region. A candidate scenario for seconds scale variability is proposed in [132]. In this scenario, most of the broad band emission comes from a usual emission region. Additionally, multiple fine beams of very energetic electrons following moving magnetic field lines are present in the jet. This jet would be responsible for an intense inverse Compton emission with limited synchrotron; and only visible for short durations when the magnetic line aligns with the line of sight. Generally, the fast variability of AGN is attributed to the existence of sub-emission regions with higher densities and/or lorentz factor than the bulk of the jet. The existence of such regions was previously used to model the first flare of PKS 2155-304 [133]. Both MHD simulations and models predict the apparition of such phenomenons.

Normalised excess variance over individual runs

The normalised excess variance is then computed in a run wise manner for each flare and sub-run binning. Figure 5.1 shows for each case the light curve in the bottom panel and the normalised excess variance in the top panel. For the first flare of PKS 2155-304 (Figure 5.1-a,b,c,d), σ_{NXV} is most important in the third run corresponding to the transition between the flaring state and the quiescent state. The first two runs also display positive normalised excess variance incompatible with zero within their errors. All binning show the same behaviour in terms of σ_{NXV} with small variations. One of the most important differences is in the first run for which σ_{NXV} increases for shorter binning, with for example $\sigma^2_{NXV,240s} = 0.049 \pm 0.010$ and $\sigma^2_{NXV,5sig} = 0.082 \pm 0.019$. An increase is also seen in the third run but contained within the larger errors. In the case of the second flare of PKS 2155-304 (Figure 5.1-e,f,g,h), we observe an alternation between some runs with high normalised excess variance and a majority of runs with low or compatible with zero normalised excess variance. This is compatible with the light curve which displays a long term variability and plateaus with some short bursts. A peculiar behaviour is observed for the first run as σ_{NXV} increases significantly when considering the 60 seconds binning. Another thing to note is the general decrease of σ_{NXV} when using the 5 sigma adaptive binning. It is likely that the variability feature dissipates in the increased statistical errors with this short binning. For the flare of PKS 1510-089 (Figure 5.1-i,j), no excess of variability is seen in any run meaning that both light curves are compatible with a fixed flux for each individual run. All the variability is at longer time scales. It also seems that the first run of the second night is overly stable as $\sigma_{NXV} < 0$.

5.3.1.3 Conclusion

The normalised excess variance computation is historically defined over a uniformly binned light curve. I adapted the formula to be generalised for non uniform binning by weighting the contribution of each point by its duration. Tested on 3 flares using light curves with both fixed and adaptive binning, consistent behaviours of the normalised excess variance and the associated error are observed. Satisfying results are also obtained when computing the normalised excess variance on a run wise basis. The implemented computation is valid and will be usable for any non-uniform binning in the future studies. This includes of course light curves with fine binning created with the adaptive binning used here, but also more usual light curves such as night wise with a varying observation length per night.

Flare \ Binning	run	240s	60s	15σ	5σ
PKS 2155-304 : July 28th 2006	0.25 ± 0.01	0.30 ± 0.05	0.31 ± 0.03	0.32 ± 0.02	0.35 ± 0.02
PKS 2155-304 : July 29-30th 2006	0.39 ± 0.13	0.42 ± 0.06	0.41 ± 0.03	0.42 ± 0.04	0.47 ± 0.04
PKS 1510-089 : May 28-30th 2016	0.42 ± 0.18	0.42 ± 0.10	x	x	0.53 ± 0.36

Table 5.1: Normalised excess variance for the full flares of PKS 2155-304 and PKS 1510-089 depending on the light curve binning used.

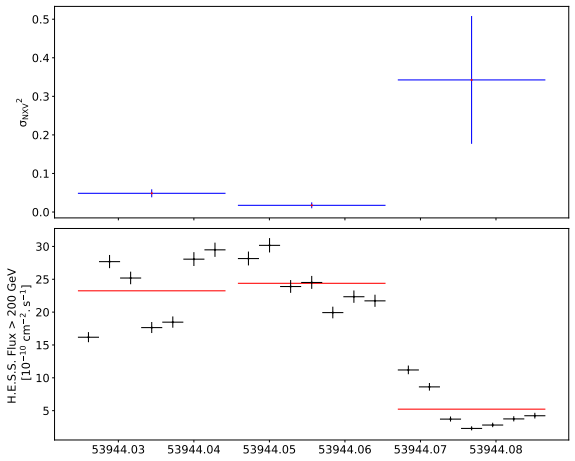

(a) PKS 2155-304 1st flare; 240 seconds binning

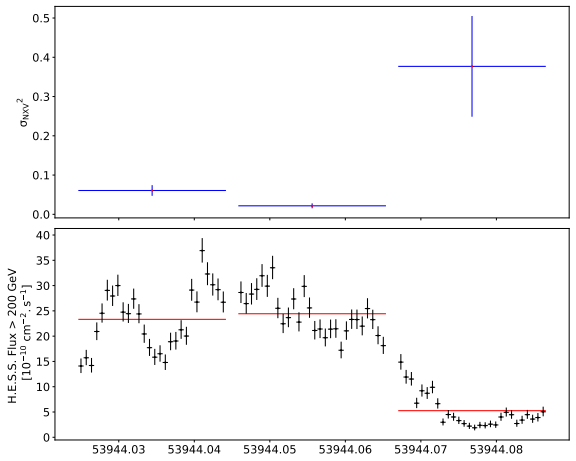

(b) PKS 2155-304 1st flare; 60 seconds binning

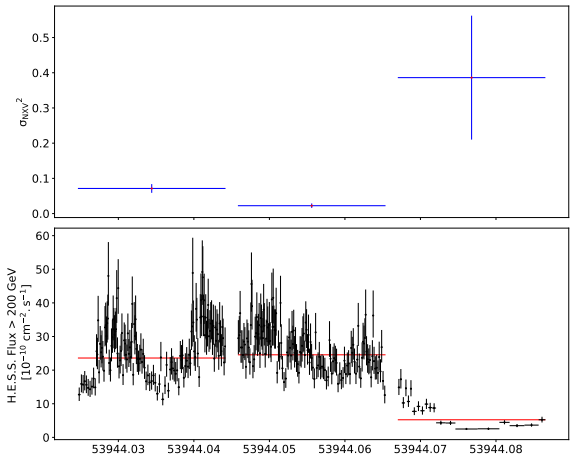

(c) PKS 2155-304 1st flare; 15 sigma binning

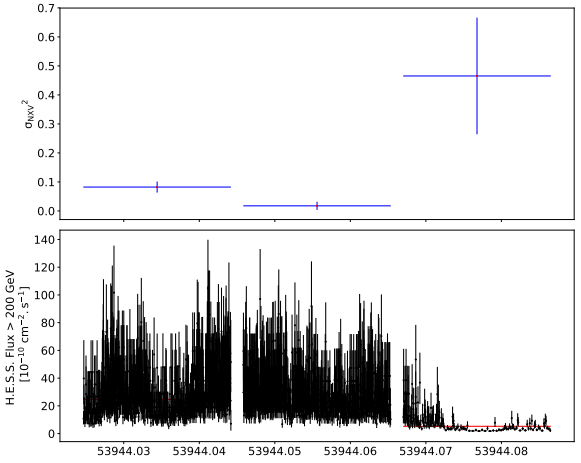

(d) PKS 2155-304 1st flare; 5 sigma binning

Figure 5.1: Light curve (*bottom*) and run wise normalised excess variance (*top*) for all three flares for various binning. Red lines in the light curve represent the run average.

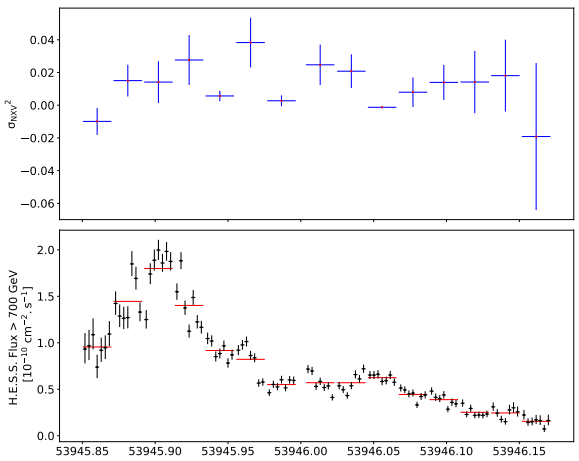

(e) PKS 2155-304 2nd flare; 240 seconds binning

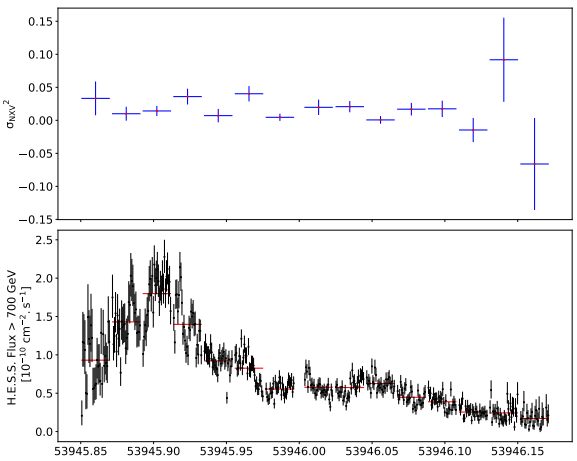

(f) PKS 2155-304 2nd flare; 60 seconds binning

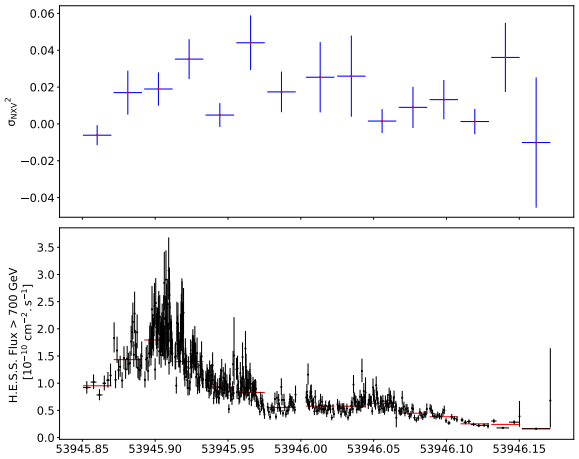

(g) PKS 2155-304 2nd flare; 15 sigma binning

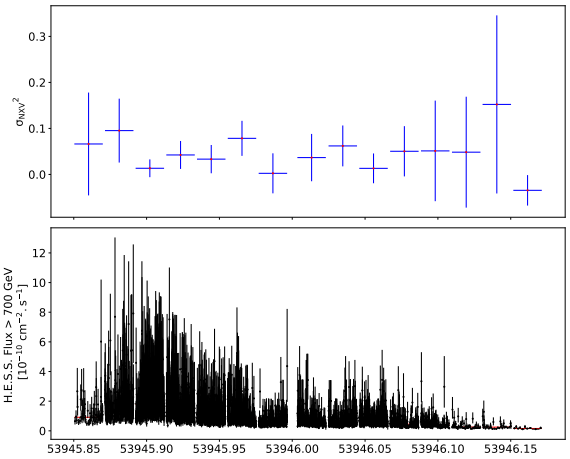

(h) PKS 2155-304 2nd flare; 5 sigma binning

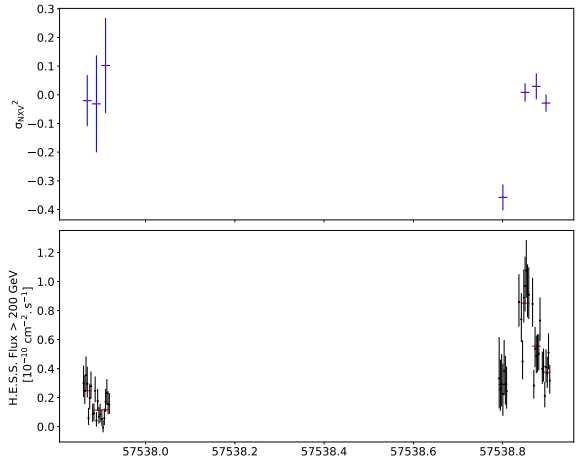

(i) PKS 1510-089 flare; 240 seconds binning

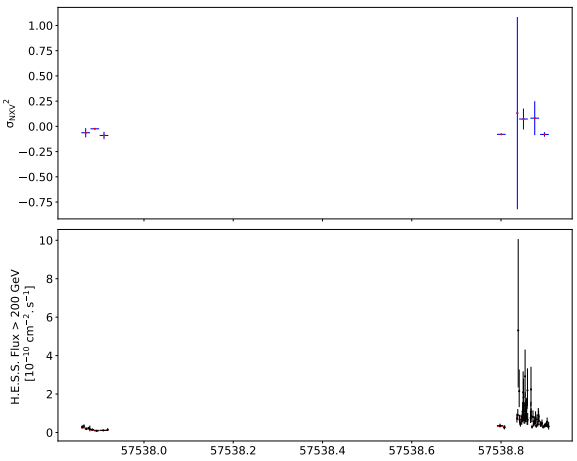

(j) PKS 1510-089 flare; 5 sigma binning

Figure 5.1: Light curve (*bottom*) and run wise normalised excess variance (*top*) for all three flares for various binning. Red lines in the light curve represent the run average. (continued)

5.3.2 Flux doubling time

5.3.2.1 Definition

The flux doubling time T_2 is an estimator of variability time scale often used in astrophysics. It estimates the duration it takes for the flux to double (or get divided by 2) using the evolution rate as between the two points between which it is being evaluated. We will follow the definition of [134] which is used in the publication associated with the flare of PKS 2155-304 of July 28th 2006 [22]. It is evaluated for each pair of point of a light curve and the shorter ones are used as variability time scales of the source. Noting T_i and F_i the time and flux of point i, we can respectively write the difference of flux, of time and the average flux of points i and j as follows :

$$\Delta F_{ij} = F_j - F_i \quad (5.5a) \qquad \Delta T_{ij} = T_j - T_i \quad (5.5b) \qquad F_{ij} = (F_j + F_i)/2 \quad (5.5c)$$

And T_2 evaluated between the point i and j is then :

$$T_{2,ij} = \left| \Delta T_{ij} \frac{F_{ij}}{\Delta F_{ij}} \right| \tag{5.6}$$

The associated error is simply obtained by propagating the error on the individual fluxes. Additionally, an error on the time of the light curve point will be taken into account as $1/\sqrt{12}$ times the duration of the bin[3]. Using δ as the symbol meaning "error on" we have :

$$2 \times \delta F_{ij} = \delta \Delta F_{ij} = \sqrt{\delta F_j{}^2 + \delta F_i{}^2} \text{ and } \delta \Delta T_{ij} = \sqrt{\delta T_j{}^2 + \delta T_i{}^2} \tag{5.7}$$

And :

$$\left(\frac{\delta T_{2,ij}}{T_{2,ij}} \right)^2 = \left(\frac{\delta F_{ij}}{F_{ij}} \right)^2 + \left(\frac{\delta \Delta F_{ij}}{\Delta F_{ij}} \right)^2 + \left(\frac{\delta \Delta T_{ij}}{\Delta T_{ij}} \right)^2 \tag{5.8}$$

Contrary to the normalised excess variance, the doubling time doesn't depend on a regular binning and can be applied directly to the light curve with adaptive binning. In the following we will see if shorter T_2 can be extracted thanks to the shorter binning at high flux.

In order to keep only meaningful estimates, it is mandatory to pre-select the T_2 by applying a cut on the relative error. For a given dataset, a shorter binning induces larger errors on the individual points. This leads to larger errors on the associated T_2.

5.3.2.2 Application to AGN flares

The extraction of the flux doubling time is applied to a selection of the light curves used in subsubsection 5.3.1.2 and they will be described using the same terminology. In the following, the doubling times will be separated between T_2^+ corresponding to an increase in flux and T_2^- corresponding to a decrease in flux. The binning and maximum relative error used will also be displayed as a subscript, e.g. for the increasing doubling time scale obtained with a 60 seconds bin light curve, allowing an error of 30% on T_2 : $T^+_{2,60s,30\%}$.

A published value of T_2 is available for the flare of PKS 2155-304 of July 28th 2006 [22]. The fastest T_2 reported using a 60 seconds bin light curve and a maximum relative error of 30% is 224 ± 60 s. The average of the 5 fastest T_2 is also given as 330 ± 40 s. The first light curve to be tested here will thus be the equivalent one obtained with the new analysis. We have $T^+_{2,60s,30\%} = 226 \pm 54$ s and the average of the five fastest is 314 ± 28 s. This is fully compatible

[3] Corresponding to one standard deviation for a uniform distribution.

with the previous estimation. The associated distribution of doubling times coloured by relative error is shown in Figure 5.2. We can in particular note that increasing the required precision to 20% means a fastest $T^{+}_{2,60s,20\%} = 263 \pm 47$ s; and lowering the precision to 40% means a fastest $T^{+}_{2,60s,40\%} = 157 \pm 54$ s. Shorter times are obtained for the decreasing flux T_2. The fastest decrease time scale is $T^{-}_{2,60s,30\%} = 112 \pm 25$ s.

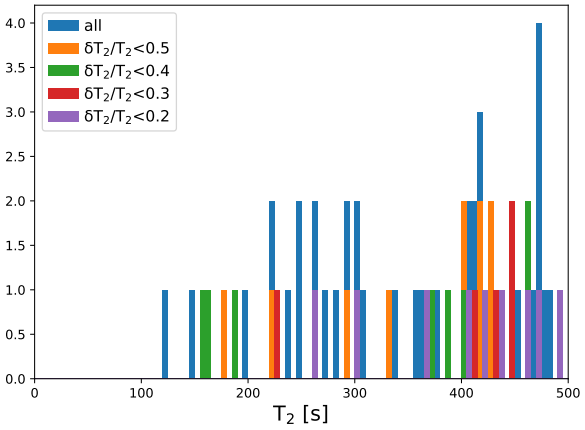

Figure 5.2: Increase doubling time distribution for the first flare of PKS 2155-304 using light curve with 60 seconds bins. Colours correspond to different relative errors.

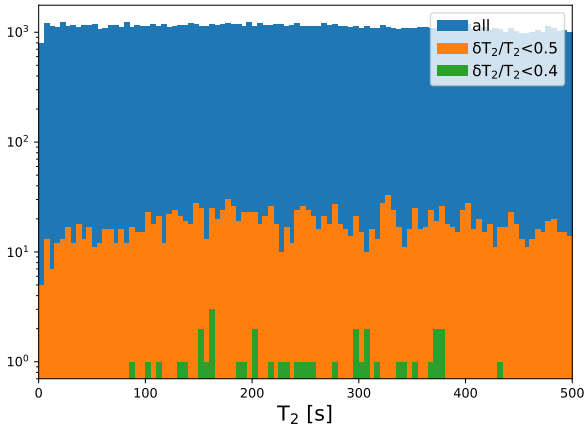

Figure 5.3: Increase doubling time distribution for the first flare of PKS 2155-304 using light curve with 5 sigma adaptive bins. Colours correspond to different relative errors.

When creating a light curve, the shorter the integration time used, the larger the relative errors on the flux will be. Consequently, the relative errors on the associated T_2 will also be larger. When using a 5 sigma per point limit on the first flare of PKS 2155-304, this means that no T_2 are extracted with an error of less than 30% as shown in Figure 5.3. In this case, we can use 40% and $T^{+}_{2,5sig,40\%} = 86 \pm 34$ s with an average of the 5 fastest of 114 ± 20 s. These durations are consistent with the 2 fastest rising time of the asymmetric gaussians used to model the flare : 67 ± 47 s and 116 ± 53 s. T_2 of the order of seconds are also seen with e.g, $T^{+}_{2,5sig,50\%} = 2.2 \pm 0.9$ s which justifies the increase of excess variance in the previous part and corresponds to observable features on the light curve as shown in Figure 5.6. As discussed in the section on σ_{NXS}, arguments of causality makes explaining the short time scales seen here by a change of the full emission region impossible but existing model can account for them. Using 15 sigma per point, $T^{+}_{2,15sig,40\%} = 26 \pm 10$ s with an average of the 5 fastest of 39 ± 6 s. This means that the increase in precision on the light curve points here allows to resolve shorter variability than the finer binning before. We can also use a better constraint on T_2 to compare with the 60 seconds binning : $T^{+}_{2,15sig,30\%} = 252 \pm 73$ s with an average of the 5 fastest of 285 ± 37 s which is close to the values obtained with the 60 seconds binning.

Looking at the weaker flare of PKS 1510-089, longer bins are produced by the adaptive binning method. The available fixed binning is also longer. In this case $T^{+}_{2,240s,30\%} = 39706 \pm 11671$ s $= 0.46 \pm 0.13$ day. This is representative of the more than quadrupling in flux between the lowest state of the first night and the highest state of the second night. As seen on the distribution of T_2^{+} in Figure 5.4, authorising 40% errors shows a shorter time scale $T^{+}_{2,240s,30\%} = 2994 \pm 1175$ s with an average of the 5 fastest of 3422 ± 600 s, close to an hour. Using a 5 sigma per point adaptive binning, similar time scales are dominating the distribution of positive doubling times but with way worse errors as seen in Figure 5.5.

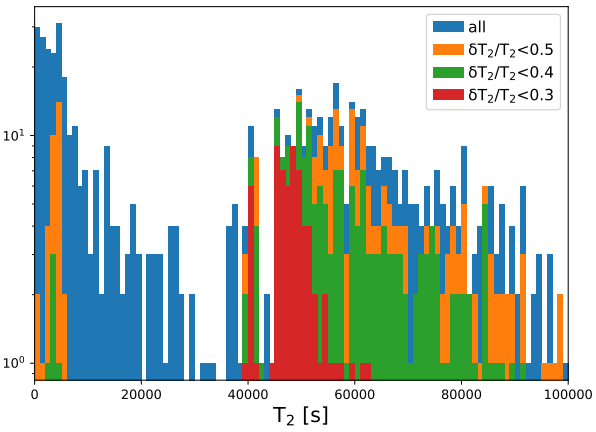

Figure 5.4: Increase doubling time distribution for the first flare of PKS 1510-089 using light curve with 240 seconds bins. Colours correspond to different relative errors.

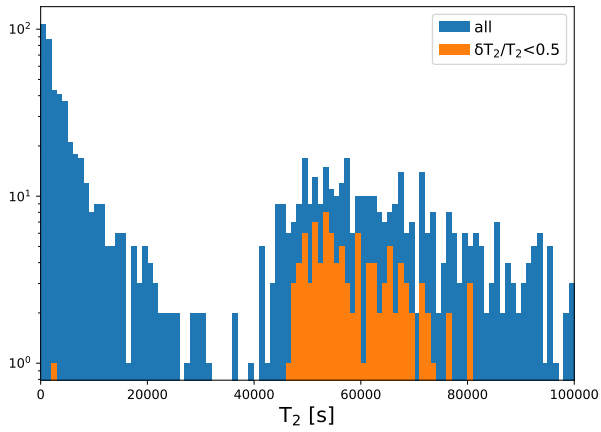

Figure 5.5: Increase doubling time distribution for the first flare of PKS 1510-089 using light curve with 5 sigma adaptive bins. Colours correspond to different relative errors.

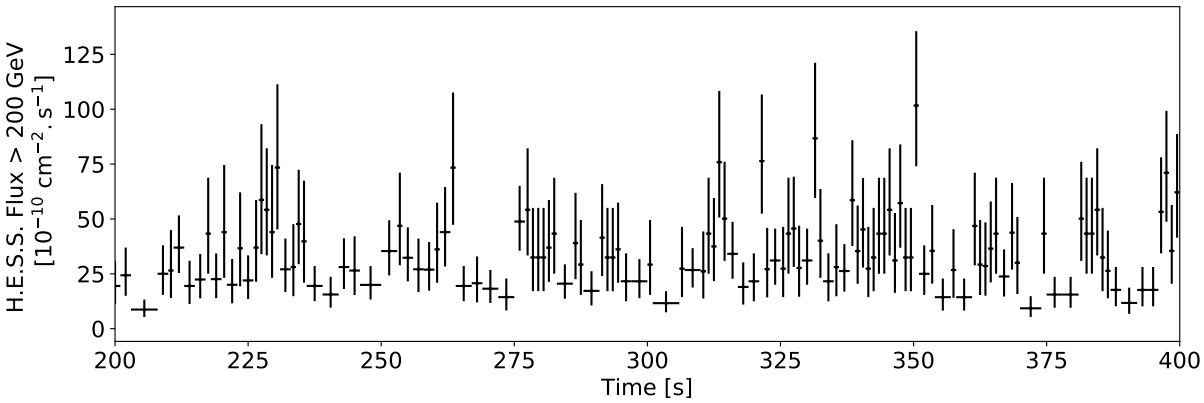

Figure 5.6: Zoom on the light curve of the first flare of PKS 2155-304 created with an adaptive binning with 5 sigma per point. Variability over seconds is clearly visible. Times are given relative to the start of the flare observations.

5.3.2.3 Conclusion

Extracting doubling time scales from adaptively binned light curves leads to an extraction of time scales consistent with the ones obtained with a fixed binning, as was expected. A caveat comes from the increased relative error on the flux appearing when reducing the duration of light curves bins. Since the doubling times are computed only using a pair of points, it doesn't gain precision by having access to more data while it loses precision due to the errors on the points. One thus needs to be conservative when creating a light curve with adaptive binning in order to guaranty a certain precision of the T_2 estimator. If this is done, doubling time scales can naturally be extracted using an adaptive binning. While the errors do increase when considering very short binning, the associated time scales are indeed found in the light curve. The multiplicity of occurrence of a given time scale is also important here but difficult to account for precisely as the doubling times are correlated.

Chapter 6

Lepto-hadronic model : expected neutrinos from TXS 0506+056

Sommaire

The blazar jet physics remains mysterious with a wide variety of temporal and spectral behaviours from one object to the other but also for a single object observed at different times. This was illustrated in the previous chapters with ,e.g., the flares of 3C 279 displaying a short, one night flare and a multiple day flare and a large variety of multi-wavelength correlation. Among the pending questions, the role of hadrons in the high energy photon bump emission is of high importance since the presence of highly energetic hadrons induces important effects and constraints on the jet energetic, acceleration, geometry, ... Indeed, the high mass of the proton compared to the electron means that it will carry a significantly higher quantity of energy in the jet; that it will require larger confinement region; and that it will loose less energy than electrons. Most blazars SED are well reproduced by both leptonic and lepto-hadronic models which makes favouring one or the other very complex.

In recent years, the improvement of astrophysical neutrino observation techniques led to a new interest in lepto-hadronic models as meson decay produces neutrinos. Since leptonic processes yield no neutrinos, a significant association of blazars with an astrophysical neutrino excess would guaranty a hadronic origin of the high energy photon emissions in the jet. Additionally, simultaneous photon and neutrino flux measurements could add constraints to the generally degenerate solution of emission models. I previously performed a study aiming at assessing the potential neutrino spectrum expected from a blazar, PG 1553+113, in a non-flaring state [135]. This work was performed using the code LeHa, a one-zone lepto-hadronic model developped by Matteo Cerruti [136] [137]. Results included a wide variety of solution divided into two families characterised by the origin of the high energy photon bump : synchrotron from primary protons or emission by secondary leptons plus electron synchrotron self Compton (SSC). It was shown that the peak of neutrino emissions is expected at energies above the IceCube optimal sensitivity. Proton synchrotron solution for PG 1553+113 always included neutrino fluxes below the 4 years IceCube sensitivity to point-like sources. Oppositely, in the case when emission from secondaries is important the neutrino flux could be above the 4 years IceCube sensitivity to point-like sources which can thus constraint the model parameter space. Example modelling showing these properties are displayed in Figure 6.1.

In September 2017, IceCube detected a high energy neutrino : IceCube-170922A, as a muon type track event. IceCube events are divided into three main categories : muon type track events from ν_μ, cascade events from ν_e and double bang events from ν_τ. Cascade events deposit energy in a localised region of the detector where the neutrino interacts. The wide and localised morphology of the signal leads to direction errors of the order of 10 to 20 degrees. Double bang events are similar but with two regions : one where the neutrino interacts and one where the tau decays. Muon type track events deposit energy in a track over a long distance following the secondary muon trajectory. The arrival direction of a muon type track event can thus be reconstructed with a good precision, in this case 90% containment errors of less than 1° which is usual for such events. IceCube-170922A arrived from a direction located at 0.1° from the blazar TXS 0506+056. MWL observation at HE by *Fermi*-LAT and VHE by MAGIC showed an elevated state of TXS 0506+056 at the time, leading to a temporal and spatial coincidence with a chance correlation rejected at the 3σ level [36]. Following this association, we performed an extensive exploration of the parameter space of the one-zone lepto-hadronic model from the LeHa code applied to the high state of TXS 0506+056. The goal being to estimate the associated neutrino flux and detection probability. This work will be described in details in this chapter, and was published in the Monthly Notices of the Royal Astronomical Society Letters [33].

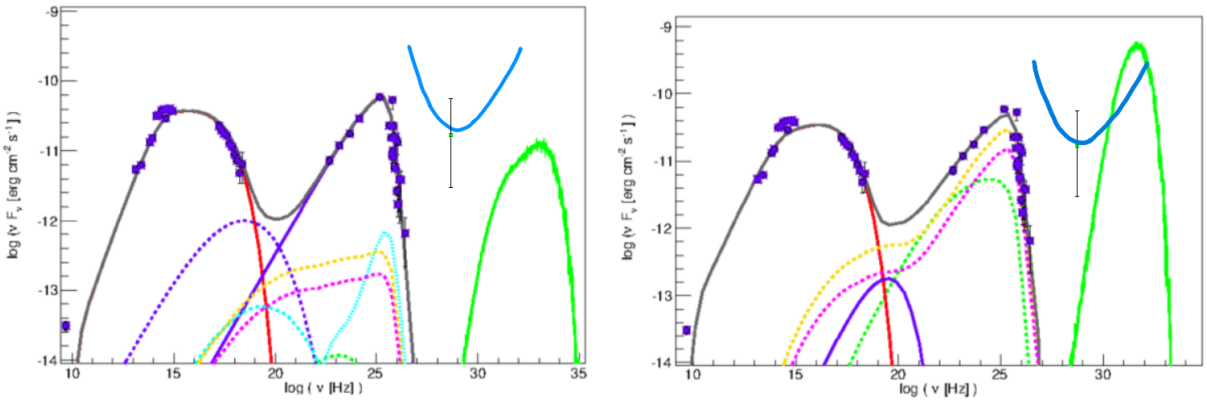

Figure 6.1: Modelling of the low state of PG 1553+113 SED using a lepto-hadronic model. Purple points are a compilation of electromagnetic data on which the model is adjusted. The green point at $\sim 10^{28-29}$ Hz is a neutrino (N-17) reconstructed at 8.9° from PG1553+113, compatible within the large neutrino direction errors typical for cascade events. The cyan solid line is the 4-years IceCube sensitivity. Synchrotron emission from primary electrons is shown with the red solid line; synchrotron emission from primary protons is shown with the purple solid line; synchrotron-self-Compton emission is shown with the green dashed line; synchrotron emission by muons is shown with the dotted light-blue line; synchrotron emission by cascades triggered by π^0 decay, $\pi^{\pm}$ decay, proton synchrotron and muon synchrotron are shown with the violet, yellow, purple and light-blue dashed lines, respectively. Finally the neutrino total flux is shown as a solid green line. *left :* Model with a dominant proton synchrotron contribution at high energy. *right :* Model with a dominant pion cascade contribution at high energy. From [135].

6.1 The model

The model in the LeHa code is a stationary, one zone, lepto-hadronic model. It considers a single spherical emitting region in a relativistic jet. This emitting region is characterised by a radius R, a Doppler factor δ_D with respect to the observer, and is filled by a plasma of leptons and hadrons subjected to a uniform magnetic field B. The primary lepton population is considered to be only composed of electrons and positrons and the hadrons are assumed to be protons. Both populations energy distributions are parametrised as broken power-laws with an exponential cut-off, with the break coming from cooling of the injected particles. No acceleration processes are included in the code as source of the emitting particles. A broken power law takes 6 parameters : the minimum, maximum and break energies (respectively corresponding to the Lorentz factors γ_{min}, γ_{break}, γ_{max}); the indexes before (α_1) and after the break (α_2); and the global normalisation K. In total the LeHa codes requires 15 parameters : δ_D, B, R, $\gamma_{e,min}$, $\gamma_{e,break}$, $\gamma_{e,max}$, $\alpha_{e,1}$, $\alpha_{e,2}$, K_e, $\gamma_{p,min}$, $\gamma_{p,break}$, $\gamma_{p,max}$, $\alpha_{p,1}$, $\alpha_{p,2}$ and K_p.

The code simulates both leptonic and hadronic interactions (see subsection 1.2.1.1 and 1.2.1.2). A synchrotron self Compton (SSC) scenario is assumed for the inverse Compton interaction of the primary electrons, meaning that no external photon fields are considered. While this is the expected behaviour for BL Lac objects [138], such as TXS 0506+056, external target fields are expected in the case of FSRQ. For the hadronic part, the code simulates proton-photon interactions by making use of the Monte-Carlo code SOPHIA [32] for the photo-meson interactions. Bethe-Heitler pair production is also implemented using an analytical computation [139]. The photon fields used in proton-photon and photon-photon interactions in the LeHa code are the synchrotron photons from the primary electrons and positrons and SSC photons.

The leptonic processes from the primary electrons can be computed directly and very quickly. The hadronic part of the code is way more computationally expensive with the required simulations and the complex integration used for the Bethe-Heitler process.

6.2 IceCube-170922A association to TXS 0506+056

6.2.1 The data

Our model will be compared to multi-wavelength data acquired within 14 days of the detection of the IceCube-170922A event on September 22nd 2017 at 20:54:30.43 Coordinated Universal Time (UTC). Data points are taken from the neutrino association paper [36] limiting the optical data to the strictly simultaneous Swift-UVOT points since additional data over the same energy band is not useful for the modelling. Thanks to the extensive MWL observation campaign started after the neutrino detection, TXS 0506+056 was detected in radio, optical, X-rays, and at high and very high energy during this period. A very good coverage of the transition between the low and high energy component of the TXS 0506+056 SED is achieved in X-rays by the combination of Swift-XRT and NuSTAR observations. The high energy points are obtained with *Fermi*-LAT and the VHE are covered by the MAGIC detection. Initial observations by H.E.S.S. and VERITAS on September 23rd, and MAGIC on September 24th, following the neutrino alert led to no detection for each instrument. After reports by *Fermi*-LAT of an elevated state of TXS 0506+056 starting in April 2017, and of an ongoing flare, MAGIC performed additional observations between September 28th and October 4th leading to a detection.

While the data used here come from a variable source, the use of a stationary model is justified since TXS 0506+056 was detected in an elevated state during a long, six months, period at HE by *Fermi*-LAT and because we are interested in a single neutrino detection. Thus, no temporal information about the neutrino flux is available and the actual SED of the source can be expected to be on average relatively close to the one used in the present modelling.

Radio emission is generally expected to originate from a large region with relatively low photon density as the contrary would imply a strong suppression of the flux by the synchrotron self absorption effect. Due to the high radiation density in the emission region in our model, it cannot account for radio emissions which thus originate from a separate region of the jet.

6.2.2 The simulation

In order to reduce the parameter space to be explored, physically motivated a-priori assumptions were applied :

- We assume that the electrons and protons are accelerated by a common mechanism and are consequently injected with particles populations characterised by the same spectral index α_1 which will be the index before the break of both broken power laws.

- The dominating cooling process for electrons is synchrotron losses. As a consequence the electron distribution after the break at $\gamma_{e,break}$ is characterised by a spectral index $\alpha_{e,2} = \alpha_1 + 1$, and $\gamma_{e,break}$ is obtained by equating the synchrotron and synchrotron self Compton cooling time scale τ_c and the addiabatic cooling time scale $\tau_{add} = 2R/c$ [137].

$$\tau_c(\gamma_e) = \frac{3m_e c}{4(u_B + u_{soft})\sigma_T \gamma_e} \tag{6.1}$$

where u_B is the magnetic field energy density, u_{soft} the synchrotron photon energy and σ_T the Thomson cross-section.

- The minimum energy of both protons and electrons have little impact on the models as long as it remains relatively small. However, in order to accommodate for radio data, the minimum electrons energy cannot be arbitrarily low. We consequently fixed $\gamma_{p,min} = 1$ and $\gamma_{e,min} = 500$. The existence of a minimum energy to the particle distribution is associated to the efficiency of the acceleration mechanism versus the energy loss rate as a function of energy. Most models of acceleration have a minimum energy below which the energy loss rate is higher than the acceleration rate implying that particles can't be accelerated from below this energy and lower energy particles are decelerated.

- We consider a proton population subjected to limited cooling. To do so, the maximum proton Lorentz factor $\gamma_{p,max}$ is calculated by equating the acceleration time scale, $\tau_{acc} = \eta \frac{m_p c}{eB} \gamma_p$, and the shortest energy losses time scale for the protons. As a consequence, proton energy losses are limited and the proton population distribution is considered to be a simple power law instead of a broken power law. Additionally, the value $\gamma_{p,max}$ is directly linked to η, the efficiency factor of the acceleration mechanism.

- MAGIC observed a variability time scale τ_{obs} of the order of one day. It can be used to constrain the size of the emission region by argument of causality : $R \leq \frac{\delta_D \tau_{obs}}{1+z} = R_{max}$

The remaining parameters are B, δ_D, R, K_e, K_p, $\gamma_{e,max}$, α_1 and η. During each modelling, K_e and $\gamma_{e,max}$ will be constrained by fitting the low energy component in the SED ignoring the radio band. For the high energy component, two scenarios similar to the ones observed in my previous work on PG 1553+113 were studied. The first is the family of solutions for which the proton synchrotron dominates the high energy component. The second considers a combination of SSC and hadronic cascade emissions. In both cases, the exploration of the parameter space was performed in two steps. First, general constraints and properties of the solutions are obtained by exploring the parameter space by-hand and using previous knowledge and external informations. Then an automatic scan is performed over the reduced parameter space. During the automatic scan, the χ^2 with respect to the data is computed a posteriori for each model. From the χ^2 distribution, the best fit model is chosen as the solution with the lowest χ^2 and all models characterised by $|\Delta\chi^2| \leq 1\sigma$ are selected as possible solutions.

During the modelling, the neutrino spectra for each flavour of (anti-)neutrinos is extracted and propagated to the observer frame along with the electromagnetic spectrum. Since neutrinos oscillate we make the hypothesis of a uniform probability of observing each flavour of 1/3. We are here mostly interested in the muon neutrinos as IceCube-170922A was reconstructed with this flavour. The predicted observable spectrum obtained from each model will be the sum of the propagated ν_e and ν_μ spectra [1] produced during the charged pion decay divided by 3. In order to extract muon neutrino detection rates, I implemented in the LeHa code the convolution of the neutrino spectra obtained from the modelling with the effective areas for the IceCube EHE trigger [36] and the IceCube point-source search (PS) [140]. The EHE sensitivity corresponds

[1] No ν_τ are produced in the source

to the full sky search which originally detected IceCube-170922A. The PS sensitivity is a more sensitive search, performed a posteriori in the direction of TXS 0506+056, which did not yield any detection of additional neutrinos in the studied time period.

6.2.3 Proton synchrotron solutions

In this first model family, the peak of the high energy component of the SED is ascribed to synchrotron from the primary protons. For a given value of δ_D the observed high energy peak is in this case directly related to $\gamma_{p,max}$ and consequently to η. Following [137] we first fixed $\eta = 10$. With this choice, adjusting the energy of the peak of the proton synchrotron emission requires dense emission regions. The issue is then that a large contribution from the electromagnetic cascades initiated by the pion decay arises in this case thus over-predicting the VHE and hard X-ray emission. Proton synchrotron solutions require a higher value of η, meaning a lower efficiency of the acceleration process. For a given value of δ_D, α_1 and η, the condition on the cooling of the protons can be translated into an upper limit on the peak frequency of the proton synchrotron : $\nu_{peak,p} \leq \nu_{max}$. Since $\nu_{peak,p}$ is monotonously evolving with the magnetic field, the scan of the magnetic fields dimension will be converted into a scan over values of $\nu_{peak,p} \leq \nu_{max}$ during the parameter scan.

The high energy component is also strongly constrained at the transition from the low energy component by data in X-rays from Swift-XRT and NuSTAR. Since the emission from cascades covers a broad energy spectra, adjusting the NuSTAR data with cascade emissions always overproduces the VHE part of the spectrum in the model. The solution is to have the proton synchrotron dominating the whole SED from NuSTAR to the high energy peak. This strongly constrains the primary particle distribution properties by fixing the injection index to $\alpha_1 = 2.0$. In the area of the parameter space that will be explored in this scenario, the electrons will be in the fast-cooling regime implying that they are fully cooled and $\gamma_{e,break} = \gamma_{e,min}$. Consequently, and remembering the co-acceleration of leptons and hadrons, the lepton injection will follow a simple power law with a hard index, leading to strong electron synchrotron flux in the optical and infrared ranges.

The parameter space region to explore is well defined by the above constraints. A scan was performed with the following ranges : $\delta_D \in [20-50]$, with seven linearly spaced bins; $R \in [10^{15}\text{ cm} - R_{max}]$, with ten logarithmically spaced bins; $\nu_{peak,p} \in [\nu_{max}/1000, \nu_{max}]$, with ten logarithmically spaced bins; $\eta \in [10, 50]$, with five linearly spaced bins; and $K_p \in [K^\star/3, 3K^\star]$, with five logarithmically spaced bins, where $K^\star$ corresponds to the proton density such that the peak of the proton synchrotron component is at the level of the *Fermi*-LAT data. In total, 17500 models were produced and the 1σ contour in the parameter space was obtained using the χ^2 distribution. The associated range for each parameters, and derived quantities, are available in Table 6.1. No solution were selected with $\delta_D < 35$. In the selected solutions, the emission region properties are thus $\delta_D = 35-50$ with $B = 0.8-32G$ and $R = 10^{15-17}$ cm. The associated jet power thus ranges from 8×10^{45} to 1.7×10^{48} erg.s^{-1} increasing with R. This corresponds to luminosity ranging from well below to above the Eddington luminosity of a $10^9 M_\odot$ black hole : $L_{Edd} \sim 1.26\times10^{47}$ erg.s^{-1}. A mass of $10^9 M_\odot$ was used here as a typical order of magnitude for an AGN SMBH. After this study, the mass of the black hole of TXS 0506+056 was estimated to be $3\times10^8 M_\odot$ [141], implying $L_{Edd} \sim 3.8\times10^{46}$ erg.s^{-1} and leaving our conclusion unchanged. The difference between the energy carried by protons and the magnetic field is represented by the ratio of their respective energy densities. For proton synchrotron scenarios it is $\frac{u_p}{u_b} = 1-89$, and is closer to equipartition for lower total jet power.

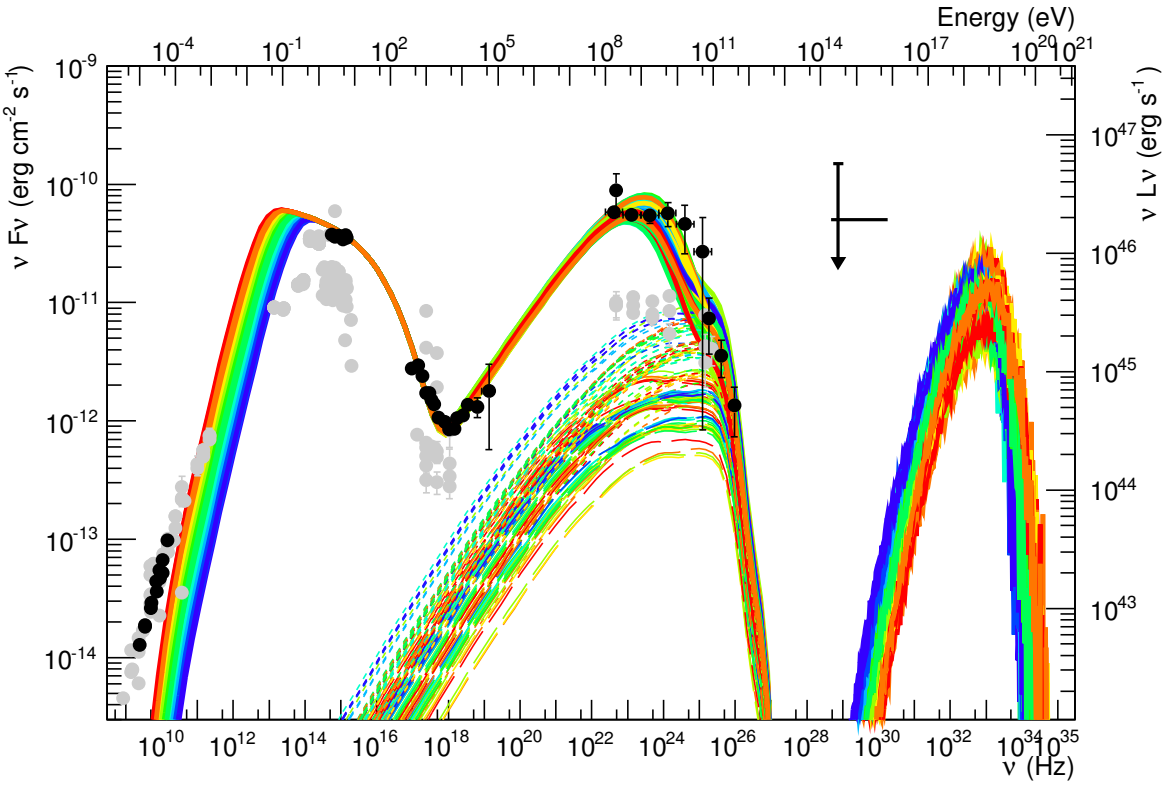

Figure 6.2: Modeling of TXS 0506+056 for the proton synchrotron scenarios. Black points are data from [36], while gray points are archival data. For each model, bold lines represent the total emission in photons (E<100 TeV) and neutrinos (single flavour, E>100 TeV); dashed lines the emission from pion cascades; dotted lines the emission from Bethe-Heitler cascades. Colours from red to blue represent increasing values of R. From [33].

The photon and neutrino SED for the selected solutions are displayed in Figure 6.2. The neutrino spectra are narrow, and typically peak above 10^{18} eV. Convoluting with the EHE muon neutrino sensitivity of IceCube, the predicted detection rate varies widely between 5.7×10^{-3} and 0.16 yr^{-1}. Since the neutrino spectrum peak at a way higher energy than the 90% uncertainty on the energy of IC-170922A (183 TeV-4.3 PeV), the detection rates drop strongly when limiting to this energy range to between 2.4×10^{-5} and 1.7×10^{-3} yr^{-1}. Since TXS 0506+056 was observed in a high state at HE during 6 months we can estimate the detection probability over this period if the neutrino flux remained constant. The maximum probability of detecting one neutrino with an energy compatible with that measured by IceCube during the 6-month high state of the source, assuming a Poisson law, is 0.085%. This probability drops when considering neutrino rates below the maximum. Additionally, the associated probability of detecting no events outside of this energy range over the same period is 82%. This time increasing for lower neutrino rates. The PS search, more sensitive at low energy, yields neutrino rates similarly low at $0.011 - 0.32$ yr^{-1}. The similarity is explained by the very hard neutrino spectra peaking at an energy where the EHE and PS sensitivity are relatively similar. The rates outside the IceCube neutrino energy range are identical to the EHE case and the probability of non-detection is between 85% and 99%. With these rates, accounting for IC-170922A using a proton-synchrotron solution is very unlikely but the detection of a single neutrino, if any, is the most likely scenario.

6.2.4 Mixed lepto-hadronic solutions

In the mixed lepto-hadronic solutions, the high energy emission is dominated by a combination of SSC and radiation from hadronic cascades. The associated region of the parameter space is very different from the proton synchrotron case with notably lower values of the magnetic field, lower maximum proton energies and higher proton densities. As a consequence, the neutrino flux is expected to be higher and peaks at lower energy.

While it is possible to interpret the broadband emission with a standard leptonic SSC model, our constraint of $\gamma_{e,min}$ of a few hundreds induces that the NuSTAR data cannot be produced by the SSC component in our models. It is instead accounted for by the cascades implying that these data can serve as upper limits to the hadronic component.

Some parameters are also fixed in order to reduce the parameter space to explore. In the region of the parameter space with mixed lepto-hadronic solutions the electrons are not fully cooled. It was thus decided to fix $\alpha_1 = 2.0$ and to limit our solutions to the case where no significant cooling is observed i.e. $\gamma_{e,max} \leq \gamma_{e,break}$. We also fixed $\eta = 10$ since solutions are found for this value of the proton acceleration efficiency. In the end, 3500 models were produced scanning the following parameter space : $\delta_D \in [20, 50]$, with seven linearly spaced bins; $R \in [10^{15}\text{ cm}, R_{max}]$, with ten logarithmically spaced bins; $\nu_{peak,p} \in [1.5\times10^{-8}\nu_{max}, 1.5\times10^{-5}\nu_{max}]$ with ten logarithmically spaced bins; $K_p \in [K^\star/3, 3K^\star]$, with five logarithmically spaced bins. The range for each parameters, and derived quantities, obtained for the solution selected with $\Delta\chi^2 < 1\sigma$ are available in Table 6.1. The region of the parameter space giving good solution is quite reduced with $B = 0.1 - 0.7$ G and $R = 2\times10^{15} - 1.5\times10^{16}$ cm for $\delta_D = 30 - 50$[2].

For all solutions, the SSC dominates the high energy peak while the flatter emission from cascades extend to both lower and higher energies and thus dominate the X-rays and VHE. The minimum jet power in this scenario is ~ 40 times higher than in the proton synchrotron case. It is achieved for intermediate values of δ_D, large B and small R. The large proton densities and lower magnetic field also imply an emission region far from the energy equipartition between protons and magnetic field with $\frac{u_p}{u_b} = 10^4 - 10^6$.

The photon and neutrino SED for the selected solutions are displayed in Figure 6.3. The neutrino flux is higher and peak at lower energies than in the proton synchrotron scenario. The combination of higher flux and peak energy closer to the optimal IceCube sensitivity leads to a significantly higher EHE neutrino detection rate between 0.1 and 3.0 per year. The lowest rate obtained here can be lowered to any value if one allows the SSC to dominate the X-rays leaving the hadronic processes mostly hidden in the photon observations.

The highest neutrino detection rates are achieved for solutions with the most kinetic energy carried by protons ($\propto u_p R^3$) which is associated in this case with an intermediate jet power. In general, the most extreme jet powers are not required to account for the detection of a neutrino by IceCube with detection rates above 0.5 yr^{-1} attainable even with a jet power close to the minimum value of 3.5×10^{47} erg.s^{-1}. The EHE detection rate restricted to the 0.183-4.3 PeV energy band is 0.008-0.11 yr^{-1}. It implies a probability for detecting one ν_μ with the energy measured by IceCube during the 6 months high-state of 5.2% in the case with the highest neutrino rate, and an associated probability for not detecting any events outside of the reconstructed energy interval of 5.5%. The neutrino rates obtained with the PS effective area are much higher : 0.3-6.9 yr^{-1} over the full energy range and 0.2-6.4 yr^{-1} when limiting to

[2] Allowing for a cooling break in the primary electron spectrum allows for solution with lower δ_D and a better representation of the optical data. However it would increase significantly the difficulty of the parameter scan while having limited effects on the the modelling of the high-energy spectrum and the resulting ranges of jet power and neutrino fluxes.

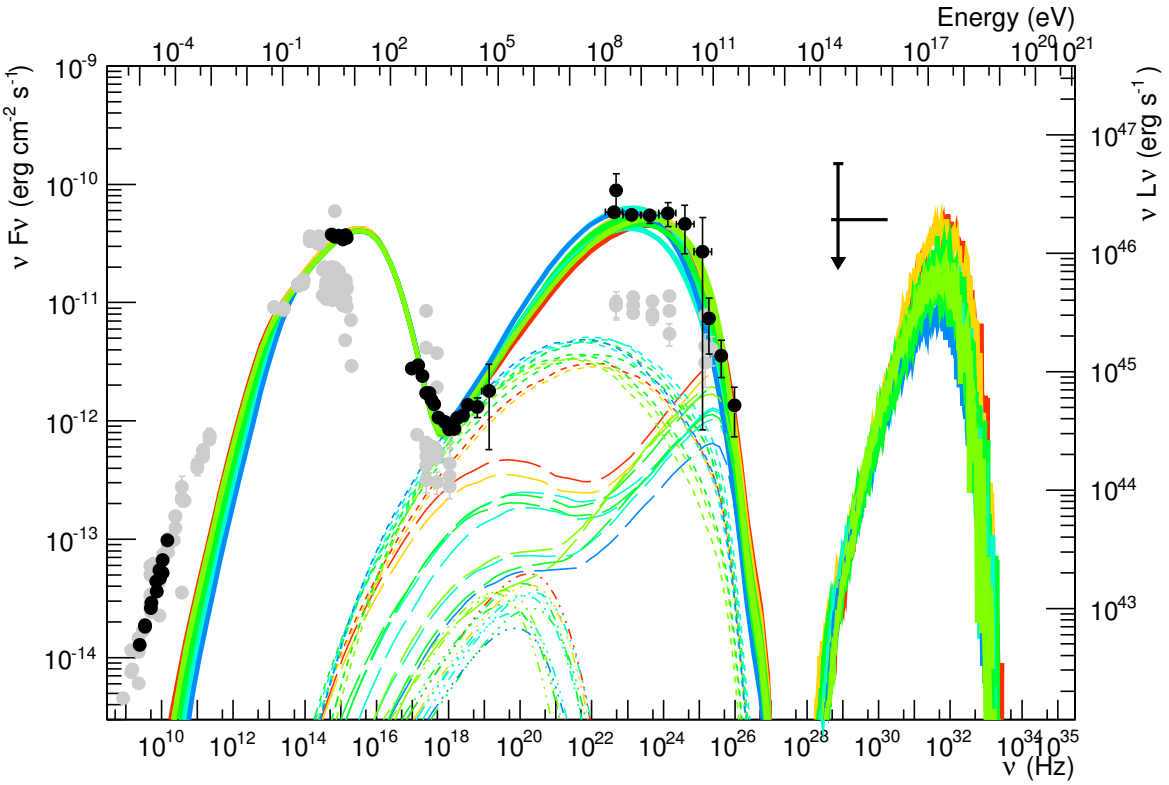

Figure 6.3: Modeling of TXS 0506+056 for the lepto-hadronic scenarios. Black points are data from [36], while gray points are archival data. For each model, bold lines represent the total emission in photons (E<100 TeV) and neutrinos (single flavour, E>100 TeV); dashed lines the emission from pion cascades; dotted lines the emission from Bethe-Heitler cascades; dotted-dashedlines the proton synchrotron emission. Colours from red to blue represent increasing values of R. From [33].

energies higher than 4.3 PeV. The highest rate corresponds to a Poisson probability of 4% to not detect any neutrino outside the IC-170922A energy range. The model with the highest neutrino production in the lepto-hadronic solution are thus in tension with the neutrino observations by IceCube. It should be noted that relaxing the assumption that $\gamma_{p,max}$ is linked to the acceleration timescale with $\eta = 10$ allows the neutrino spectra to peak at lower energies, thus lowering the expected rates.

6.3 Conclusion

A one zone lepto-hadronic model was used to recreate the SED of the 2017 high state of TXS 0506+056. Using physically motivated assumptions to reduce the parameter space, and general constraints from the electromagnetic data, we automatically explored the parameter space for two scenarios. Solutions are found in both the proton synchrotron and mixed lepto-hadronic scenarios and 1σ contours for the parameter space are extracted. Proton synchrotron solutions are characterised by a degeneracy between magnetic field and size of the emission region leaving a relatively larger parameter space as solution of the observed electromagnetic SED. In terms of energetics, proton synchrotron solutions allow for sub-Eddington luminosity

and near-equipartition of the energy between protons and magnetic fields. Alternatively, mixed scenarios require a high energy budget with a large dominance of protons. Mixed scenarios are also better constrained in terms of available parameter space. It should be noted that the energy budget could be reduced if we allowed a harder proton spectrum or a higher minimum particle energy. It can also be realised if a target photons field originates outside the jet by invoking external inverse Compton processes [142][143].

The two scenarios should in principle be distinguishable with future variability studies of this source using the variations of its photon SED. Indeed, both scenarios are characterised by different correlations between energy band. On one hand the lepto-hadronic scenario predicts a strong correlation between the low-energy and high-energy spectral bumps, as in a SSC scenario both are produced by the same population of electrons. On the other hand the proton-synchrotron scenario implies delays between the variations in the two components due to the different acceleration and cooling time scales of the electrons and protons. A delay is also expected between the hard X-ray component – coming from the cascades – and the high-energy peak – dominated by SSC – flux in the lepto-hadronic solutions. Observations of rapid flux variability over a few nights would require time-dependent modelling in order to obtain a more realistic, time dependent, neutrino detection rate. The stationary solutions presented here are however consistent with a variability time scale of one day thanks to the upper limits applied to R.

When looking at the neutrino output predicted by the model, one can see that proton synchrotron solutions are unlikely to explain an origin of the neutrino IC-170922A in the high state of TXS 0506+056. However detection of neutrinos with higher energy are occasionally expected from such a source. On the other hand, mixed lepto-hadronic solutions can account for this event without predicting more events in this energy range. The point source search at higher energy would however expect multiple neutrinos for a large portion of the available solutions. Neutrino observations of this source in a similarly high state of electromagnetic emissions in the future would be very useful to further constrain the model. If a second neutrino is detected this would favour the lepto-hadronic scenario, while the absence of any neutrino detections could be used to put constraints on the parameter space for both scenarios by limiting the acceptable maximum neutrino luminosity.

Table 6.1: Parameters used for the hadronic models. From [33].

	Proton-synchrotron	Lepto-hadronic
δ_D	$35-50$	$30-50$
R [10^{16} cm]	$0.1-9.7$	$0.2-1.5$
$^\star\tau_{\rm obs}$ [days]	$0.01-1.0$	$0.02-0.3$
B	$0.8-32$	$0.13-0.65$
$^\star u_B$ [erg.cm^{-3}]	$0.02-0.16$	$6.5\times10^{-4}-0.017$
$\gamma_{e,\rm min}$	500	500
$\gamma_{e,\rm break}$	$=\gamma_{e,\rm min}$	$=\gamma_{e,\rm max}$
$\gamma_{e,\rm max}$ [10^4]	$0.6-1.0$	$0.8-1.7$
$\alpha_{e,1}=\alpha_{p,1}$	2.0	2.0
$\alpha_{e,2}=\alpha_{p,2}$	3.0	3.0
K_e [cm^{-3}]	$6.3-9.1\times10^3$	$9.5\times10^3-2.6\times10^5$
$^\star u_e$ [10^{-5}erg.cm^{-3}]	$0.4-15.1$	$2.2\times10^3-43\times10^3$
$\gamma_{p,\rm min}$	1	1
$\gamma_{p,\rm break}$[10^9]	$=\gamma_{p,\rm max}$	$=\gamma_{p,\rm max}$
$\gamma_{p,\rm max}$[10^9]	$0.4-2.5$	$0.06-0.2$
η	$20-50$	10
K_p [cm^{-3}]	$10.4-2.0\times10^4$	$3.5\times10^3-6.6\times10^4$
$^\star u_p$ [erg.cm^{-3}]	$0.7-45$	$100-1400$
$^\star u_p/u_B$	$1.0-89$	$3.9\times10^4-79\times10^4$
$^\star L$ [10^{46} erg.s^{-1}]	$0.8-170$	$35-350$
$^\star\nu_{\rm EHE}$ [yr^{-1}]	$5.7\times10^{-3}-0.16$	$0.11-3.0$
$^\star\nu_{\rm EHE,(0.183-4.3)\,PeV}$ [yr^{-1}]	$2.4\times10^{-5}-1.7\times10^{-3}$	$0.008-0.11$
$^\star\nu_{\rm PS}$ [yr^{-1}]	$0.011-0.32$	$0.3-6.9$

The luminosity of the emitting region has been calculated as $L=2\pi R^2 c\Gamma^2_{\rm bulk}(u_B+u_e+u_p)$, where $\Gamma_{\rm bulk}=\delta_D/2$, and u_B, u_e, and u_p, the energy densities of the magnetic field, the electrons, and the protons, respectively. The quantities flagged with a star (*) are derived quantities, and not model parameters. The full set of parameters is available as online material of [33].

Conclusion

The work presented in this manuscript is centred on the study of the variability of blazars. Blazars are active galactic nuclei ejecting a relativistic jet of particles in the observer direction, which is responsible for the majority of the photons seen by the observer. The associated SED extends over nearly 20 orders of magnitude in energy from the radio to VHE bands. Despite numerous observations and large theoretical efforts, the wide variety of blazars observational properties and variability prevented a clear understanding of the physics at work in these sources. In order to improve our understanding of AGN, more simultaneous observations of the multi-wavelength and multi-messenger properties of blazars will be required along with more precise estimations of their evolution.

My work was performed in the H.E.S.S. experiment, observing at VHE. At this wavelength short variability was observed from blazars with time scales as short as minutes. In the experiment my work was threefold :

- The H.E.S.S. experiment uses an observation technique with a limited field of view. Additionally the limited flux reaching Earth at VHE means that long observations are needed to detect usable signal. It can consequently only observe a limited fraction of the sky each night. In order to optimise the time used for AGN observations, the AGN Target of Opportunity program triggers observations of blazars seen in a state of high activity (flare) by other instruments – or sometimes by H.E.S.S. itself – and can also communicate this intention to instruments covering other wavelengths. Since on average the VHE flux will be higher than average at these times, it can allow to detect sources otherwise difficult or impossible to detect with H.E.S.S. and improve the precision of the temporal information extractable from the data from bright sources. The multi-wavelength coverage will also be increased compared to independent observations. As part of the AGN ToO program I participated to multiple monitoring of the multi-wavelength activity of AGN.

- The exploitation of data acquired by H.E.S.S. requires a careful analysis especially when considering time sensitive datasets. I performed a large analysis work which can be divided in two categories. The first is the extragalactic Round Up, a global monthly analysis of the extragalactic observations by H.E.S.S. It aims at identifying global analysis bugs, highlighting interesting datasets to the collaboration and discovering unexpected variability from the observed sources or in the field of view. A large part of my analysis work was focused on observations of bright activity from two blazars : 3C 279 and PKS 2022-077, observed in the context of the ToO program. In the case of 3C 279, out of six observation periods, two led to significant detections with interesting behaviours. In January 2018, a burst of VHE photons was observed during one night with little counterpart at high energy. This indicates an emission process potentially uncorrelated between HE and VHE. In June 2018, a correlated multiple day long flaring activity was detected at least in optical, at

HE and at VHE. Both the time scales and multi-wavelength properties are different from the January 2018 case highlighting the complexity of blazars. This complexity was also seen during the period without detections by H.E.S.S. with varying correlations between optical and HE. Further exploitation of these datasets is ongoing. PKS 2022-077 is a particularly distant source for VHE observations as absorption by ambient photons from the EBL suppresses the flux during propagation. No detection of this source was achieved over three ToO observation campaigns. Two of these allowed to derive limits on the flux constraining the extrapolation of the HE spectra. In these cases, limits were derived on the parameter of three hypothesis able to explain the non detection by H.E.S.S. It was found that a modification of the EBL model normalisation would not be compatible with EBL measurement leaving the possibilities of an intrinsic limit of the energy emitted in the emission region, an absorption by the broad line region low energy radiation, or the need for another effect we did not consider.

- The optimisation of the tools available to study short time variability. I developed a method automatically adapting the binning of a light curve based on the instantaneous significance of the signal received. It allows for the computation of light curves over datasets varying strongly with a high precision binning in the high state when enough signal is available, while still integrating the low state over long periods. The very short binning with varying time also led to further developments. First a new computation method for the significance using a Bayesian development to avoid bias from the frequentist approach. Second is the adaptation of a common variability estimator, the normalised excess variance, for non constant binnings. The later was tested along with the doubling time scale estimator since a new task force aiming at characterising AGN flares seen with H.E.S.S. will use the adaptive binning method to compute light curves. When applied to a particularly intense flare of PKS 2155+304 from July 2006; both estimators hint at variability over timescales of a few seconds when applied to a light curve created with a threshold significance per points of 5 sigma. Such short variability can be explained when considering substructures in the jet potentially created by MHD instabilities. A second tool was implemented in the H.E.S.S. analysis software. It allows for the filtering of previously identified time intervals of bad quality. The goal here is to recover the good parts of observation runs temporarily affected by issues. It is particularly needed for variable sources.

Following a detection of a neutrino by IceCube, and its potential association with the blazar TXS 0506+056, I also participated to the study of the neutrino yield of a lepto-hadronic model of emission for blazar jets. The parameter space of the model was explored and solutions close to the observed SED of TXS 0506+056 selected. The associated neutrino production is unlikely to explain the observed neutrino event in a proton synchrotron scenario but can be accounted for in mixed solutions with a sub-dominant hadronic cascade contribution to the high energy component of the SED. In the case of mixed solutions, additional neutrinos are predicted and the detection or non detection of this neutrinos can be used to constrain the models. The neutrino-photon multi-messenger astronomy is a promising field to differentiate between leptonic and hadronic processes in blazar jets.

With the start of CTA in the near future, the number of detected blazars and the temporal precision of observations will increase greatly thanks to the improvement in sensitivity. The

tools presented here could thus be commonly required. Very high energy astronomy will likely see exciting developments and discoveries in the decades to come.

Appendix A

Background integration

We want to obtain $P(s|N_{ON}I)$ integrated over the possible values of the background. This requires to perform the following integral :

$$Int = \int_0^{+\infty} b^{N_{ON}+N_{OFF}-i} e^{-(1+\alpha)b} db \tag{A.1}$$

Which is of the form :

$$Int = \int_0^{+\infty} b^n e^{-c\times b} db \tag{A.2}$$

By performing an integral by part we obtain :

$$Int = \left[\frac{1}{-c} b^n e^{-c\times b}\right]_0^{+\infty} - \frac{n}{-c}\int_0^{+\infty} b^{n-1} e^{-c\times b} db \tag{A.3}$$

Where the initial integral is visible with an additional factor -n/(-c) and a power n-1 instead of n. Applying this process n times we finally have:

$$Int = \left[e^{-c\times b}\sum_{j=0}^{n} \frac{(-1)^j n!}{(n-j)!(-c)^{j+1}} x^{n-j}\right]_0^{+\infty} \tag{A.4}$$

When developing the equation above, each term evaluated at infinity will go to zero due to the $e^{-c\times b}$. When evaluating at 0, the same will happen due to the x^{n-j} except when $j = n$. Hence :

$$Int = -\frac{(-1)^n n!}{(-c)^{n+1}} = \frac{n!}{c^{n+1}} = \frac{(N_{ON}+N_{OFF}-i)!}{(1+\alpha)^{N_{ON}+N_{OFF}-i+1}} \tag{A.5}$$

Inserting into equation 3.7 :

$$\begin{aligned} P(s|N_{ON}I) &\propto e^{-s}\sum_{i=0}^{N_{ON}} \frac{N_{ON}!}{i!(N_{ON}-i)!} s^i \alpha^{N_{ON}-i} \frac{(N_{ON}+N_{OFF}-i)!}{(1+\alpha)^{N_{ON}+N_{OFF}-i+1}} \\ &\propto \sum_{i=0}^{N_{ON}} \alpha^{N_{ON}-i} \frac{(N_{ON}+N_{OFF}-i)!N_{ON}!}{(1+\alpha)^{N_{ON}+N_{OFF}-i+1}(N_{ON}-i)!} \frac{s^i}{i!} e^{-s} \\ &\propto \sum_{i=0}^{N_{ON}} c_i \frac{s^i}{i!} e^{-s} \end{aligned} \tag{A.6}$$

with :

$$\begin{aligned} c_i &= \alpha^{N_{ON}-i} \frac{(N_{ON}+N_{OFF}-i)!N_{ON}!}{(1+\alpha)^{N_{ON}+N_{OFF}-i+1}(N_{ON}-i)!} \\ &= \frac{\alpha^{N_{ON}} N_{ON}!}{(1+\alpha)^{N_{ON}+N_{OFF}+1}} \frac{(1+\alpha)^i}{\alpha^i} \frac{(N_{ON}+N_{OFF}-i)!}{(N_{ON}-i)!} \\ &= Constant|_i \times (1+\alpha^{-1})^i \frac{(N_{ON}+N_{OFF}-i)!}{(N_{ON}-i)!} \end{aligned} \tag{A.7}$$

Bibliography

[1] T. S. Hamilton, S. Casertano, and D. A. Turnshek, *The Luminosity Function of QSO Host Galaxies*, ApJ**576** (Sep, 2002) Sep 61–74, arXiv:astro-ph/0011255 [astro-ph].

[2] Event Horizon Telescope Collaboration, C. Goddi, G. Crew, V. Impellizzeri, *et al.*, *First M87 Event Horizon Telescope Results and the Role of ALMA*, The Messenger **177** (Sept., 2019) Sept. 25–35, arXiv:1910.10193 [astro-ph.HE].

[3] Event Horizon Telescope Collaboration, K. Akiyama, A. Alberdi, W. Alef, *et al.*, *First M87 Event Horizon Telescope Results. I. The Shadow of the Supermassive Black Hole*, ApJ**875** (Apr, 2019) Apr L1, arXiv:1906.11238 [astro-ph.GA].

[4] R. Antonucci, *Unified models for active galactic nuclei and quasars.*, ARA&A**31** (Jan, 1993) Jan 473–521.

[5] C. M. Urry and P. Padovani, *Unified Schemes for Radio-Loud Active Galactic Nuclei*, PASP**107** (Sep, 1995) Sep 803, arXiv:astro-ph/9506063 [astro-ph].

[6] M. C. Bentz and S. Katz, *The AGN Black Hole Mass Database*, Publications of the Astronomical Society of the Pacific **127** (Jan, 2015) Jan 67–73. http://dx.doi.org/10.1086/679601.

[7] J. E. Pringle, *Accretion discs in astrophysics*, ARA&A**19** (Jan, 1981) Jan 137–162.

[8] H. Cheng, W. Yuan, H.-Y. Liu, *et al.*, *Modelling accretion disc emission with generalized temperature profile and its effect on AGN spectral energy distribution*, Monthly Notices of the Royal Astronomical Society **487** (Jun, 2019) Jun 3884–3903. http://dx.doi.org/10.1093/mnras/stz1532.

[9] S. F. Hönig, *Redefining the Torus: A Unifying View of AGNs in the Infrared and Submillimeter*, The Astrophysical Journal **884** (Oct, 2019) Oct 171. http://dx.doi.org/10.3847/1538-4357/ab4591.

[10] E. S. Perlman, R. E. Mason, C. Packham, *et al.*, *The Mid-Infrared Emission of M87*, ApJ**663** (Jul, 2007) Jul 808–815, arXiv:0704.1156 [astro-ph].

[11] N. Bennert, B. Jungwiert, S. Komossa, M. Haas, and R. Chini, *Properties of the Narrow-line Region in Seyfert Galaxies*, vol. 373 of *Astronomical Society of the Pacific Conference Series*, p. 521. 2007.

[12] B. Peterson, *The Broad-Line Region in Active Galactic Nuclei*, pp. 77–100. Springer Berlin Heidelberg, Berlin, Heidelberg, 2006. https://doi.org/10.1007/3-540-34621-X_3.

[13] D. Heinzeller and W. J. Duschl, *On the Eddington limit in accretion discs*, MNRAS**374** (Jan., 2007) Jan. 1146–1154, arXiv:astro-ph/0610742 [astro-ph].

[14] V. Beckmann and C. R. Shrader, *Active Galactic Nuclei*. 2012.

[15] M. Schmidt, *3C 273 : A Star-Like Object with Large Red-Shift*, Nature**197** (Mar, 1963) Mar 1040.

[16] P. Padovani, D. M. Alexander, R. J. Assef, *et al.*, *Active galactic nuclei: what's in a name?*, A&A Rev.**25** (Aug, 2017) Aug 2, arXiv:1707.07134 [astro-ph.GA].

[17] M. S. Shaw, R. W. Romani, G. Cotter, *et al.*, *SPECTROSCOPY OF BROAD-LINE BLAZARS FROM 1LAC*, The Astrophysical Journal **748** (Mar, 2012) Mar 49. http://dx.doi.org/10.1088/0004-637X/748/1/49.

[18] J. Ballet, T. H. Burnett, S. W. Digel, and B. Lott, *Fermi Large Area Telescope Fourth Source Catalog Data Release 2*, arXiv e-prints (May, 2020) May arXiv:2005.11208, arXiv:2005.11208 [astro-ph.HE].

[19] The Fermi-LAT collaboration, *The Fourth Catalog of Active Galactic Nuclei Detected by the Fermi Large Area Telescope*, arXiv e-prints (May, 2019) May arXiv:1905.10771, arXiv:1905.10771 [astro-ph.HE].

[20] E. Nieppola, M. Tornikoski, and E. Valtaoja, *Spectral energy distributions of a large sample of BL Lacertae objects*, A&A**445** (Jan., 2006) Jan. 441–450, arXiv:astro-ph/0509045 [astro-ph].

[21] G. Ghisellini, *The blazar sequence 2.0*, arXiv:1609.08606 [astro-ph.HE].

[22] F. Aharonian, A. G. Akhperjanian, A. R. Bazer-Bachi, *et al.*, *An Exceptional Very High Energy Gamma-Ray Flare of PKS 2155-304*, ApJ**664** (Aug, 2007) Aug L71–L74, arXiv:0706.0797 [astro-ph].

[23] E. Aranzana, E. Körding, P. Uttley, S. Scaringi, and S. Bloemen, *Short time-scale optical variability properties of the largest AGN sample observed with Kepler/K2*, MNRAS**476** (May, 2018) May 2501–2515, arXiv:1802.08058 [astro-ph.HE].

[24] K. Nalewajko, *The brightest gamma-ray flares of blazars*, Monthly Notices of the Royal Astronomical Society **430** (Jan, 2013) Jan 1324–1333. http://dx.doi.org/10.1093/mnras/sts711.

[25] H. E. S. S. Collaboration, H. Abdalla, A. Abramowski, F. Aharonian, *et al.*, *Characterizing the γ-ray long-term variability of PKS 2155-304 with H.E.S.S. and Fermi-LAT*, A&A**598** (Feb, 2017) Feb A39, arXiv:1610.03311 [astro-ph.HE].

[26] P.-f. Zhang, D.-h. Yan, N.-h. Liao, and J.-c. Wang, *Revisiting Quasi-periodic Modulation in γ-Ray Blazar PKS 2155-304 with Fermi Pass 8 Data*, ApJ**835** (Feb., 2017) Feb. 260, arXiv:1611.04354 [astro-ph.HE].

[27] A. Neronov, D. Semikoz, and S. Sibiryakov, *Measuring parameters of active galactic nuclei central engines with very high energy γ-ray flares*, MNRAS**391** (Dec., 2008) Dec. 949–958, arXiv:0806.2545 [astro-ph].

[28] K. Wille, *SYNCHROTRON RADIATION*, Joint Universities Accelerator School JUAS (Jan., 2013) Jan. . https://indico.cern.ch/event/218284/contributions/1520454/attachments/352184/490697/JUAS2013_Synchrotron_Radiation_1.pdf.

[29] M. S. Longair, *High Energy Astrophysics*. 2011.

[30] O. Klein and T. Nishina, *Über die Streuung von Strahlung durch freie Elektronen nach der neuen relativistischen Quantendynamik von Dirac*, Zeitschrift fur Physik **52** (Nov., 1929) Nov. 853–868.

[31] S. R. Kelner and F. A. Aharonian, *Energy spectra of gamma rays, electrons, and neutrinos produced at interactions of relativistic protons with low energy radiation*, Phys. Rev. D**78** (Aug., 2008) Aug. 034013, arXiv:0803.0688 [astro-ph].

[32] A. Mücke, R. Engel, J. P. Rachen, R. J. Protheroe, and T. Stanev, *Monte Carlo simulations of photohadronic processes in astrophysics*, Computer Physics Communications **124** (Feb, 2000) Feb 290–314, arXiv:astro-ph/9903478 [astro-ph].

[33] M. Cerruti, A. Zech, C. Boisson, *et al.*, *Leptohadronic single-zone models for the electromagnetic and neutrino emission of TXS 0506+056*, MNRAS**483** (Feb., 2019) Feb. L12–L16, arXiv:1807.04335 [astro-ph.HE].

[34] G. B. Rybicki and A. P. Lightman, *Radiative processes in astrophysics*. 1979.

[35] A. Zech, M. Cerruti, and D. Mazin, *Expected signatures from hadronic emission processes in the TeV spectra of BL Lacertae objects*, A&A**602** (Jun, 2017) Jun A25, arXiv:1703.05937 [astro-ph.HE].

[36] IceCube Collaboration, M. G. Aartsen, M. Ackermann, J. Adams, *et al.*, *Multimessenger observations of a flaring blazar coincident with high-energy neutrino IceCube-170922A*, Science **361** (Jul, 2018) Jul eaat1378, arXiv:1807.08816 [astro-ph.HE].

[37] P. Giommi, T. Glauch, P. Padovani, *et al.*, *Dissecting the regions around IceCube high-energy neutrinos: growing evidence for the blazar connection*, arXiv:2001.09355 [astro-ph.HE].

[38] J. G. Kirk, F. M. Rieger, and A. Mastichiadis, *Particle acceleration and synchrotron emission in blazar jets*, A&A**333** (May, 1998) May 452–458, arXiv:astro-ph/9801265 [astro-ph].

[39] H. Sol, G. Pelletier, and E. Asseo, *Two-flow model for extragalactic radio jets.*, MNRAS**237** (Mar, 1989) Mar 411–429.

[40] T. Vuillaume, G. Henri, and P. O. Petrucci, *A stratified jet model for AGN emission in the two-flow paradigm*, A&A**620** (Nov, 2018) Nov A41, arXiv:1810.01718 [astro-ph.HE].

[41] B. Arsioli and Y. L. Chang, *The γ-ray emitting region in low synchrotron peak blazars. Testing self-synchrotron Compton and external Compton scenarios*, A&A**616** (Aug., 2018) Aug. A63, arXiv:1804.09761 [astro-ph.HE].

[42] M. L. Lister, *Parsec-Scale Jet-Environment Interactions in AGN*, vol. 386 of *Astronomical Society of the Pacific Conference Series*, p. 240. 2008.

[43] M. Zacharias, M. Böttcher, F. Jankowsky, *et al.*, *Cloud Ablation by a Relativistic Jet and the Extended Flare in CTA 102 in 2016 and 2017*, ApJ**851** (Dec., 2017) Dec. 72, arXiv:1711.06117 [astro-ph.HE].

[44] IceCube Collaboration, *et al.*, *Multi-messenger Observations of a Binary Neutron Star Merger*, ApJ**848** (Oct., 2017) Oct. L12, arXiv:1710.05833 [astro-ph.HE].

[45] D. D'Urso, *Cosmic Ray Physics*, arXiv e-prints (Nov., 2014) Nov. arXiv:1411.4642, arXiv:1411.4642 [astro-ph.HE].

[46] B.-B. Wang, X.-J. Bi, K. Fang, S.-J. Lin, and P.-F. Yin, *Time-dependent solar modulation of cosmic rays from solar minimum to solar maximum*, Phys. Rev. D**100** (Sept., 2019) Sept. 063006, arXiv:1904.03747 [astro-ph.HE].

[47] R. Blandford, P. Simeon, and Y. Yuan, *Cosmic Ray Origins: An Introduction*, Nuclear Physics B Proceedings Supplements **256** (Nov., 2014) Nov. 9–22, arXiv:1409.2589 [astro-ph.HE].

[48] C. Evoli, *The Cosmic-Ray Energy Spectrum*, Zenodo (Oct., 2018) Oct. . https://doi.org/10.5281/zenodo.2360277.

[49] A. W. Strong, I. V. Moskalenko, and V. S. Ptuskin, *Cosmic-Ray Propagation and Interactions in the Galaxy*, Annual Review of Nuclear and Particle Science **57** (Nov., 2007) Nov. 285–327, arXiv:astro-ph/0701517 [astro-ph].

[50] O. Adriani, G. C. Barbarino, G. A. Bazilevskaya, *et al.*, *PAMELA Measurements of Cosmic-Ray Proton and Helium Spectra*, Science **332** (Apr., 2011) Apr. 69, arXiv:1103.4055 [astro-ph.HE].

[51] R. Alves Batista, J. Biteau, M. Bustamante, *et al.*, *Open questions in cosmic-ray research at ultrahigh energies*, Frontiers in Astronomy and Space Sciences **6** (June, 2019) June 23, arXiv:1903.06714 [astro-ph.HE].

[52] Pierre Auger Collaboration, A. Aab, P. Abreu, M. Aglietta, *et al.*, *Observation of a large-scale anisotropy in the arrival directions of cosmic rays above* 8×10^{18} *eV*, Science **357** (Sept., 2017) Sept. 1266–1270, arXiv:1709.07321 [astro-ph.HE].

[53] A. Loureiro, A. Cuceu, F. B. Abdalla, *et al.*, *Upper Bound of Neutrino Masses from Combined Cosmological Observations and Particle Physics Experiments*, Phys. Rev. Lett.**123** (Aug., 2019) Aug. 081301, arXiv:1811.02578 [astro-ph.CO].

[54] M. C. Gonzalez-Garcia, M. Maltoni, and T. Schwetz, *Updated fit to three neutrino mixing: status of leptonic CP violation*, Journal of High Energy Physics **2014** (Nov., 2014) Nov. 52, arXiv:1409.5439 [hep-ph].

[55] V. Gribov and B. Pontecorvo, *Neutrino astronomy and lepton charge*, Physics Letters B **28** (Jan., 1969) Jan. 493–496.

[56] S. Bilenky, *Neutrino oscillations: From a historical perspective to the present status*, Nuclear Physics B **908** (July, 2016) July 2–13, arXiv:1602.00170 [hep-ph].

[57] M. G. Aartsen, M. Ackermann, J. Adams, *et al.*, *The IceCube Neutrino Observatory: instrumentation and online systems*, Journal of Instrumentation **12** (Mar., 2017) Mar. P03012, arXiv:1612.05093 [astro-ph.IM].

[58] H. Niederhausen, *Recent IceCube Measurements Using High Energy Neutrinos*, arXiv e-prints (Sept., 2019) Sept. arXiv:1909.12182, arXiv:1909.12182 [astro-ph.HE].

[59] IceCube Collaboration, M. G. Aartsen, M. Ackermann, J. Adams, *et al.*, *Search for steady point-like sources in the astrophysical muon neutrino flux with 8 years of IceCube data*, arXiv e-prints (Nov., 2018) Nov. arXiv:1811.07979, arXiv:1811.07979 [hep-ph].

[60] M. Ajello, M. Arimoto, M. Axelsson, *et al.*, *A Decade of Gamma-Ray Bursts Observed by Fermi-LAT: The Second GRB Catalog*, ApJ**878** (June, 2019) June 52, arXiv:1906.11403 [astro-ph.HE].

[61] S. Cherry, J. Sorenson, and M. Phelps, *Physics in Nuclear Medicine*. 01, 2012.

[62] A. Franceschini and G. Rodighiero, *The extragalactic background light revisited and the cosmic photon-photon opacity*, A&A**603** (July, 2017) July A34, arXiv:1705.10256 [astro-ph.HE].

[63] P. Sommers, *Extensive air showers and measurement techniques*, Comptes Rendus Physique **5** (May, 2004) May 463–472.

[64] J. N. Capdevielee, P. Gabriel, H. J. Gils, *et al.*, *Extensive air shower simulations with the CORSIKA program*, .

[65] KASCADE Collaboration, D. Heck, *Hadronic Interaction Models and the Air Shower Simulation Program CORSIKA*, .

[66] A. Barnacka, L. Bogacz, M. Grudzińska, *et al.*, *Monte Carlo Simulations For The Cherenkov Telescope Array Observatory Using Pl-Grid E-Infrastructure*, Computer Science **13** (01, 2012) 01 113.

[67] E. Hecht, *Optics*. Pearson education. Addison-Wesley, 2002. https://books.google.fr/books?id=T3ofAQAAMAAJ.

[68] J. Jelley, *Čerenkov radiation, and its applications*. Pergamon Press, 1958. https://books.google.fr/books?id=uzZRAAAAMAAJ.

[69] E. Ciarrocchi and N. Belcari, *Cerenkov luminescence imaging: physics principles and potential applications in biomedical sciences*, EJNMMI Physics **4** (12, 2017) 12 .

[70] T. Ashton, M. Backes, A. Balzer, *et al.*, *A NECTAr-based upgrade for the Cherenkov cameras of the H.E.S.S. 12-meter telescopes*, Astroparticle Physics **118** (Mar., 2020) Mar. 102425, arXiv:2001.04510 [astro-ph.IM].

[71] A. M. Hillas, *Cerenkov Light Images of EAS Produced by Primary Gamma Rays and by Nuclei*, .

[72] M. de Naurois and L. Rolland, *A high performance likelihood reconstruction of γ-rays for imaging atmospheric Cherenkov telescopes*, Astroparticle Physics **32** (Dec., 2009) Dec. 231–252, arXiv:0907.2610 [astro-ph.IM].

[73] K. Levenberg, *A Method for the Solution of Certain Non-Linear Problems in Least Squares*, The Quarterly of Applied Mathematics (1944) 164–168.

[74] R. D. Parsons and J. A. Hinton, *A Monte Carlo template based analysis for air-Cherenkov arrays*, Astroparticle Physics **56** (Apr., 2014) Apr. 26–34, arXiv:1403.2993 [astro-ph.IM].

[75] T. P. Li and Y. Q. Ma, *Analysis methods for results in gamma-ray astronomy.*, ApJ**272** (Sept., 1983) Sept. 317–324.

[76] D. Berge, S. Funk, and J. Hinton, *Background modelling in very-high-energy γ-ray astronomy*, A&A**466** (May, 2007) May 1219–1229, arXiv:astro-ph/0610959 [astro-ph].

[77] G. P. Rowell, *A new template background estimate for source searching in TeV gamma -ray astronomy*, A&A**410** (Oct., 2003) Oct. 389–396, arXiv:astro-ph/0310025 [astro-ph].

[78] F. Piron, *Etude des Propriétés spectrales et de la Variabilité de l'Emission gamma supérieure à 250 GeV des Noyaux actifs de Galaxies de type Blazar observés dans le cadre de l'Expérience CAT*. PhD thesis, Université de Paris-Sud (Paris XI), May, 2000.

[79] T. Hassan, L. Arrabito, K. Bernlöhr, *et al.*, *Monte Carlo performance studies for the site selection of the Cherenkov Telescope Array*, Astroparticle Physics **93** (July, 2017) July 76–85, arXiv:1705.01790 [astro-ph.IM].

[80] A. Acharyya, I. Agudo, E. O. Angüner, *et al.*, *Monte Carlo studies for the optimisation of the Cherenkov Telescope Array layout*, Astroparticle Physics **111** (Sept., 2019) Sept. 35–53, arXiv:1904.01426 [astro-ph.IM].

[81] Cherenkov Telescope Array Consortium, B. S. Acharya, I. Agudo, *et al.*, *Science with the Cherenkov Telescope Array*. 2019.

[82] A. Levan, P. Crowther, R. de Grijs, *et al.*, *Gamma-Ray Burst Progenitors*, Space Sci. Rev.**202** (Dec., 2016) Dec. 33–78, arXiv:1611.03091 [astro-ph.HE].

[83] H. Abdalla, R. Adam, F. Aharonian, *et al.*, *A very-high-energy component deep in the γ-ray burst afterglow*, Nature**575** (Nov., 2019) Nov. 464–467, arXiv:1911.08961 [astro-ph.HE].

[84] H. E. S. S. Collaboration, M. de Naurois, *GRB190829A: Detection of VHE gamma-ray emission with H.E.S.S.*, Astronomer telegram (May, 2020) May .

[85] MAGIC Collaboration, V. A. Acciari, S. Ansoldi, L. A. Antonelli, *et al.*, *Teraelectronvolt emission from the γ-ray burst GRB 190114C*, Nature**575** (Nov., 2019) Nov. 455–458.

[86] J. P. Lenain, *FLaapLUC: A pipeline for the generation of prompt alerts on transient Fermi-LAT γ-ray sources*, Astronomy and Computing **22** (Jan., 2018) Jan. 9–15, arXiv:1709.04065 [astro-ph.IM].

[87] H. E. S. S. Collaboration, H. Abdalla, R. Adam, F. Aharonian, *et al.*, *Constraints on the emission region of 3C 279 during strong flares in 2014 and 2015 through VHE gamma-ray observations with H.E.S.S*, arXiv e-prints (Jun, 2019) Jun arXiv:1906.04996, arXiv:1906.04996 [astro-ph.HE].

[88] MAGIC Collaboration, J. Albert, E. Aliu, H. Anderhub, *et al.*, *Very-High-Energy gamma rays from a Distant Quasar: How Transparent Is the Universe?*, Science **320** (June, 2008) June 1752, arXiv:0807.2822 [astro-ph].

[89] J. Aleksić, L. A. Antonelli, P. Antoranz, *et al.*, *MAGIC Observations and multiwavelength properties of the quasar 3C 279 in 2007 and 2009*, A&A**530** (June, 2011) June A4, arXiv:1101.2522 [astro-ph.CO].

[90] G. Emery, M. Cerruti, A. Dmytriiev, *et al.*, *Observations of the FSRQ 3C 279 during the flaring state of 2017 and 2018 with H.E.S.S.*, in *36th International Cosmic Ray Conference (ICRC2019)*, vol. 36 of *International Cosmic Ray Conference*, p. 668. July, 2019. arXiv:1908.06784 [astro-ph.HE].

[91] M. de Naurois, *H.E.S.S. detection of a strong VHE activity from the blazar 3C 279*, The Astronomer's Telegram **11239** (Jan, 2018) Jan 1.

[92] M. De Naurois, *H.E.S.S. and ATOM detection of renewed activity of the FSRQ 3C 279*, The Astronomer's Telegram **11680** (June, 2018) June 1.

[93] J. D. Scargle, J. P. Norris, B. Jackson, and J. Chiang, *Studies in Astronomical Time Series Analysis. VI. Bayesian Block Representations*, ApJ**764** (Feb, 2013) Feb 167, arXiv:1207.5578 [astro-ph.IM].

[94] F. Brun, *Search for weak or transient sources in the inner Galactic plane regions with H.E.S.S. Application to the study of the W49B supernova remnant region.* Theses, Université Pierre et Marie Curie - Paris VI, Sept., 2011. https://tel.archives-ouvertes.fr/tel-00645861.

[95] M. Holler, J. Chevalier, J. P. Lenain, D. Sanchez, and M. de Naurois, *Run-Wise Simulations for Imaging Atmospheric Cherenkov Telescope Arrays*, in *35th International Cosmic Ray Conference (ICRC2017)*, vol. 301 of *International Cosmic Ray Conference*, p. 755. Jan., 2017. arXiv:1711.01118 [astro-ph.HE].

[96] Fermi-LAT Collaboration, F. Acero, M. Ackermann, M. Ajello, *et al.*, *Fermi Large Area Telescope Third Source Catalog*, ApJS**218** (Jun, 2015) Jun 23, arXiv:1501.02003 [astro-ph.HE].

[97] N. Gehrels, G. Chincarini, P. Giommi, *et al.*, *The Swift Gamma-Ray Burst Mission*, ApJ**611** (Aug, 2004) Aug 1005–1020, arXiv:astro-ph/0405233 [astro-ph].

[98] D. N. Burrows, J. E. Hill, J. A. Nousek, *et al.*, *The Swift X-Ray Telescope*, Space Sci. Rev.**120** (Oct, 2005) Oct 165–195, arXiv:astro-ph/0508071 [astro-ph].

[99] M. Hauser, C. Möllenhoff, G. Pühlhofer, *et al.*, *ATOM - an Automatic Telescope for Optical Monitoring*, Astronomische Nachrichten **325** (Oct., 2004) Oct. 659–659.

[100] V. S. Paliya, *Fermi-Large Area Telescope Observations of the Exceptional Gamma-Ray Flare from 3C 279 in 2015 June*, ApJ**808** (Aug., 2015) Aug. L48, arXiv:1507.03073 [astro-ph.HE].

[101] J. D. Finke, *External Compton Scattering in Blazar Jets and the Location of the Gamma-Ray Emitting Region*, ApJ**830** (Oct., 2016) Oct. 94, arXiv:1607.03907 [astro-ph.HE].

[102] M. S. Shaw, R. W. Romani, G. Cotter, *et al.*, *Spectroscopy of Broad-line Blazars from 1LAC*, ApJ**748** (Mar., 2012) Mar. 49, arXiv:1201.0999 [astro-ph.HE].

[103] A. Franceschini, G. Rodighiero, and M. Vaccari, *Extragalactic optical-infrared background radiation, its time evolution and the cosmic photon-photon opacity*, A&A**487** (Sept., 2008) Sept. 837–852, arXiv:0805.1841 [astro-ph].

[104] H.E.S.S. Collaboration, C. Romoli, M. Boettcher, M. Cerruti, *et al.*, *H.E.S.S. observation of 3C 279 during optical and gamma-ray flares in 2017 and 2018*, Talk at TeVPA2018 (Aug., 2018) Aug. .

[105] G. Piano, A. Bulgarelli, M. Tavani, *et al.*, *AGILE detection of a gamma-ray flare from the FSRQ PKS 2023-07*, The Astronomer's Telegram **8879** (Mar., 2016) Mar. .

[106] Fermi-LAT Collaboration, S. Ciprini, *Fermi-LAT detection of a GeV gamma-ray flare from the blazar PKS 2023-07*, The Astronomer's Telegram **8932** (Apr., 2016) Apr. .

[107] G. Emery, F. Jankowsky, J. P. Lenain, *et al.*, *Observations of blazar PKS 2023-07 in flaring state with HESS and Fermi-LAT in 2016-2017 and constraints on an intrinsic cut-off*, in *36th International Cosmic Ray Conference (ICRC2019)*, vol. 36 of *International Cosmic Ray Conference*, p. 669. July, 2019.

[108] S. Abdollahi, F. Acero, M. Ackermann, *et al.*, *Fermi Large Area Telescope Fourth Source Catalog*, ApJS**247** (Mar., 2020) Mar. 33, arXiv:1902.10045 [astro-ph.HE].

[109] P. M. W. Kalberla, W. B. Burton, D. Hartmann, *et al.*, *The Leiden/Argentine/Bonn (LAB) Survey of Galactic HI. Final data release of the combined LDS and IAR surveys with improved stray-radiation corrections*, A&A**440** (Sep, 2005) Sep 775–782, arXiv:astro-ph/0504140 [astro-ph].

[110] E. F. Schlafly and D. P. Finkbeiner, *Measuring Reddening with Sloan Digital Sky Survey Stellar Spectra and Recalibrating SFD*, ApJ**737** (Aug., 2011) Aug. 103, arXiv:1012.4804 [astro-ph.GA].

[111] K. C. Chambers, E. A. Magnier, N. Metcalfe, *et al.*, *The Pan-STARRS1 Surveys*, arXiv e-prints (Dec, 2016) Dec arXiv:1612.05560, arXiv:1612.05560 [astro-ph.IM].

[112] A. Domínguez, J. R. Primack, D. J. Rosario, *et al.*, *Extragalactic background light inferred from AEGIS galaxy-SED-type fractions*, MNRAS**410** (Feb, 2011) Feb 2556–2578, arXiv:1007.1459 [astro-ph.CO].

[113] W. A. Rolke, A. M. López, and J. Conrad, *Limits and confidence intervals in the presence of nuisance parameters*, Nuclear Instruments and Methods in Physics Research A **551** (Oct., 2005) Oct. 493–503, physics/0403059.

[114] S. S. Wilks, *The Large-Sample Distribution of the Likelihood Ratio for Testing Composite Hypotheses*, Ann. Math. Statist. **9** (03, 1938) 03 60–62. https://doi.org/10.1214/aoms/1177732360.

[115] G. Casella and R. Berger, *Statistical Inference*. Duxbury Resource Center, June, 2001.

[116] Fermi-LAT Collaboration, S. Abdollahi, M. Ackermann, M. Ajello, *et al.*, *A gamma-ray determination of the Universe's star formation history*, Science **362** (Nov., 2018) Nov. 1031–1034, arXiv:1812.01031 [astro-ph.HE].

[117] G. . Madejski and M. Sikora, *Gamma-Ray Observations of Active Galactic Nuclei*, ARA&A**54** (Sept., 2016) Sept. 725–760.

[118] M. Meyer, J. D. Scargle, and R. D. Blandford, *Characterizing the Gamma-Ray Variability of the Brightest Flat Spectrum Radio Quasars Observed with the Fermi LAT*, ApJ**877** (May, 2019) May 39, arXiv:1902.02291 [astro-ph.HE].

[119] Y. Liu, D. R. Jiang, and M. F. Gu, *The Jet Power, Radio Loudness, and Black Hole Mass in Radio-loud Active Galactic Nuclei*, ApJ**637** (Feb., 2006) Feb. 669–681, arXiv:astro-ph/0510241 [astro-ph].

[120] J. Chevalier, *Active Galactic Nuclei population study at TeV with the H.E.S.S. telescopes and variability studies of the blazar PKS 2155-304 with SSC modelling.* Theses, Université de Grenoble Alpes, June, 2017. https://tel.archives-ouvertes.fr/tel-01690232.

[121] F. Brun, Q. Piel, M. de Naurois, and S. Bernhard, *Analysis methods to search for transient events in ground-based very high energy γ-ray astronomy*, Astroparticle Physics **118** (Mar., 2020) Mar. 102429, arXiv:2001.06084 [astro-ph.IM].

[122] H. E. S. S. Collaboration, A. Wierzcholska, M. Zacharias, F. Jankowsky, and S. Wagner, *H.E.S.S. Monitoring of PKS 2155-304 in 2015 and 2016*, Galaxies **7** (Jan., 2019) Jan. 21, arXiv:1908.01232 [astro-ph.HE].

[123] R. Gambini and J. Pullin, *Nonstandard optics from quantum space-time*, Phys. Rev. D**59** (June, 1999) June 124021, arXiv:gr-qc/9809038 [gr-qc].

[124] K. Nandra, I. M. George, R. F. Mushotzky, T. J. Turner, and T. Yaqoob, *ASCA Observations of Seyfert 1 Galaxies. I. Data Analysis, Imaging, and Timing*, ApJ**476** (Feb., 1997) Feb. 70–82.

[125] T. J. Turner, I. M. George, K. Nandra, and D. Turcan, *On X-Ray Variability in Seyfert Galaxies*, ApJ**524** (Oct., 1999) Oct. 667–673, arXiv:astro-ph/9906050 [astro-ph].

[126] A. Lawrence and I. Papadakis, *X-Ray Variability of Active Galactic Nuclei: A Universal Power Spectrum with Luminosity-dependent Amplitude*, ApJ**414** (Sept., 1993) Sept. L85.

[127] F. Aharonian, A. G. Akhperjanian, G. Anton, *et al.*, *Simultaneous multiwavelength observations of the second exceptional γ-ray flare of PKS 2155-304 in July 2006*, A&A**502** (Aug., 2009) Aug. 749–770, arXiv:0906.2002 [astro-ph.CO].

[128] H. E. S. S. Collaboration and MAGIC Collaboration, M. Zacharias, J. Sitarek, D. Dominis Prester, *et al.*, *The exceptional VHE gamma-ray outburst of PKS 1510-089 in May 2016*, in *35th International Cosmic Ray Conference (ICRC2017)*, vol. 301 of *International Cosmic Ray Conference*, p. 655. Jan., 2017. arXiv:1708.00653 [astro-ph.HE].

[129] K. Chatterjee, M. Liska, A. Tchekhovskoy, and S. B. Markoff, *Accelerating AGN jets to parsec scales using general relativistic MHD simulations*, MNRAS**490** (Dec., 2019) Dec. 2200–2218, arXiv:1904.03243 [astro-ph.HE].

[130] D. Giannios, *Acceleration and emission of MHD driven, relativistic jets*, in *Journal of Physics Conference Series*, vol. 283 of *Journal of Physics Conference Series*, p. 012015. Feb., 2011.

[131] Y. N. Istomin, *Relativistic jets in active galactic nuclei: time variability*, MNRAS**408** (Oct., 2010) Oct. 1307–1312.

[132] G. Ghisellini, F. Tavecchio, G. Bodo, and A. Celotti, *TeV variability in blazars: how fast can it be?*, MNRAS**393** (Feb., 2009) Feb. L16–L20, arXiv:0810.5555 [astro-ph].

[133] K. Katarzyński, J. P. Lenain, A. Zech, C. Boisson, and H. Sol, *Modelling rapid TeV variability of PKS2155-304*, MNRAS**390** (Oct., 2008) Oct. 371–376, arXiv:0807.4533 [astro-ph].

[134] Y. H. Zhang, A. Celotti, A. Treves, *et al.*, *Rapid X-Ray Variability of the BL Lacertae Object PKS 2155-304*, ApJ**527** (Dec., 1999) Dec. 719–732, arXiv:astro-ph/9907325 [astro-ph].

[135] M. Cerruti, A. Zech, G. Emery, and D. Guarin, *Hadronic modeling of TeV AGN: Gammas and neutrinos*, arXiv:1610.00255 [astro-ph.HE].

[136] M. Cerruti, *High-energy emission from active galactic nuclei*. 2012. http://www.theses.fr/2012PA077225. Thèse de doctorat dirigée par Boisson, Catherine et Zech, Andreas Astronomie et Astrophysique Paris 7 2012.

[137] M. Cerruti, A. Zech, C. Boisson, and S. Inoue, *A hadronic origin for ultra-high-frequency-peaked BL Lac objects*, MNRAS**448** (Mar., 2015) Mar. 910–927, arXiv:1411.5968 [astro-ph.HE].

[138] A. Celotti and G. Ghisellini, *The power of blazar jets*, MNRAS**385** (Mar., 2008) Mar. 283–300, arXiv:0711.4112 [astro-ph].

[139] S. R. Kelner and F. A. Aharonian, *Energy spectra of gamma rays, electrons, and neutrinos produced at interactions of relativistic protons with low energy radiation*, Phys. Rev. D **78** (Aug, 2008) Aug 034013. https://link.aps.org/doi/10.1103/PhysRevD.78.034013.

[140] IceCube Collaboration, M. G. Aartsen, K. Abraham, M. Ackermann, *et al.*, *All-sky Search for Time-integrated Neutrino Emission from Astrophysical Sources with 7 yr of IceCube Data*, ApJ**835** (Feb., 2017) Feb. 151, arXiv:1609.04981 [astro-ph.HE].

[141] P. Padovani, F. Oikonomou, M. Petropoulou, P. Giommi, and E. Resconi, *TXS 0506+056, the first cosmic neutrino source, is not a BL Lac*, MNRAS**484** (Mar., 2019) Mar. L104–L108, arXiv:1901.06998 [astro-ph.HE].

[142] S. Ansoldi, L. A. Antonelli, C. Arcaro, *et al.*, *The Blazar TXS 0506+056 Associated with a High-energy Neutrino: Insights into Extragalactic Jets and Cosmic-Ray Acceleration*, ApJ**863** (Aug., 2018) Aug. L10, arXiv:1807.04300 [astro-ph.HE].

[143] A. Keivani, K. Murase, M. Petropoulou, *et al.*, *A Multimessenger Picture of the Flaring Blazar TXS 0506+056: Implications for High-energy Neutrino Emission and Cosmic-Ray Acceleration*, ApJ**864** (Sept., 2018) Sept. 84, arXiv:1807.04537 [astro-ph.HE].

Résumé:

Suite à chaque amélioration de notre connaissance de l'Univers, la résolution des zones d'ombre restantes dans nos théories nécessite l'utilisation de données de plus en plus détaillées, précises et variées. Les expériences ont donc amélioré leur sensibilité et résolution, mais aussi combiné leurs données pour former des compilations de données multi-longueurs d'onde et multi-messagers. Si une source est variable, les informations temporelles peuvent aussi ajouter des contraintes aux processus ayant lieu dans celle-ci. Les blazars sont des noyaux actifs de galaxies dont les émissions électromagnétiques, qui couvrent une large fraction du spectre électromagnétique observé, sont fortement variables et émises par un jet relativiste. L'expérience H.E.S.S. est un réseau de télescopes Cherenkov situé en Namibie réalisant des observation astronomiques de photons de très haute énergies. Ce manuscrit commence par une revue de la physique des blazars, de l'astronomie à très haute énergies et de l'expérience H.E.S.S., qui est suivie par les descriptions de divers travaux réalisés pour analyser et utiliser des données de variabilité de blazars. Des jeux de données obtenus durant des périodes d'activités intenses de deux blazars (3C 279 et PKS 2022-077) ont été analysés et mis en relation avec les données multi-longueurs d'onde contemporaines. Une nouvelle tâche de travail visant à caractériser de manière semi-systématique les épisodes d'activité de blazars est aussi introduite. Enfin, le manuscrit se termine par les résultats d'une exploration de l'espace des paramètres d'un modèle d'émission lepto-hadronique appliqué à une observation de TXS 0506+056 avec une détection coïncidente d'une activité électromagnétique et d'un neutrino.

Mots-clés: Noyaux actifs de galaxies; Astronomie; Très hautes énergies; Variabilité

Abstract:

Along with the improvement of our knowledge of the Universe, increasingly detailed, varied and precise data sets appeared necessary to solve the remaining unknowns. Experiments thus improved their sensitivities and resolutions but also combined their observations into large multi-messenger and multi-wavelength data sets. If a source is variable the available temporal information can also be used to constrain the possible processes taking place in this source. Blazars are active galactic nuclei displaying important variability with electromagnetic emissions covering a large fraction of the observed electromagnetic spectrum, emitted in a relativistic jet of particles. The H.E.S.S. experiment is an array of Cherenkov telescopes located in Namibia performing astronomical observations using very high energy photons. In this manuscript, reviews of blazar physics, very high energy astronomy and the H.E.S.S. experiment are followed by various worked performed to analyse and use variable data from blazars. Tools were developed in the H.E.S.S. analysis software aiming at improving the analysis of flaring events. Sets of data obtained during flaring events of two blazars (3C 279 and PKS 2022-077) were analysed and put into context with contemporaneous multi-wavelength observations. A new task aiming at characterising blazar flare in a semi-systematic way is also introduced. The manuscript then ends with the results of the exploration of the parameter space of a lepto-hadronic emission model applied to a flare of TXS 0506+056 coincident with the detection of an astrophysical neutrino with IceCube.

Key words: Active galactic nuclei; Very high energy astronomy; Variability